PHOTOPRODUCTION OF POSITIVE PIONS FROM HYDROGEN IN THE 600 TO 1000 MEV REGION

Thesis by

Franklin Painter Dixon

In Partial Fulfillment of the Requirements

For the Degree of

Doctor of Philosophy

California Institute of Technology

Pasadena, California

1960

DEDICATION

This work is dedicated to my wife,
Barbara, in recognition of her patience,
understanding, and encouragement.

ACKNOWLEDGEMENTS

The author wishes to express his appreciation to Dr. R. L. Walker for the supervision of this work. His interest and guidance have been invaluable.

The interest and encouragement of Dr. R. F. Bacher throughout the author's graduate residence is deeply appreciated. The assistance and suggestions of other members of the staff at the Synchrotron Laboratory are gratefully acknowledged.

The use of equipment designed or built by Dr. H. M. Brody, Dr. A. M. Wetherell, J. Boyden, Dr. P. L. Donoho, and Dr. J. I. Vette has proved most helpful.

The active assistance in accumulating data by J. Kilner, R. Diebold, and G. Neugebauer is deeply appreciated.

The author thanks Dr. V. Z. Peterson and Mr. E. B. Emery for maintenance of the liquid hydrogen target. The excellent support by the Synchrotron staff and crew in maintaining and operating the machine and equipment is sincerely appreciated.

The partial financial support of the United States Atomic Energy Commission is gratefully acknowledged.

ABSTRACT

A magnetic spectrometer and scintillation counter system was used to detect pions from the reaction $\gamma + P \longrightarrow \pi^+ + N$ initiated in a liquid hydrogen target by the bremsstrahlung beam of the Caltech Synchrotron. Observations were made at five mean laboratory photon energies, k = 600, 700, 800, 900, and 1000 Mev. At each energy measurements were made in the angular range 20° to 165° in the center-of-momentum system to provide differential cross sections at eleven angles.

The results are presented in the form of angular distributions in the c. m. system for each value of k. These differential cross sections have been integrated to provide total cross sections, whose variation with energy gives a peak at 700 Mev. Also, the 1000 Mev value is slightly above the 900 Mev total cross section and the 1000 Mev angular distribution indicates the strong influence of a higher angular momentum state thought to be J = 5/2.

The peak at 700 Mev and the behavior at 1000 Mev are interpreted to be effects of two resonances in the pion-nucleon system. The "second resonance" near 700 Mev is consistent with an isotopic spin and angular momentum I = 1/2 and J = 3/2, respectively, and the "third resonance" is presumed due to an I = 1/2 and J = 5/2 state. Arguments to support an assignment of $D_{3/2}$ for the second resonance and $D_{5/2}$ or $F_{5/2}$ for the third resonance at 1050 to 1100 Mev are offered.

TABLE OF CONTENTS

LIST OF ILLUSTRATIONS

LIST OF TABLES

I. INTRODUCTION

Since the prediction by Yukawa (1) of the existence of a particle with mass intermediate to the electron and proton, there has been much interest in the meson and its role in nuclear interactions. The confirmation of the existence of the charged π meson in the early emulsion experiments of Lattes, Occhialini, and Powell (2) was the forerunner of a great complex of experimental and theoretical investigations into the realm of meson physics. This study has developed in many directions. From the early cosmic ray experiments, which shed much light on the meson in its role as a fundamental particle, the use of accelerators to produce mesons and a study of the production processes and the interaction of the mesons with matter has led to a better understanding of its properties, but leaves much to be explained with the part it plays in the realm of nuclear forces.

The strong interaction between pions and nucleons has been studied extensively by means of pion nucleon scattering and pion photoproduction experiments. The lower energy pion-nucleon scattering data were analysed in terms of phase shifts associated with the angular momentum states and isotopic spin states of the pion-nucleon system. The treatment of the scattering and photoproduction in a phenomenological manner (3) was quite successful. No theory could produce the observed features until Chew developed the static theory, Chew and Low improved it, and Chew, Low, Goldberger, and Nambu used dispersion theory to provide a good correlation with experiments at low energies (4). The

analysis of a resonance at 195 Mev in the pion scattering experiments with positive pions (π^+, P) and negative pions (π^-, P) on hydrogen and the similar behavior in the π^0 and π^+ photoproduction experiments from protons for a laboratory photon energy near 300 Mev led to the assignment of isotopic spin, $I = 3/2$, and angular momentum $J = 3/2$ to the resonant state. This resonance, which we shall call the first resonance, was the prominent feature in the lower energy investigations (5).

The first measurements at higher energies were the scattering experiments of Cool, Piccioni, and Clark (6), which measured the total cross section for pion-nucleon interactions by attenuation of the pion beam from the Brookhaven Cosmotron. From this measurement there appeared to be an enhancement effect in the total cross section for π^-, P scattering starting at about 400 Mev laboratory pion energy and giving a broad peak centered at about 900 Mev. The π^+, P scattering did not show this feature, indicating that the $I = 3/2$ state did not participate in this enhancement. Further, the π^0 photoproduction data of Vette (7) indicated a broad hump in the region near 800 Mev laboratory photon energy and the situation was confused by the lack of correspondence between the energies in the center-of-momentum system for the peaks seen in the two experiments. The possibility of inelastic events in the scattering process made the correlation with single photoproduction questionable. It was apparent that additional information would be desirable and the logical extension of the lower energy π^+ photoproduction experiments seemed to offer a useful means of exploring the $I = 1/2$ state, since this state was twice as

strong in the π^+, N system as the π^0, P and would play a more dominant part in the π^+ photoproduction than in the π^0 case.

It was with these features in mind that the experiment described in this thesis was undertaken. The measurements were designed to give angular distributions from 20° to about 163° in the center-of-momentum system for laboratory photon energies of 600, 700, 800, 900, and 1000 Mev. The positive pion created by photon interaction with a hydrogen nucleus was selected for momentum by a magnetic spectrometer and identified by its energy loss in a system of scintillation and Čerenkov counters. For each of the five photon energies measurements were made at eleven different angles in the range indicated above.

The measurements, including the data described in the last paragraph, and the total cross sections obtained by integrating the differential cross sections of the angular distributions over all angles, have resulted in two important findings. The variation of the total cross section with photon energy indicated a second resonance near a laboratory photon energy of 700 Mev, which was also observed in measurements at Cornell (8). A third resonance at an energy near 1050 Mev is inferred from the drastic change in the angular distribution for 1000 Mev photons compared to those at lower energy and from the increase in total cross section from 900 to 1000 Mev. Thus, we see a total of three resonances in the photon reaction producing a single positive pion from a proton. The first resonance, which was observed in the lower energy experiments (9, 10), with an isotopic spin and angular momentum

$I = J = 3/2$ near a laboratory photon energy of 300 Mev. The second resonance in an $I = 1/2$ state with a possible angular momentum assignment $J = 3/2$ for photons near 700 Mev. And the third resonance near 1050 Mev in an $I = 1/2$ state with $J = 5/2$ inferred from the angular distribution.

The two higher energy resonances are believed to correspond to the two peaks observed in recent π^-, proton total cross section measurements (11). The correspondence between the c.m. energies in the scattering and photoproduction is not perfect, but the qualitative agreement between the two experiments supports the existence of three resonances and is consistent with the angular momentum assignments indicated above.

II. EXPERIMENTAL METHOD

A. General Method

Determination of the differential cross section for the photoproduction of single positive pions from hydrogen requires detection of the pions emitted into a given solid angle from the reaction:

$$\gamma + P \rightarrow \pi^+ + N \tag{1}$$

initiated by a photon of energy k. Since this is a two-body reaction the value of k is fixed when the angle and momentum of the π^+ are specified. These quantities are related by the equation:

$$k = \frac{M_p E_\pi - (1/2)(M^2_\pi - M^2_n + M^2_p)}{M_p - E_\pi + p_\pi \cos \theta_\pi} \tag{2}$$

where subscripts p, n, and π refer to the proton, neutron, and pion, respectively; and E is total energy, M is mass, p_π is pion momentum, and θ_π is pion angle, all in the laboratory system. Equation 2 is a result of requiring conservation of energy and momentum for the above reaction.

In this experiment the momentum was fixed by using a magnetic spectrometer to focus particles from a liquid hydrogen target onto an array of counters. The spectrometer accepts particles in a momentum range Δp with a mean value p_o and in an angular range $\Delta\theta$ centered at θ_o. From equation 2 it is evident that the range of acceptance, or window, of the spectrometer corresponds to a range of photon energies Δk with a mean value, which we usually refer to by the symbol k throughout this report. The kinematics of the single photoproduction reaction are given in figure 1, as are

Figure 1. Pion Momentum versus Laboratory Angle.

k is the laboratory photon energy. The dashed lines are the upper limit of π^+ momentum at a given laboratory angle for the pair production reaction. The rectangles represent the spectrometer acceptance window and θ_{cm} is the mean pion angle in the c.m. system for the single production reaction.

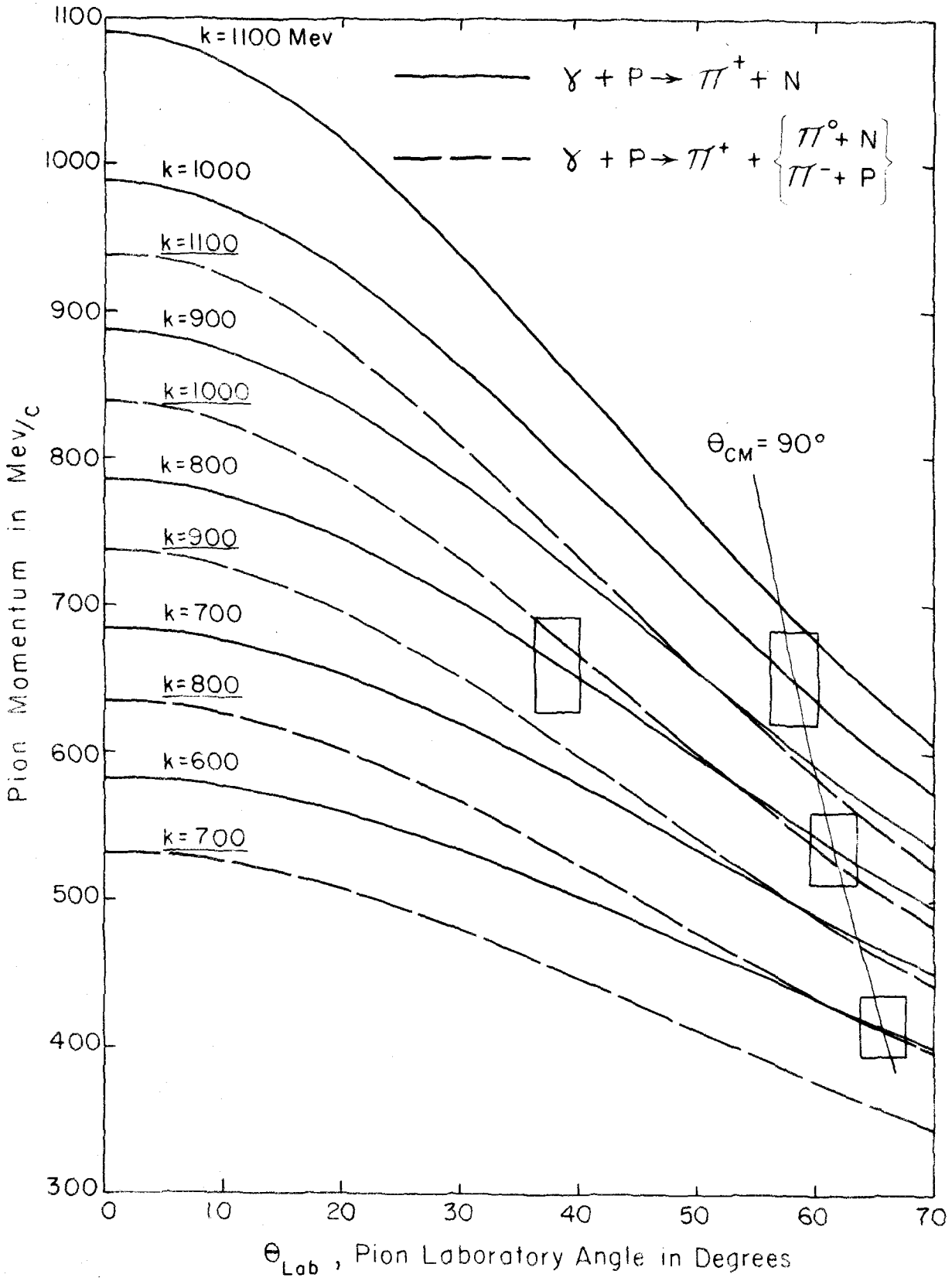
k = 1100 Mev
γ + P → π⁺ + N
γ + P → π⁺ + { π° + N / π⁻ + P }
k=1000
k=1100
k=900
k=1000
k=800
k=900
k=700
k=800
k=600
k=700
θCM = 90°
Pion Momentum in Mev/c
θLab , Pion Laboratory Angle in Degrees
1100
1000
900
800
700
600
500
400
300
0
10
20
30
40
50
60
70

the limiting curves for the pair production reaction:

$$\begin{aligned} \gamma + P &\longrightarrow \pi^+ + (\pi^0 + N) \\ &\longrightarrow \pi^+ + (\pi^- + P) \end{aligned} \qquad (3)$$

where the nucleon and other pion go off together and give the most energetic π^+ for a given photon energy and angle of emission. The spectrometer windows are shown for some of the experimental points by rectangles, which cover the ranges of momenta and angles accepted by the detection system when it is set to observe single π^+ particles from reaction 1 corresponding to a mean momentum and angle defined by the values at the center of the rectangle.

The presence of π^+ from the pair reaction would represent a contamination and the experiment was conducted in such a manner that this did not occur. The beam from the synchrotron contains photons of all energies up to the peak value, E_o. Referring to figure 1, it is evident that E_o should be as large as possible without providing photons with an energy capable of producing a π^+ from the pair reaction in the region covered by the spectrometer window. Thus, the dashed curve which would just pass through the lower left corner of the window rectangle gives the maximum E_o without pair contamination. In all but the k = 1000 Mev cases the value of E_o was dictated by the desire to use the full spectrometer acceptance window and provide the maximum counting rate without pair contamination. This was possible with a good margin of safety. For the 1000 Mev runs the synchrotron operated at E_o = 1080 Mev and π^+ mesons emitted in the sensitive region could come from the single reaction only.

B. Identification of Pions

While the magnet focussed particles in a particular momentum range and having a given sign of charge, it did not discriminate in any way against particles with different masses. In order to separate the pions from the other particles emitted from the target, it was necessary to incorporate a velocity selection based on pulse heights in a series of three scintillation counters at the rear of the magnet. For momenta less than 800 Mev/c this was sufficient to eliminate protons, but not electrons and muons. Since the muons, which arise from the decay of pions by the reaction

$$\pi^+ \longrightarrow \mu^+ + \nu \ , \qquad (4)$$

have a mass very near the pions, it is not possible to tell whether a count has been given by one or the other in the energy ranges studied here. For this reason it was necessary to calculate the contribution of muons to the observed counting rate and subtract it. This correction is discussed in the Appendix.

Electrons were not found to contribute to the counts obtained from the hydrogen in this experiment. This finding was based in part on the observation that the same counting rate within statistics for the full target and background runs was obtained when the magnetic field was reversed to accept negatively charged particles. Since no negative pions can be produced singly from hydrogen nuclei, the pion contribution to the observed hydrogen counting rate would be eliminated with a reversal of the field. However, the contribution of electrons would not be expected to change, if they are

a result of pair production in the target or elsewhere in the system.

In addition to the field reversal check, a monitor designed to show the presence of a significant number of electrons was provided by an "electron" counter based on the tendency of an electron to create a shower in a lead absorber placed before the last scintillation counter in the system, resulting in a large pulse from the counter. Similar effects initiated by pions and muons were much less likely, but not negligible, in the ranges of momenta observed. The "electron" count was never greater than the expected pion initiated events, presuming the observed counting rate to consist entirely of pions. The "electron" count for pions ran from (4.5 ± 1.0) % for p_o between 200 and 475 Mev/c to (14.0 ± 1.5)% at p_o = 950 Mev/c compared to the pion counting rate. This contribution from pions was established by observing the fraction of big pulses, or "electron" counts, relative to the total counting rate when the particles had to pass through 4 to 8 inches of lead in front of the entire array of counters operating in their normal manner with the lead absorber before the last one. The probability of an electron traversing this total amount of lead was negligible and the effects observed were associated with pion interactions in the shower absorber. As a consequence of these studies, no electron contamination has been detected and no correction for this effect was deemed necessary.

For the higher momentum points, where the energy losses in the counters for protons did not differ much from the pions, it was necessary to use a Čerenkov counter to discriminate against the protons. This was done for the forward angle runs, which required detection of pions with momenta greater than 600 Mev/c, the upper limit of the magnet when it was employed in the Medium

Energy position. This meant that the points measured with the High Energy position of the magnet had the additional discrimination of the Čerenkov counter to separate pions from higher mass particles within the momentum range of the spectrometer.

The efficiency of the Čerenkov counter for pions and protons was measured by selecting the particular particle desired at the momentum setting of the magnet by means of a time-of-flight requirement between a counter in the aperture of the magnet and the defining counter near the rear magnet focus. By introducing the proper delay in the front counter channel of the Berkeley coincidence circuit it was possible to choose the particles of interest, and determine what fraction of them gave counts in the Čerenkov when they were required to pass through it. This will be discussed further.

In general, the method of investigation consisted of choosing a laboratory photon energy, k, and a center of momentum angle, θ_{cm}, which was converted to a mean laboratory angle, θ_o, and momentum, p_o^s, corresponding to the chosen point. This purely kinematical value of momentum was adjusted to the mean magnet momentum, p_o, by allowing for the momentum lost in the hydrogen target, air path, and counter before entering the magnet and adjusted to insure that the mean photon energy defined by the spectrometer resolution and bremsstrahlung end point would have the desired value. The spectrometer was then set up for the desired values of p_o and θ_o and the counting rate was determined with hydrogen in the target. The hydrogen was then removed entirely or reduced to an atmosphere of hydrogen gas and the background

counting rate was measured. The difference in these rates was then adjusted for various factors to give the net pion counting rate from the hydrogen effective in the reaction and reduced to a value for the differential cross section at the particular value of k and θ_{cm} under study. Specific details of the corrections and calculations will be found in the section on Data Reduction.

The counting rates are a result of subtracting the "electron" counts, which were apparently due to pion interactions in the half inch Pb absorber between the last two counters, from the total number of counts for a given amount of target irradiation. This is necessary, since the "electron" events (pulses from C3 larger than 2.5 times minimum ionizing) are due to absorption effects, which are included in the absorption correction to be discussed in Section IV-B. In the absorption measurements the "electron" counts were likewise subtracted to obtain the counting rates.

III. EXPERIMENTAL EQUIPMENT

A. General Description

The experimental area of the California Institute of Technology Synchrotron Laboratory is shown in figure 2. The electrons, which are accelerated by the synchrotron, strike the radiator for a 20 millisecond interval once per second. The resulting bremsstrahlung process produces the photon beam, which passes out of the synchrotron through the primary collimator. The Pb scraper cleans the beam by allowing the primary beam defined by the collimator to pass without touching while intercepting particles and photons, which surround the primary beam as a consequence of the collimation process. After the first scraper the beam passes a hydrogen gas target, a second scraper, a series of sweeping magnets, and a third scraper before it strikes the liquid hydrogen target, which was used for this experiment. The beam continues until it enters the "beam catcher", which houses a thick-walled Cu-air ionization chamber, or beam monitor.

The magnetic spectrometer employed in this experiment is the Medium and High Momentum Magnet, which is shown in the high momentum position (referred to by H. E.) used for the forward angle points. The same magnet was modified to give a larger solid angle for lower momentum particles by moving it closer to the target, tilting the pole tips, and moving the counters closer to the magnet. The utility magnet, low momentum magnet, sweeping magnets, and third Pb scraper were removed from the experimental area to allow room for the most backward-angle measurements. Those points at 150° and greater in the center-of-momentum system were measured under these conditions. Details of the

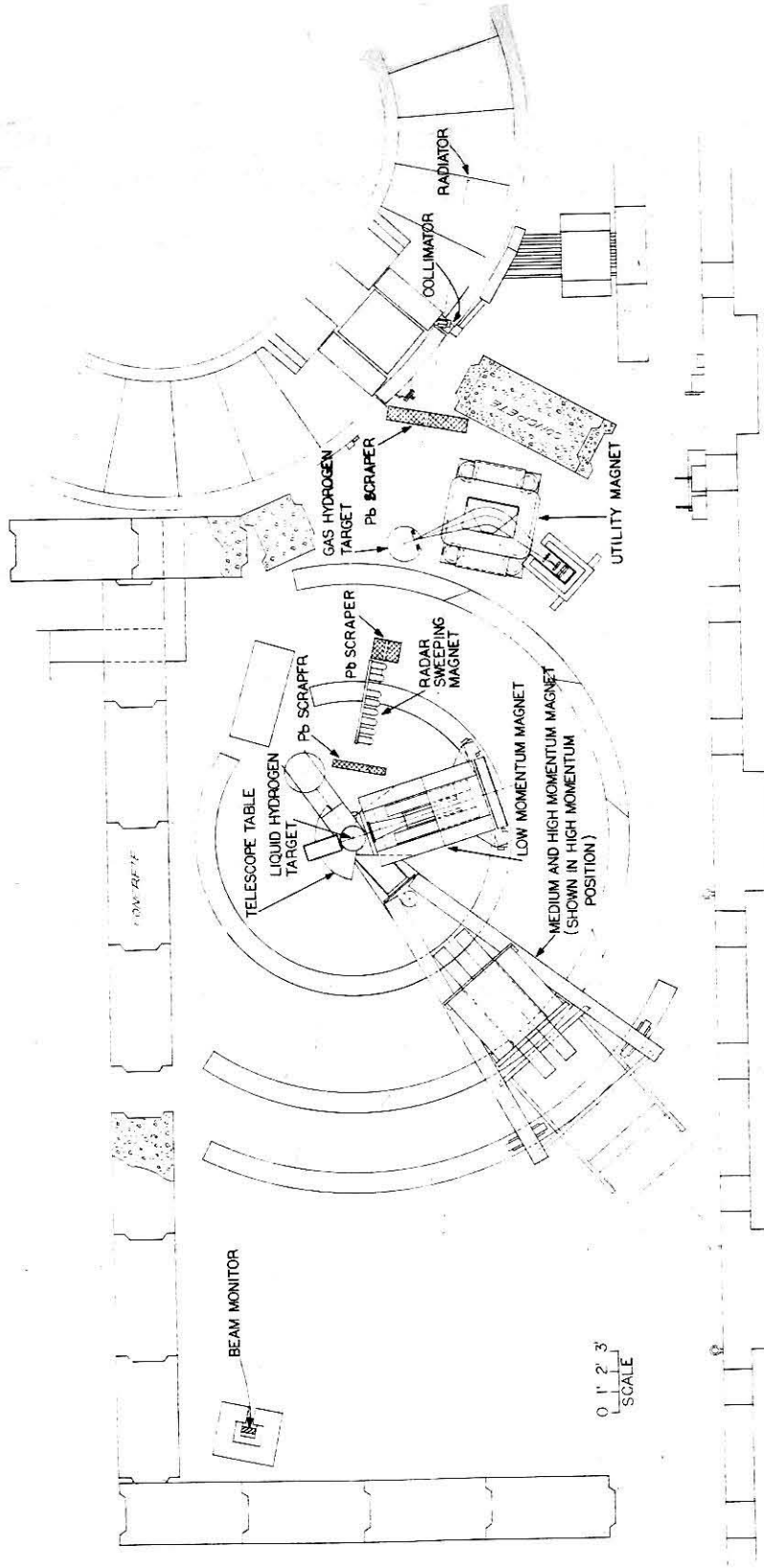

Figure 2. The Experimental Area

various experimental devices will be found in the following sections.

B. The Magnetic Spectrometer

Although the same magnet was used throughout these measurements, several geometrical arrangements of the aperture limiting devices and the defining counters resulted in changes in the properties of the system. Since the measurements were made in three separate runs with intervening separations of up to four months, there were also variations in some of the calibrations and quantities not directly associated with the spectrometer. Table 1 gives the spectrometer configurations and various properties which were correlated with them.

The spectrometer uses a uniform-field wedge-type single focussing magnet, which can analyse charged particles with momentum up to 1200 Mev/c in the H.E. position and up to 600 Mev/c in the M.E. position (12). It is mounted on a frame, which is supported on a pivot under the liquid hydrogen target at one end and two sets of wheels, which roll on iron tracks at a fixed radial distance from the pivot, at the other end. The focussing plane of the magnet is vertical to improve the angular resolution without loss in the solid angle of the spectrometer.

In the early stages of this experiment the solid angle of the spectrometer was defined by Pb slits. The vertical angle was limited by two tapered pieces of Pb with a separation of 12 inches at a distance of 56 inches from the center of the target. The horizontal limitation consisted of the last of four tapered Pb absorber

Table 1

Spectrometer Configurations and Associated Properties

Configuration: A = Medium Energy Spectrometer with Lead Slits and Standard $\Delta p/p$ Defining Counter.

B = Medium Energy Spectrometer with Lead Slits and Narrow $\Delta p/p$ Defining Counter.

C = Medium Energy Spectrometer with Aperture Counter (Paddle) and Magnet Pole-Face Veto Counters (Fans) Defining its Solid Angle with Standard $\Delta p/p$ Counter.

D = High Energy Spectrometer with Paddle-Fan Counters and Standard $\Delta p/p$ Counter.

$\Delta\Omega$: Spectrometer solid angle in steradian.

$\Delta p/p$: Spectrometer momentum dispersion constant.

t_o : Thickness of front counter placed before entrance aperture (inches).

ℓ_o : Distance from center of hydrogen target to front counter (inches).

L : Distance from center of hydrogen target to vertical aperture limitation.

S : Distance from center of hydrogen target to defining counter at rear of spectrometer.

A_π : Fraction of pions which pass through system without being absorbed.

ρ_H : Density of hydrogen which was effective in producing the observed net pion counting rate (gm/cc), i.e. full target minus background hydrogen density.

M : Ion chamber integrator constant in coulombs per BIP (Beam Integrator Pulse).

Table 1

Configuration	$\Delta\Omega$ (Steradian)	$\Delta p/p$	t_o (Inches)	ℓ_o (Inches)	L (Inches)	S (Inches)	A_π	ρ_H (gm per cc)	M (Coulomb/BIP)
M.E. Pb Slits (A)	.00785	.0965	.375	14.6	56.0	165.0	0.847	.0703	$.2209 \times 10^{-6}$
M.E. Pb Slits (B)	.00785	.0427	.375	14.6	56.0	165.0	0.847	.0703	$.2209 \times 10^{-6}$
M.E. Paddle Fans (C)	.00612	.1013	.250	61.0	61.0	165.0	0.851	.0688	$.2181 \times 10^{-6}$
H.E. Paddle Fans (D)	.00197	.0992	.250	107.5	107.5	260.5	0.800	.0688	$.2167 \times 10^{-6}$

strips attached to the pole faces of the magnet. The measurements made with this arrangement were in Configurations A and B. A schematic diagram of the spectrometer in this arrangement is given in figure 3a. The four strips of lead were not entirely effective in eliminating particles scattered or produced in the massive pole faces so they were replaced by the pole-face veto counters (Fans), which are shown in figure 3b. At the same time the vertical Pb slits were removed and the vertical aperture was defined by a counter operated in coincidence with the other counters at the rear focus. This aperture counter (Paddle) also replaced the front counter, C_o, which had too high a singles counting rate in the presence of intense beam dump with a resulting non-negligible accidental counting rate for the backward points. Measurements made with the M.E. position of the magnet and the Paddle-Fan aperture arrangement were made in Configuration C. It should be noted that the spectrometer solid angle and momentum resolution were different in Configurations A, B, and C, but the position of the magnet was the same for all three states with a target-to-rear-focus path length of 165 inches. The mean bending radius and mean deflection angle remained constant for all runs in the M.E. position.

For measurements of pions with momenta higher than the 600 Mev/c limit of the M.E. position it was necessary to reposition the magnet by moving it away from the target and tilting the poles to give a mean deflection angle of $27^{\circ}17'$ and a mean path length from target to rear focus of 260 inches. Also, the counters were moved back to a point near the rear focus. This H.E. position also utilized the Fan counter system of pole-face veto counters to eliminate

Figure 3a. Schematic Diagram of the Magnetic Spectrometer with the Medium Energy Magnet Position.

The magnet is shown with the lead slits used for aperture definition in Configurations A and B. The horizontal limiting slits are attached to the pole faces of the magnet. C_Q, C1, C2, and C3 are the scintillation counters through which detected particles passed. The photon beam passed through the hydrogen target at a mean height indicated by the horizontal center line. The mean particle path through the spectrometer is shown by the solid line continuation through the magnet and counter house.

Figure 3b. Schematic Diagram of the Magnetic Spectrometer with the High Energy Magnet Position.

The magnet is shown with the fan counters and the aperture counter used to define the magnet aperture in Configurations C and D. The Čerenkov counter in the counter house was used in Configuration D only, as was the high energy magnet position. In Configuration D the detected particles from the liquid hydrogen target had to pass through C_A, C1, C, C2, and C3 without producing a veto response in the fan counters on the magnet pole faces. The lead shielding in front of the C_A light pipe prevented Čerenkov pulses in the lucite. These were troublesome without the shielding.

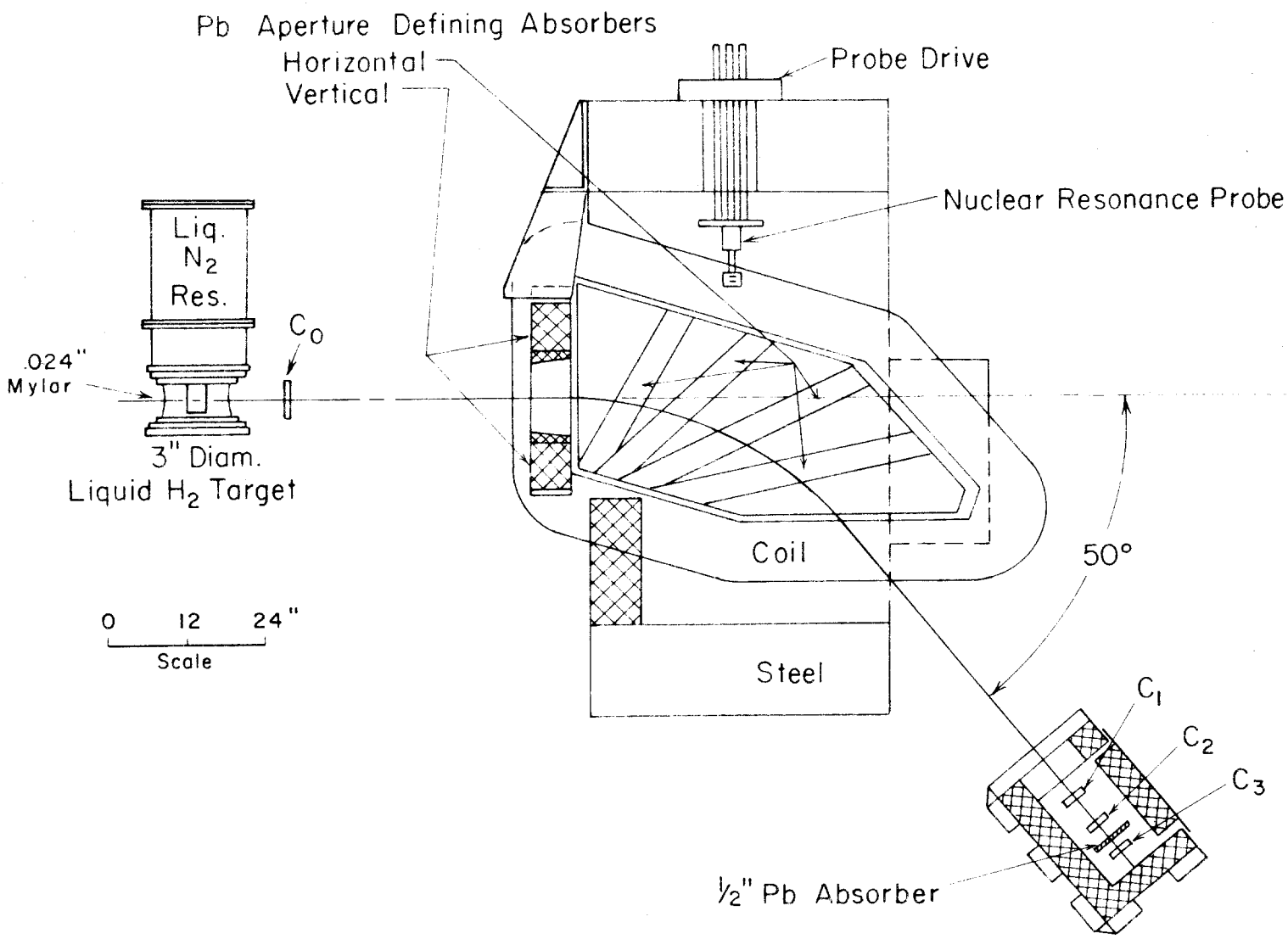
Pb Aperture Defining Absorbers
Horizontal
Vertical
Probe Drive
Nuclear Resonance Probe
Liq. N_2 Res.
C_0
.024" Mylar
3" Diam. Liquid H_2 Target
0 12 24"
Scale
Coil
50°
Steel
C_1
C_2
C_3
½" Pb Absorber

Figure 3a

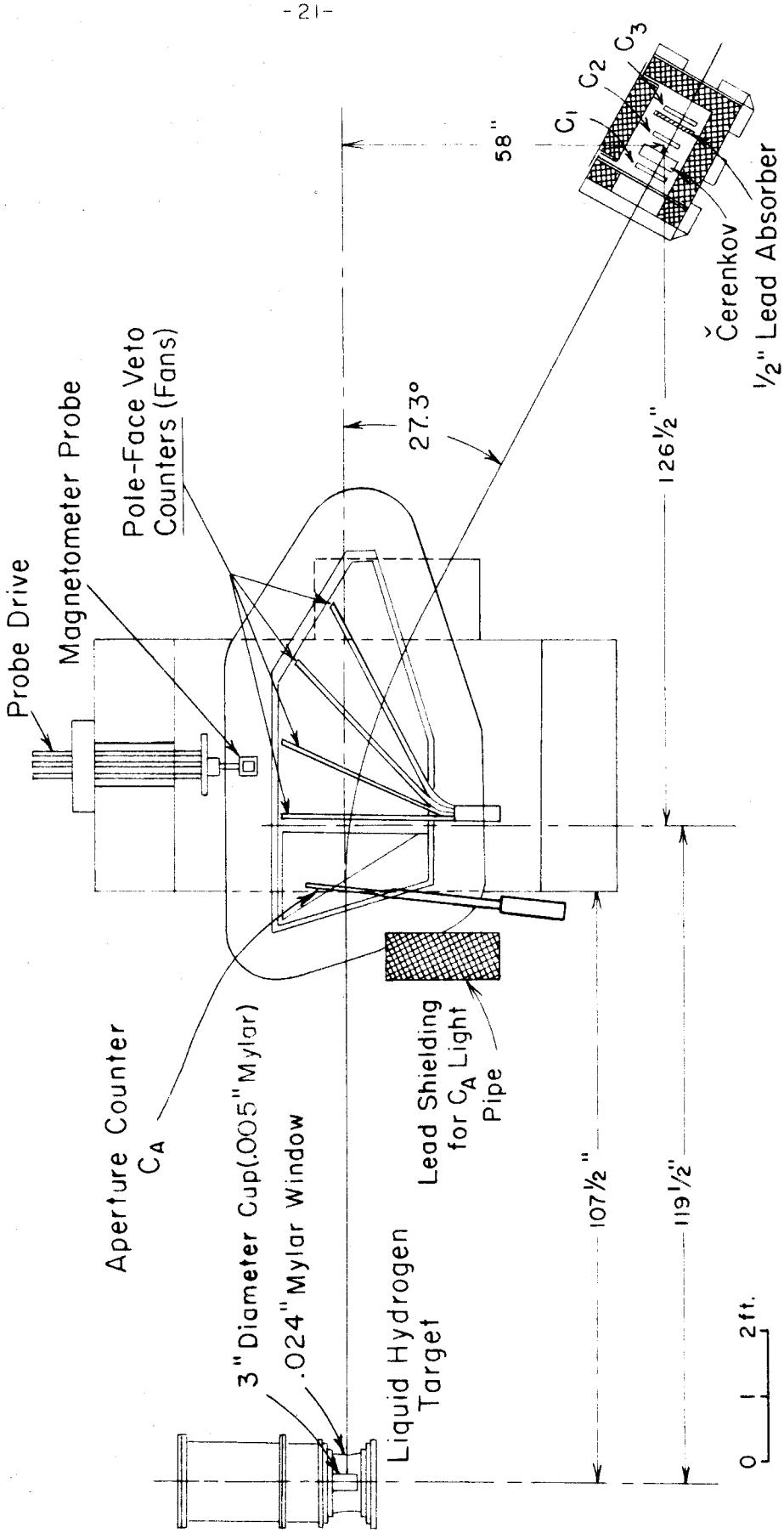
Probe Drive
Magnetometer Probe
Pole-Face Veto Counters (Fans)
27.3°
58"
C_1
C_2
C_3
Čerenkov
½" Lead Absorber
126½"
Aperture Counter C_A
3" Diameter Cup(.005" Mylar)
.024" Mylar Window
Liquid Hydrogen Target
Lead Shielding for C_A Light Pipe
107½"
119½"
0 1 2ft.

Figure 3b

spurious counts and the Paddle counter in the aperture to define the vertical solid angle and to eliminate cosmic ray background while providing a time-of-flight reference. The Čerenkov counter was added to the spectrometer system to separate pions and protons at momenta greater than 800 Mev/c, where the ionization energy loss in the scintillation counters was not sufficiently different to allow discrimination against proton contamination on a basis of pulse heights alone. This counter was made of 1.5 inches of Lucite and represents a major fraction of the absorption loss probability for pions passing through the spectrometer system. For this reason the Čerenkov counter was not present in Configurations A-C, but it was used only in Configuration D, where it served to eliminate the high momentum proton background.

The basic properties of the spectrometer are given in Table 1 under the configuration employed. The solid angle is defined by the aperture limitations previously described, but the momentum resolution is determined by the height of the defining counter. The sizes of the counters are given in a later section under "Counters."

The magnet current was supplied by a 50KW motor-generator and was controlled by a current regulator to better than $0.1^{o}/o$. The current was set and checked periodically by means of a proton resonance magnetometer described in the magnet report by Donoho (12).

The value of the desired magnetic field depended upon the mean momentum of the particles to be analysed. A careful calibration of the mean spectrometer momentum, p_o, was made

by the "floating wire" technique. A flexible and light weight wire was placed in equilibrium on the mean orbit through the magnet under the action of the magnetic field and direct current in the wire balanced by a known tension on the wire. The known quantities then permitted a determination of the corresponding momentum required for a charged particle with a trajectory along the path defined by the current carrying wire. The accuracy of these measurements was $\pm 0.4\%$ and represents the error in setting up the spectrometer momentum, since the frequency of the magnetometer could be determined to an accuracy of 1 part in 40,000 and was reproducibly set to an accuracy of 0.1%. The value of p_o for a given frequency was given by the relation:

$$p(\text{Mev/c}) = 2.940\ T(\text{gms})/I(\text{amps}), \qquad (5)$$

where T is the tension on the wire and I is the current flowing in the wire. The results of this calibration made it possible to adjust the spectrometer with a high degree of accuracy to fit the conditions set by the particular experimental requirements. The values of p_o versus f are given in the supplement to the magnet report (13).

The design of this 40-ton magnet permits a single person to change angles in a few minutes. The wheels on the rear of the magnet frame roll on an iron track and little effort is required to turn the whole spectrometer about the pivot located under the liquid hydrogen target. Marks were surveyed in every 10 degrees relative to the beam direction and a reference wheel attached to the magnet frame interpolated between these marks, enabling an

angular setting of the spectrometer to an accuracy of ± 0.05 degrees. The angular resolution (full width at half maximum) of the spectrometer in the laboratory was 2.06 degrees for Configurations A and B, 1.64 degrees for Configuration C, and 1.00 degrees for Configuration D. Of course, the resolution in the c.m. system was related to the laboratory system by the transformation:

$$\Delta\theta_{cm} = \frac{\partial\theta'}{\partial\theta} \Delta\theta \quad , \tag{6}$$

where the prime signifies the center-of-momentum system and $\Delta\theta$ is the angular resolution in the laboratory. The function $\frac{\partial\theta'}{\partial\theta}$ is determined by the kinematic variables of the reaction under observation, and in this experiment the resolution of pion angles in the center-of-momentum system was 0.5 to 1.7 times the values of $\Delta\theta$ for the spectrometer in the laboratory system.

C. Bremsstrahlung Beam

The beam from the Caltech synchrotron is a result of collision of the accelerated electrons with a .031 inch tantalum target, or radiator, at the end of the acceleration cycle. The spectrum of photon energies in the beam is a continuous function of energy and is represented very nearly by a thin target spectrum according to pair-spectrometer measurements to be discussed later. The total beam intensity is monitored by collecting the charge from a thickwalled copper-air ionization chamber, which is exposed to the beam, and integrating this charge in a precision electronic integrator (Model 3, Number 0196), which creates an output pulse when a definite quantity of charge has been collected on the capacitor at the input of the integrating circuit. The number of output pulses

are recorded on a mechanical counter and are referred to as the number of BIPS, or beam integrator pulses. The integrator was carefully calibrated by M. D. Daybell during this experiment and the integrator constant, M, given in table 1 represents the amount of charge required to give an output pulse from the integrator (coulombs per BIP).

The amount of charge created in the ion chamber depended on the peak energy of the photons in the beam. This peak energy, E_o, is the energy of the electrons which strike the radiator and is measured by the beam energy meter. The setting of E_o was important and a simple experiment was performed to check on the reading of the beam energy meter and at the same time check the shape of the photon spectrum and the mean momentum of the spectrometer. This was accomplished by comparing the calculated value of the spectrometer response in the form of pion counting rate relative to that for $E_o = 800$ Mev with the observed counting rate corrected for background and muon contamination obtained by varying E_o from 600 to 800 Mev with the spectrometer set at a mean momentum $p_o = 577$ Mev/c and a mean angle $\theta_o = 39.5^o$, corresponding to a mean photon energy for single pion production of $k = 695.4$ Mev. The calculated values obtained from the Datatron Resolution Program for the magnetic spectrometer by numerical integration over the target, spectrometer, and photon spectrum produced the solid curve shown in figure 4. The observations are indicated by the open circles with their associated errors. Within the experimental errors the measured and calculated values are in agreement. This shows that the setting of E_o,

Figure 4. Measured and Calculated Spectrometer Response as a Function of E_o Given by the Beam Energy Meter.

The solid line shows the response in the form of pion counting rate relative to $E_o = 800$ Mev calculated by a numerical integration over the spectrometer and target variables and the photon spectrum. The data are measured values obtained with the indicated E_o, and they are normalized to the $E_o = 800$ Mev counting rate. The counting rates were corrected for background and muon contamination. Errors in the photon spectrum, the indicated value of E_o, the mean momentum of the spectrometer, or the calculated resolution function would be expected to influence the agreement.

For these observations the spectrometer was set at $p_o = 577$ Mev/c and $\theta_o = 39.5^o$, corresponding to a mean photon energy $k = 695.4$ Mev.

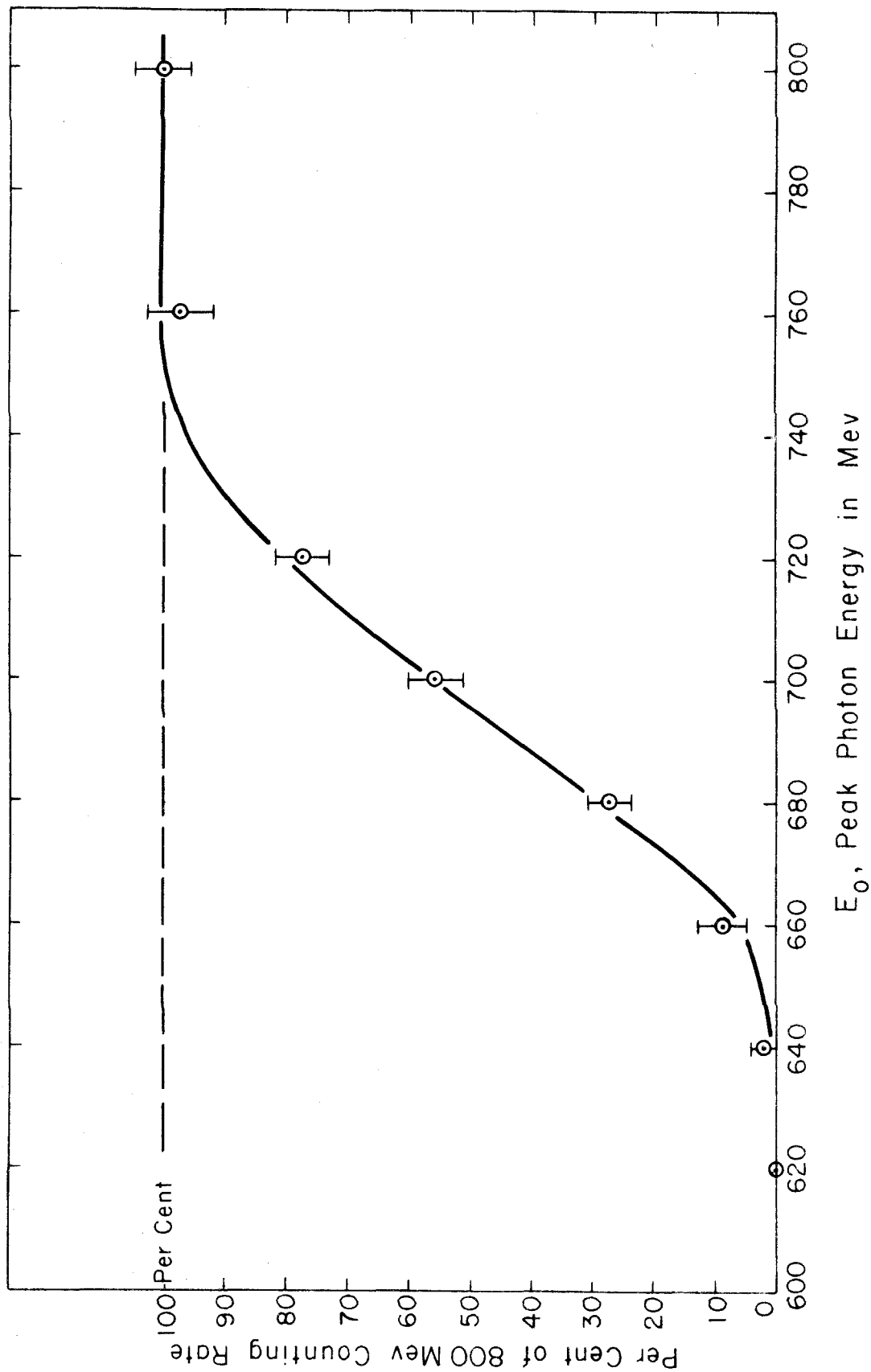
Per Cent of 800 Mev Counting Rate
100 Per Cent
90
80
70
60
50
40
30
20
10
0
600
620
640
660
680
700
720
740
760
780
800
E_0, Peak Photon Energy in Mev

using the beam energy meter, and the observed spectrometer sensitivity are consistent and gives a check on the mean spectrometer momentum and mean photon energy, as well.

For this experiment E_o was varied from 550 to 1080 Mev. In order to interpret the results, the total energy passing through the target must be determined. This is accomplished by converting the number of BIPS to a total energy based on the integrator calibration and a calibration of the beam monitor chamber by R. Gomez (14) using the Quantameter designed by R. R. Wilson (15). This total energy in the beam, W, is a function of E_o and the values of W for this experiment are shown in table 2. W is the energy required per BIP at 0^oC and 76.0 cm of Hg, i.e. a "standard" BIP.

The collimation of the beam from the synchrotron resulted in a rectangular beam 5.9 cm high by 4.4 cm wide at the liquid hydrogen target. The intensity of this beam was not constant but varied as a function of radial distance r from the center of the target in a plane perpendicular to the beam. The focussing properties of the spectrometer vary with position in the target and it is necessary to weight the various points used in averaging over the target according to the intensity of irradiation. This is achieved by expanding the beam intensity throughout the interaction volume in the 3 inch cylindrical mylar cup, which is shown schematically in figure 3, in terms of the moments about the center of the target. Table 3 gives the beam moments for various values of E_o. The moments are not important for most of the results reported here, since the effective path length along the

Table 2

Ion Chamber Calibration and Total Energy in the Bremsstrahlung Beam as a Function of Peak Energy.

E_o : Peak bremsstrahlung energy.

D : The weighting factor to convert standard response of calibration reference quantameter (14) to response of the monitor ion chamber.

U : The response of the beam monitor ion chamber to a beam with peak energy E_o, representing the energy in the beam per unit charge.

$W_{A,B}$, W_C, and W_D : The values of total energy in the beam required to give an output pulse from the beam integrator (one BIP) when measurements were made in the various configurations (see table 1). This is given by $W = UM$, where M is the integrator calibration constant from table 1.

Table 2

E_o Mev	D	U=4.93x10^{18}D Mev/Coulomb	$W_{A,B}$ 10^{12}Mev/BIP	W_C 10^{12}Mev/BIP	W_D 10^{12}Mev/BIP
550	0.888	4.377 x 10^{18}	0.967	0.955	0.949
750	0.966	4.762	1.052	1.039	1.032
900	1.020	5.029	1.111	1.096	1.090
1080	1.078	5.315	1.174	1.159	1.152
Interpolated values of W used in this experiment.					
600			0.989		
650			1.010		
700			1.031		1.0116
750			1.052		
800			1.072	1.059	1.052
850			1.0917		
920			1.118		
950			1.129		
990					1.122
1000			1.142	1.131	1.1254

Table 3

Beam Moments as a Function of E_o, Peak Bremsstrahlung Energy, for the 3 inch Liquid Hydrogen Target with a Beam 5.90 cm High by 4.40 cm Wide.

The moments are defined by

$\bar{\ell} = \int n(x, y)\, dxdy\, dz$ = effective path length

$x = \int x\, n(x, y)\, dxdy\, dz$

$xx = \int x^2\, n(x, y)\, dxdy\, dz$, etc.,

where $n(x, y)$ is the density distribution of the beam cross section determined from the densitometer analysis of Ilford G5 emulsion plates exposed behind 0.125 inch of lead at the center of the target. The limits of integration are set by the interaction volume of the beam in the target and the variables (x, y, z) are distances in centimeters from the center of the target, defined by a right hand coordinate system with z along the beam direction and x upward along the axis of the mylar cup which holds the hydrogen.

The function $n(x, y)$ is normalized by

$$\int n(x, y)\, dxdy = 1 .$$

Table 3

E_o (Mev)	716	810	931	1087	1080*
$\bar{\ell}$	7.230	7.240	7.247	7.223	7.2288
x	-1.473	-1.356	-1.254	-1.198	-1.199
xx	17.50	16.84	16.21	15.81	15.82
y	0.334	0.346	0.546	1.926	1.850
yy	9.722	9.529	9.396	9.813	9.776
zz	31.88	32.00	32.09	31.90	31.92
yzz	25.80	0.341	1.146	6.629	
yyzz	37.55	36.90	36.38	37.43	
zzzz	256.4	257.9	259.2	257.1	

*Interpolated moments.

beam through the target was the only moment used for all but the 1000 Mev data. For the k = 1000 Mev points the datatron computer was employed in a numerical integration over the target volume and spectrometer variables, requiring the following moments at E_o = 1080 Mev: $\bar{\ell}$, x, xx, y, yy, and zz. The other moments given in table 3 are useful to counter telescope experiments with this target and beam collimation. The moments were obtained from the Datatron Beam Moments Program written by R. Worlock and modified by F. Dixon.

With the spectrum measurement and total energy calibration of the beam monitor ion chamber it is possible to determine the number of photons in an incremental energy range from k to k + Δk. This is given by N(k)Δk and is

$$N(k)\Delta k = \frac{W\, B(k, E_o)}{E_o\, k}\, \Delta k \quad , \tag{7}$$

where $B(k, E_o)$ is the spectrum function which gives the variation from a pure 1/k dependence and is normalized by

$$\int_0^{E_o} B(k, E_o)\, dk = E_o \quad , \tag{8}$$

W is the total energy in the beam, and E_o is the end point energy. From the pair-spectrometer measurements (16) the value of $B(k, E_o)$ from $k = 0.65\, E_o$ to $k \doteq E_o$ was 0.9. Since the measurements in this experiment were made with photons in this range, the number of photons becomes

$$N(k)\Delta k = \frac{W\, 0.9}{E_o\, k}\, \Delta k \quad , \tag{9}$$

and this expression was used in the cross section calculations.

These pair-spectrometer measurements were made with a very narrow collimation of the photon beam, and the results indicated a spectrum very close to that expected from a thin target. The tantalum target in the synchrotron is a thick target, and these results do not reflect this character. The possibility exists that the narrow collimation selected the photons arising from bremsstrahlung processes in a small thickness of the target first encountered by the electrons, since the scattered electrons would generally be turned so photons from their interactions deeper in the target are too divergent to be accepted in the narrow beam. If these measurements do not reflect the true spectrum and the thick target spectrum is valid, the results reported for this experiment will be slightly higher, due to the lower value for $B(k, E_o)$ near the peak of the thick spectrum, compared to the thin spectrum. This feature is evident in figure 5, where the spectrum calculated by D. D. Elliott for the 0.2 radiation length tantalum target is indicated by the dashed line and the spectrum based on the measurements is given by the solid line. Future measurements are planned to check this possibility and give a more accurate determination of the spectrum.

D. The Liquid Hydrogen Target

The liquid hydrogen target was designed, built, and maintained by Dr. V. Z. Peterson and Mr. Earle Emery. Details of this target are given elsewhere (17), so only those features affecting this experiment will be described here. The target is shown schematically in figure 3, where the cylindrical cup which holds the hydrogen is indicated. This cup is made of mylar .005 inch

Figure 5. Bremsstrahlung Spectrum.

$B(k, E_o)$ is the function defined by equation 7 and normalized according to equation 8. The solid line resulted from analysis of the pair-spectrometer measurements (16) and the dashed line shows the "thick target" spectrum calculated by D. D. Elliott for the target (.031 inch of Tantalum) used to produce the beam.

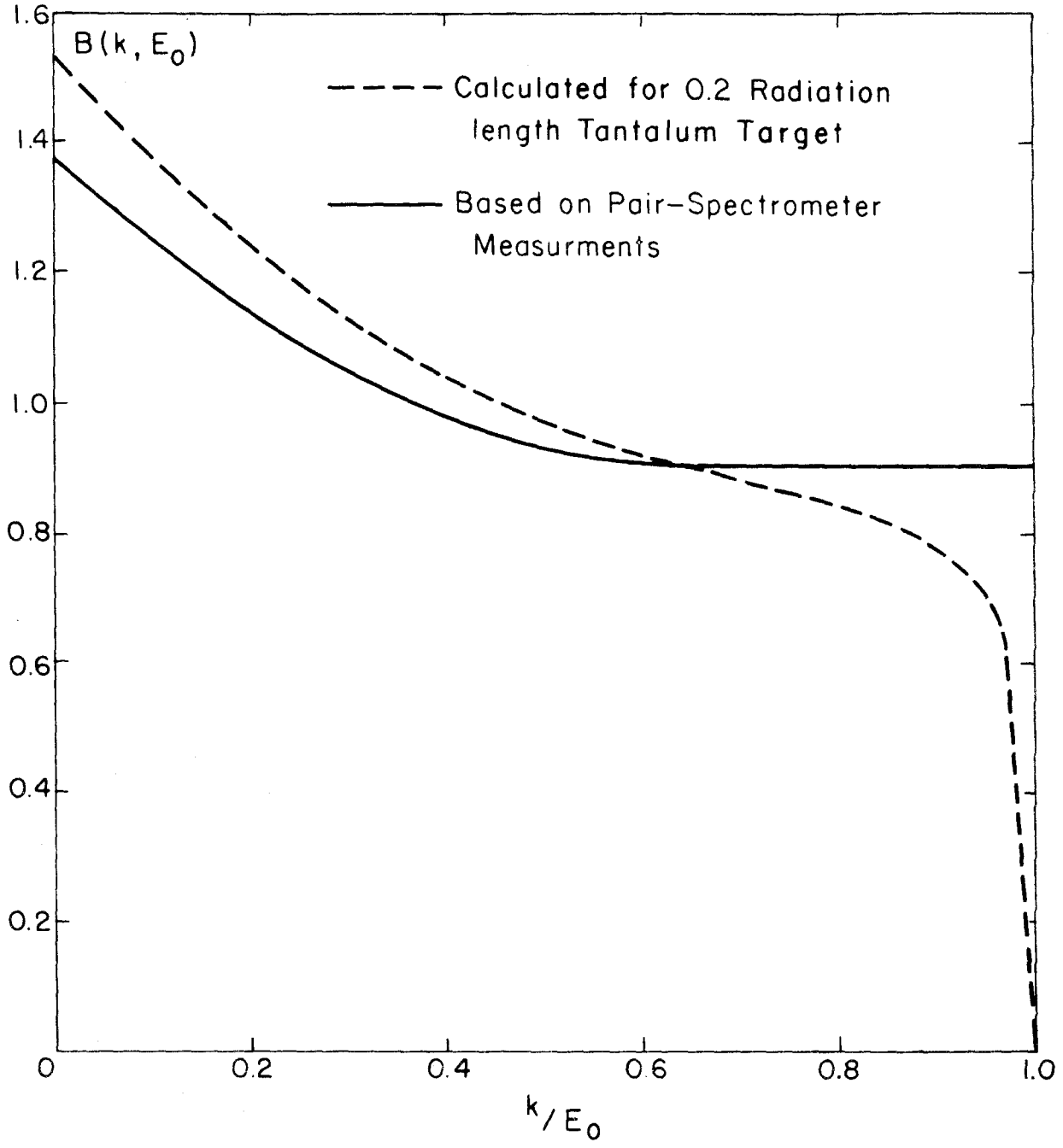
1.6
B(k, E0)
Calculated for 0.2 Radiation length Tantalum Target
Based on Pair-Spectrometer Measurments
1.4
1.2
1.0
0.8
0.6
0.4
0.2
0
0.2
0.4
0.6
0.8
1.0
k / E0

thick and measures 3 inches in diameter and 5.5 inches in length. The hydrogen was subjected to an average pressure of 84.6 cm of Hg by the atmosphere in the laboratory plus a 2psi check valve through which it was vented. This gave an equilibrium temperature of 20.63°A and a density of .0703gm/cc (18).

For the runs where the target was evacuated for background measurements this density of liquid hydrogen represented the effective density used in reducing the data to cross sections. This density is shown in table 1, where it is indicated that the backgrounds were obtained in this manner when configurations A and B were employed. In the other configurations the target was emptied of liquid hydrogen, but there was still an atmosphere of hydrogen gas in equilibrium with a reservoir of liquid hydrogen at the temperature and pressure indicated in the last paragraph. The density of this gas was calculated to be .0015gm/cc and was subtracted from the liquid hydrogen density to give a net effective density of .0688gm/cc contributing to the pion counting rates after the backgrounds were subtracted.

Particles originating in the target had to pass out through various radiation shields and mylar windows before they could be detected with the spectrometer. The material traversed included .029" of Mylar, .004" of Copper, .001" of aluminum, and about 1.5" of liquid hydrogen. The momentum loss in this material had to be included with losses due to the air path and counter in front of the magnet to obtain the value of p_o for the spectrometer, which was required to observe pions with a value of momentum p_o^s at the center of the hydrogen target. While these two values never differed by

more than 4 Mev/c, a small error in the magnet setting could shift the average photon energy by a significant amount when $\frac{\partial k}{\partial p}$ was much greater than 1. For example, the k = 900 Mev, θ_{cm} = 135° point was run before the magnet had been calibrated for p_o and the setting used was such that p_o^s was 4.9 Mev/c too high. This gave a mean photon energy of 923.6 instead of the 900 Mev desired. In the runs after calibration of the magnet for p_o it was possible to make the proper allowance before the measurements were made.

The liquid hydrogen was checked visually throughout the experiment to insure that foreign material was not in the irradiated region. The only evidence of foreign bodies in the hydrogen came when the target was evacuated and refilled for the early background runs. No solid material was observed during the actual measurements and the later technique for background measurements was adopted to reduce the likelihood of interruptions due to target contamination.

E. Counters

The scintillation counters employed in this investigation were made of polystyrene base plastic scintillator material obtained from the University of California Radiation Laboratory at Livermore. The sizes and locations of the various counters are given in table 4. Reference is made to figures 3a and 3b where the positioning and numbering of the counters is given. Counters C1 and C3 were used throughout the experiment, but the standard C2 was replaced by the narrow C2 for runs in

Table 4

Counter Sizes and Locations

The target center is located at the front focus of the magnet and the defining counter for the spectrometer system was C2, which was located at or near the rear focus.

C2(s) is the standard defining counter and C2(n) is the narrow defining counter used in Configurations A and B respectively.

H x W x T stands for height vertically x width horizontally x thickness, all in inches.

Table 4

Conf.	Counter	H x W x T	Distance from Target Center	Distance from Rear Focus
	C_o	5.00 x 3.25 x 0.375 in.	14.56 in.	
	C1	5.75 x11.0 x 0.787	159.9	-5.1 in.
A, B				
	C2(s)	4.75 x11.0 x 0.787	165.0	0
	C2(n)	2.00 x11.0 x 0.787	165.0	0
	C3	5.75 x11.0 x 0.394	170.0	+5.0
	C_A	12.34 x 3.24 x 0.250	61.0	
	C1	See above	161.0	-4.0
C				
	C2	See above	165.0	0
	C3	See above	169.0	+4.0
	C_A	See above	107.5	
	C1	See above	252.4	-7.6
D				
	$\check{C}$	6.0 x 11.0 x 1.50	256.4	-3.6
	C2	See above	260.5	+0.5
	C3	See above	264.6	+4.6

configuration B.

The counters used in front of the magnet were operated in coincidence with one of the counters at the rear and served to eliminate the cosmic ray background, which was a major source of contamination otherwise. In the early runs, Configurations A and B, C_o was used in the position shown in figure 3a and reduced the contribution to the background from the .024" mylar window which maintained the vacuum between the hydrogen cup and the outside air. This was a result of placing the counter close to the target so that only the particles from the cup and hydrogen in it could pass through the counter and the magnet aperture to register counts in the rear array of counters located in the counter house. When C_o was used the lead slits defined the vertical and horizontal aperture limits, as shown in figure 3a. For later runs the aperture, or paddle, counter designated by C_A was used instead of C_o. The requirement of a count from C_A still eliminated the cosmic ray background, but the empty target background was not limited by this system. The vertical aperture was defined by C_A, which was centered vertically on the mean path from the center of the target to the center of the defining counter, C2, at the rear. By virtue of its greater distance from the target C_A had a lower counting rate by a factor of eight than C_o, in spite of its larger area. This meant that random coincidences, or accidentals, were reduced to a negligible number even at the low counting rate points and at forward angles with a high counting rate in the front counter, where accidental counts were found to be troublesome with C_o.

The pole-face veto counters, which are shown in figure 3b and called fans since they have a fanlike appearance from the side, were used to define the horizontal aperture whenever C_A was the vertical limitation. These fan counters, designed by A. M. Wetherell and built by J. H. Boyden, following a suggestion by R. L. Walker, are described in detail on pages 36-44 in reference 19. In this experiment they served to eliminate scattering from the pole faces of the magnet and slit penetration problems in the energy ranges where the lead slits would not have been adequate, as well to to eliminate the possibility of having photoconversion in the massive iron pole faces produce spurious counts. The use of the fan counters is presumed to account for the lack of electrons even at forward angles, where magnets are notorious for the electron background apparently associated with the great expanse of iron required to obtain a suitable deflection.

The Čerenkov counter was a 1.5" thick piece of UVT Lucite designed and built by H. Brody and described in his thesis (19). As it was used in this experiment, it discriminated against protons of momenta up to 970 Mev/c and velocity less than 0.72 times the speed of light, i.e. $\beta \equiv v/c$ less than 0.72. The efficiency of the Čerenkov counter for pions and protons is indicated in figure 6. The curves show the inefficiency of the counter for pions in the momentum range of interest and the efficiency for protons in this momentum range. The efficiency was measured twice during the experiment and an average value with an error overlapping both measurements was used in the analysis, since the occurrence of the drift in the counter response could not be pinpointed. This is

Figure 6. Cerenkov Response to Pions and Protons.

The data are indicated by circles for proton efficiency and by squares for pion inefficiency. The closed and open data were obtained at the beginning and end, respectively, of the measurements with Configuration D.

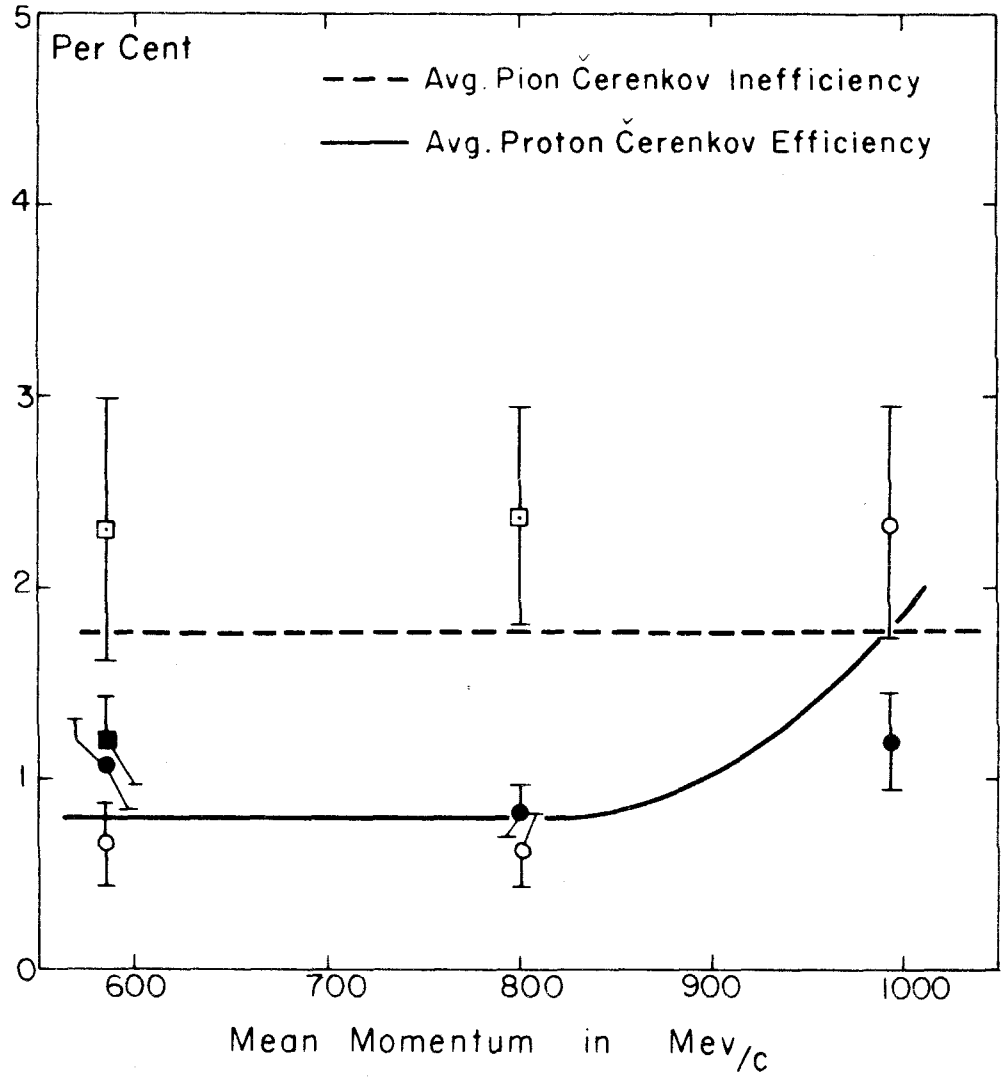
5
Per Cent
Avg. Pion Čerenkov Inefficiency
Avg. Proton Čerenkov Efficiency
4
3
2
1
0
600
700
800
900
1000
Mean Momentum in Mev/c

a small correction and the uncertainty introduced by this procedure is negligible.

The counters were glued at the ends to one or two lucite light pipes with Epon Resin, depending on the number of phototubes. The front counters, C_0 and C_A, had one tube and all the counters used in the rear had two, including the Čerenkov counter. The light pipes were in optical contact with the photocathodes through a layer of Celvacene vacuum grease. The phototubes were shielded from nearby magnetic fields by three successive layers of high susceptibility material. Next to the phototube was a cylinder of Mu Metal inside a second cylinder of Fernetic-Conetic material all encased in a soft iron tube. With this shielding the signals from the phototube were only reduced by about 20% in the presence of the highest field encountered in the experiment. Details of this shielding are discussed elsewhere (19).

F. Electronics

A block diagram of the electronics, which shows the most complex arrangement required for this investigation, is shown in figure 7. The dashed lines associated with the Čerenkov circuit indicate that those devices were not present in most of the measurements, as mentioned previously. The basic counter array consisted of C1, C2, and C3 with the counter in front. Signals went from the phototubes on either end of a counter in the array and were joined in parallel at the input to the preamplifier. To give the optimum resolution the tubes on a given counter were balanced to give the same average output pulse height when operated independently.

The preamp integrated the charge received at the input and gave a rectangular output proportional in height to the input charge and with a width determined by the length of shorted delay cable used to shape the pulse. For ease in identification C1, C2, and C3 had a width of 0.5, 0.60, and 0.75 microseconds, respectively, coming out of the preamp.

These signals from the preamp were amplified by the pulse amplifiers with a 0.07 microsecond rise time and fed into a 6-channel gated discriminator, which gave a standard 0.2 microsecond output when the input signal was bigger than the bias setting and the D.C. gating signal was present. The gate was about fifty milliseconds wide and centered on the beam dump which was about 20 milliseconds in duration. This prevented spurious counts during the injection period, etc., when stray transients in the laboratory were capable of causing false counts in the electronic system. The amplifier outputs also went to a mixer and delay circuit, where the various inputs were delayed by 0.5, 1.5, 2.5, and 3.5 microseconds, respectively, and mixed at the common output to allow observation of the output signals from the whole counter array on a single sweep of the Tektronix 513D oscilloscope.

Other inputs to the discriminator came from the various "fast" coincidence circuits. In runs in Configurations A and B there was one fast coincidence circuit of the Garwin type (20), which had a resolving time of 40 millimicroseconds for this experiment. The signals from C_0 and C_2 formed the inputs and gave an acceptable output if the two signals arrived within the resolving time of each other. The signal from C_0 was delayed by the time

Figure 7. Electronics Block Diagram.

The numbers on the phototube positions refer to RCA-6655 and -6810 phototubes. HP means Hewlett Packard. The fast scaler could be attached to any of the 6 input channels of the coincidence circuit. The dashed lines are associated with the Čerenkov counter circuits and were used in Configuration D only.

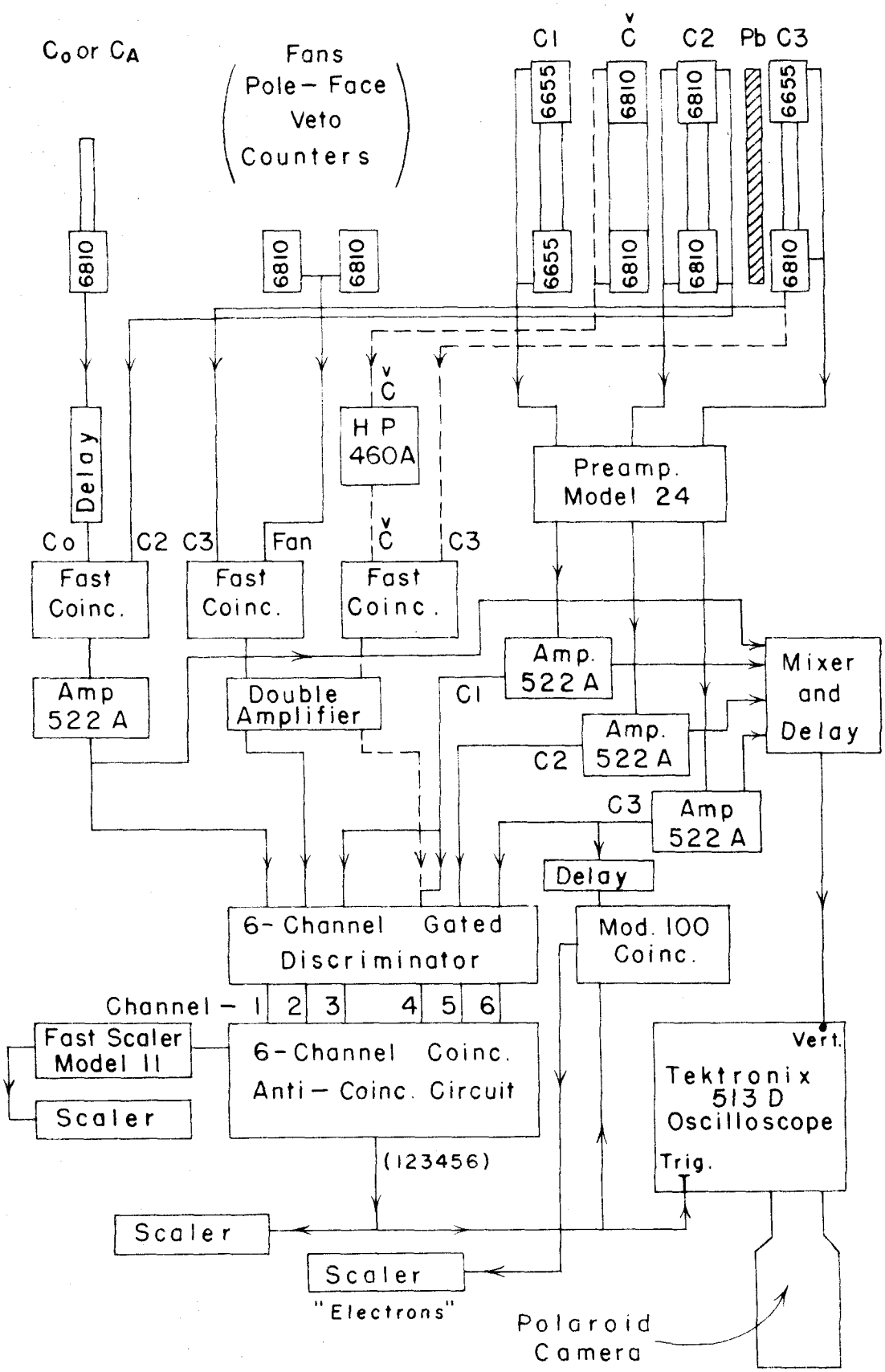

ELECTRONICS BLOCK DIAGRAM

it would take a pion with a velocity corresponding to the mean magnet momentum to pass from the front counter to the rear counter along the mean path through the magnet. It was not necessary to change the delay when the magnet current was shifted to a new value, since the resolving time was so large compared to the variation of transit times. With this arrangement the slowest pion took about 15×10^{-9} seconds while the fastest took 12.5×10^{-9} for the entire range of momenta observed in these configurations. The output signal from the Garwin was amplified in a pulse amplifier and delayed to arrive at the discriminator at the same time as the slow signals from the preamp given by a pion passing through the system.

In later runs the fans were also used in a fast circuit, as were the aperture counter and the Čerenkov counter. Here the fast coincidence circuit was a different type, which is called a Berkeley Circuit based on a design of Wentzel at the University of California Radiation Laboratory in Berkeley (21). Its performance was equivalent to the Garwin circuit with the additional possibility of reducing the resolving time to a few millimicroseconds by shortening a clipping stub on the plate of the E180F input tube. With this higher resolution in time it was then possible to use a time-of-flight selection of pions or protons to calibrate the Čerenkov counter, although this resolving time was lengthened to about 40 millimicroseconds during the actual recording of data for the experiment. This eliminated the necessity for an efficiency measurement for the time-of-flight circuitry, which had proved to be tedious in previous experiments.

The fan counters were operated in coincidence with the rear counter, C3, to reduce the counting rate in the slow coincidence circuit. The particles which were to be vetoed in this manner had to be particles which would otherwise register a count and thus had to pass through the array of counters. By requiring a fast coincidence with a particle fulfilling this requirement the possibility of accidental counts erasing valid counts was eliminated.

The Čerenkov signal had to be amplified before it would operate the fast coincidence circuit properly. This was done with a Hewlett Packard 460A amplifier. The other input to the Berkeley circuit was a signal from C3 properly delayed to coincide with the signal from the Čerenkov after its amplification. Here the coincidence requirement was needed to eliminate the effect of noise in the Čerenkov counter phototubes, which could give pulses nearly as big as the passage of a high velocity particle through the counter when the circuits were adjusted for operation with optimum efficiency for detection of fast particles.

The output signals from the fast circuits with the fan and Čerenkov inputs were amplified with a Double Amplifier designed by H. Brody, which is essentially two amplifiers made up of one feedback loop of the 522 amplifier indicated in the other circuits. These were used since the gain requirement of 100 was much less than the 2500 given by the 522. The ultimate performance was similar, except for the gain and a somewhat slower rise time than the .07 microsecond rise time of the 522.

After amplification and delay adjustments to compensate for the circuit variations, the fast coincidence outputs were introduced

into the 6-channel discriminator along with the signals from the preamp. The signals then went to the slow coincidence circuit where each input could be required in coincidence or veto by a switch setting. The resolving time of this circuit was 0.2 microsecond in coincidence and 0.4 microsecond in anticoincidence. The six inputs were varied to meet requirements of the various configurations. In Configurations A and B the channels were assigned as follows: 1-C1; 2-C1 veto (pulses bigger than pions); 3-Garwin; 4-C1; 5-C2; 6-C3. An output signal indicated that a particle with ionization bigger than or equal to a minimum ionizing particle had passed through C_0, C1, C2, and C3, but the signal in C1 was not big enough to be attributed to a proton. In Configuration C the Garwin signal was replaced by the Berkeley signal and the fans were required in veto. This gave an assignment of channels as follows: 1-C1 veto (pulses bigger than pions); 2-Berkeley No. 1, C_A + C2; 3-Berkeley No. 2 in veto, Fans + C3; 4-C1; 5-C2; 6-C3. In Configuration D the upper veto limit on C1 was replaced by the requirement of a Čerenkov signal in coincidence and the channel assignment was: 1-C1; 2- C_A+C2; 3- Fan + C3 in veto; 4- C_A+C2; 5-C3; 6- Čerenkov + C3. Channel 6 was also operated in veto for proton runs, which were needed to correct for the inefficiency of the Čerenkov counter discrimination against protons. The output signals from the slow coincidence circuit were counted with a decimal scaler and were used to trigger the oscilloscope. The traces on the scope were photographed and used to adjust biases on the discriminator and to monitor recorded counts throughout the experiment as a check on operation of the

electronics.

Since there were not enough channels on the slow coincidence circuit to allow for monitoring of "electron" counts in C3, the signal from this counter was delayed by 0.4 microsecond to coincide in timing with the output from the slow coincidence circuit and the two signals were fed into a Model 100 coincidence circuit (0.15 microsecond resolving time) with the biases adjusted to accept all output signals from the slow coincidence circuit but only the pulses from C3 more than 2.5 times the minimum ionizing pulse height. The output from this circuit was counted in the "electron" counter and used as a monitor on the possible electron contribution, as described in an earlier section.

The singles counting rate in various counters was monitored from time to time. This required a fast binary scaler operating a normal decimal scaler, since the counting rates were higher than the resolution of the decimal scaler could tolerate without losses. These singles rates were useful in insuring that the accidental counts were negligible at all times.

IV. DATA REDUCTION

This section treats the problems associated with the calculation of cross sections from the observed counting rates and the corrections and uncertainties connected with this process.

A. Cross Section Formulae

The observed counting rate from a reaction of the two body type, such as equation 1, may be expressed in the following differential form:

$$dC = \sigma(k, \theta') \frac{\partial \Omega'}{\partial \Omega} R A_\pi N_H N(k) n(x, y) dx dy dz dk d\Omega , \qquad (10)$$

where C = number of observed counts.

$\sigma(k, \theta')$ = differential cross section for reaction to produce a pion in $d\Omega'$ at θ' from a photon of energy k.

$\frac{\partial \Omega'}{\partial \Omega}$ = transformation from c. m. solid angle to lab solid angle

R = correction for pion decay in flight and for muon contamination resulting therefrom.

A_π = correction for absorption of pions throughout system.

N_H = the number of hydrogen nuclei per unit volume effective in the reaction. This is just $\frac{\rho_H N_o}{M}$, where N_o is Avrogadro's number, M is the atomic weight of hydrogen and ρ_H is the effective density of hydrogen.

$N(k)\,dk$ = the number of photons with energy from k to k + dk. This is the N(k)dk in equations 7 and 9.

$n(x, y)$ = the spatial density of the beam at the target, as described in table 3.

x, y, z = spatial coordinates in the hydrogen target and beam interaction volume, z being the beam direction and

x vertical along the axis of the cylindrical cup holding the hydrogen.

$d\Omega$ = lab solid angle increment.

To obtain the total counting rate it is necessary to integrate over the variables shown. The limits are set by the interaction volume in the target for x, y, and z and the spectrometer configuration for k and Ω . This is a complicated integration, since the spectrometer properties change with position in the target, and the kinematical quantities also vary with photon energy and position. Where the various quantities are slowly varying functions over the ranges of integration the counting rate may be approximated by using averages of these quantities in arriving at an expression for the differential cross section in terms of known or calculable quantities. Where the entire spectrometer window is employed in a measurement, the expression becomes:

$$\sigma(k, \theta^{\prime}) = C/K \tag{11}$$

where $$K = \left(\frac{\partial \Omega^{\prime}}{\partial \Omega}\right)_{av} \Delta\Omega \, R \, A_{\pi} \, N_H \, \bar{\ell} \, N_k \left(\frac{\partial k}{\partial p}\right)_{av} \frac{\Delta p}{p_o} \, p_o \tag{12}$$

in which the quantities shown are now averages over the various variables, and we replaced dk by $\left(\frac{\partial k}{\partial p}\right)_{\theta} dp$ and averaged to get $\left(\frac{\partial k}{\partial p}\right)_{av} \Delta p$. The mean path length for the beam through the hydrogen target is the quantity $\bar{\ell}$ and $N_H \bar{\ell}$ is the number of effective protons per unit area in the beam. N_k is the number of photons of average energy k per Mev irradiating the target and is represented by $\frac{W \, B(k, E_o)}{E_o \, k}$ for a BIP. $\Delta\Omega$ is the average solid angle of the spectrometer, as given in table 1 for the various configurations. This

formula is the useful expression required to evaluate the differential cross section using a spectrometer of solid angle $\Delta\Omega$ and dispersion $\frac{\Delta p}{p_o}$ for a given reaction, which determines $\frac{\partial k}{\partial p}$ and $\frac{\partial \Omega'}{\partial \Omega}$.

For measurements where the end point of the bremsstrahlung, E_o, fell below the acceptance limit for photon energies defined by the limit of momentum of the spectrometer it was necessary to perform the integration using the Datatron Digital Computer and a program coded by P. L. Donoho and modified by F. Dixon to obtain the integrals required by the reaction, beam, target, and spectrometer configurations used in this experiment. This treatment was required for the k = 1000 Mev points, but was not needed for any others. For the lower energy points it was always possible to arrange the end point energy of the beam to fall above the upper photon energy accepted by the spectrometer in the reaction studied. In effect the computer performed an integration given by:

$$K = \int\int\int \frac{\partial k}{\partial p} \frac{\partial \Omega'}{\partial \Omega} \frac{B(k, E_o)}{k} \, d\Omega \, dk \, n(x, y) \, dx \, dy \, dz. \qquad (13)$$

To obtain the differential cross section we must multiply by the factors $\frac{W}{E_o}$, R, A_π, and $\frac{\rho_H N_o}{M}$ to obtain $\mathcal{K}$ and divide $\mathcal{K}$ into the counting rate to get $\sigma(k, \theta')$. We can now give the general formula to convert counting rates into cross sections. For both types of calculations we have simply:

$$\sigma(k, \theta') = \frac{C}{\mathcal{K}} \qquad (14)$$

where we understand that $\mathcal{K}$ is either equation 12 or K of equation 13 multiplied by the appropriate factors mentioned in the sentence

following the equation.

The quantities in K must be evaluated at the mean values of the pion momentum and photon energy defined by the setting of the spectrometer angle θ_o and the mean momentum p_o. In this experiment there was a loss in momentum before entering the magnet and the average mean momentum at the center of the target, p_o^s, is the value required for the proper evaluation of K. The functions $\frac{\partial \Omega'}{\partial \Omega}$ and $\frac{\partial k}{\partial p}$ are evaluated at k and p_o^s in the expression of equation 12 to give the proper relation between cross section and counting rate, and $\frac{\Delta p}{p_o}$ is multiplied by $\frac{p_o}{p_o^s}$ to correct for momentum loss.

The correction factors R and A_π are required, since every particle emitted in the reaction under study does not result in a recorded count. R includes the decay loss of pions, R_π, and the contamination addition of muons, R_m, resulting from the pion decay. A_π makes allowance for the loss of pions due to nuclear absorption throughout the system. These effects are discussed in the next section along with the corrections required to convert the observed counting rate to the pion counting rate for cross section calculations.

B. Corrections

The counting rates recorded with a full target, C_T, must be adjusted by several factors to arrive at the effective hydrogen contribution to the counting rate, which is attributable to pion effects. In all configurations the background counting rate, C_B, had to be subtracted. In the forward angle runs using Configuration D the proton contamination due to the Čerenkov inefficiency

for proton rejection had to be subtracted in both the full target and background runs. Thus, C_T had to be reduced by C_p and C_B had to be reduced by C_{pB} before the "pion" counts could be ascertained. The result was the uncorrected pion counting rate from the hydrogen, C_u, which had to be increased to account for the pion loss due to the Čerenkov inefficiency. The various counting rates, corrections, and experimental parameters are given in table V. The counting rate, C, called the net pion counting rate, includes muons and pions and is to be used in the formula for the differential cross section given in equation 14. The factor $R = R_\pi + R_m$ corrects for the decayed pions lost and the muons which give counts indistinguishable from the pions. R_π is just the fraction of pions which pass through the spectrometer and counters without decaying and is calculated using the mean lifetime $t_\pi = (2.56 \pm .05) \times 10^{-8}$ seconds. The expression found to be most useful with magnets employs the mean spectrometer momentum to give an average for a given run of

$$R_\pi = \exp(-S/2.157p_o) \tag{15}$$

with S = target-to-C2 mean path length in inches.

R_m makes allowance for the muon counts, some of which come from pions which would have been counted if no decays occurred and others which are decay products from pions, whose angle of emission or momentum was such that they would not have given a count. The details of the calculation of R are given in the Appendix. This involved an integration over the pion

spectrum emitted from the target as a function of the energies in the beam, the angles of emission, the dynamics of the decay, and the limitations set by the spectrometer geometry and the magnetic field. The problem was not tractable for an exact calculation, so an approximate solution was obtained with an estimated uncertainty of 15%. The correction was of the order of ten per cent of the total counting rate and the uncertainty of 1.5% in the final results was not significant in light of the errors of 5 to 10% resulting from statistics.

The correction for nuclear absorption involved the losses in the lead absorber in front of C3 and the counters $C_{A,0}$, C1, C2, and C3 plus the Čerenkov. The absorption effect was determined by placing lead in the system and comparing the counting rates with the extra lead to those with only the half inch normally used. In general the effect was compatible with the geometrical cross section in agreement with the absorption measurements for pions (22) in the energy range from 100 Mev to 1 Bev. The notable exception to this statement came at $p_o = 577$ Mev, where the cross section for absorption was apparently lower than geometrical. The mean path obtained in the measurement was $L = 22.7 \pm 6.99$ cm of lead compared to the geometrical value $L_g = 14.7$ cm from

$$L_g = \frac{M_{Pb}}{N_o \pi R_o^2 A_{Pb}^{2/3} (\text{density})} \quad , \tag{16}$$

in which L_g is the mean path in centimeters

M_{Pb} is the atomic weight of lead = 207.2

N_o is Avrogadro's number

R_o is effective nucleon radius = 1.37×10^{-13} cm.

A_{Pb} is the mass number of lead =

and density is 11.35 gm/cc for the lead employed. In view of the poor statistics associated with this particular measurement it is felt that the use of the geometrical value is not inconsistent with the result obtained, since the other measured values for the mean absorption length from 250 Mev/c to 950 Mev/c were in general agreement with this choice. The values shown in table 1 under A_π include the geometrical cross section for the counters and absorber in the various configurations including the material in which a positive pion may be absorbed. The counters are considered to be $(CH)_n$ for the scintillaters and $C_5H_8O_2$ for the Lucite Čerenkov. The correction was calculated for all material except the hydrogen using a density of 1.052 for the scintillation plastic and 1.18 gm/cc for the Lucite. The error assigned to the absorption correction is 15% of the correction based on the errors quoted in the original interaction measurements of pions in lead. In the worst case this could result in an assignment of a 3% error in the final result, which has a small effect compared to the 5-10% statistical error. The original studies (22) of pion interactions with various nuclei on which this choice is based were accomplished in a good geometry attenuation measurement and include some effects of scattering out of the beam not included in nuclear absorption effects. These may have been reduced in this experiment by the location of the lead absorber close to the rear counter, but should have been present in the effects assigned to the other counters, which were some distance

away (see table 4).

C. Errors

The corrections introduce uncertainties in the final results, as do the counting statistics, errors in determination of experimental parameters, etc. These may be classified, according to the effect on the data, as systematic or random errors. The systematic errors are assumed to affect the data uniformly, and the random errors differ from point to point in a nonuniform manner. The errors follow according to classification.

I. Systematic Errors

a. Beam monitoring - 3% in calibration.

b. Errors in the spectrometer solid angle, mean momentum, and momentum dispersion constant - all 3%.

c. Error in the nuclear absorption corrections - 15% of the correction.

II. Random Errors

a. Muon contamination correction error - 15% of the correction.

b. Statistical counting errors in the form of standard deviations - 5 to 8%.

The errors quoted in the final results are those in group II, since they affect the angular distributions by varying in value from point to point.

V. RESULTS

The primary objective of this experiment was to obtain good angular distributions for the five photon energies, k = 600, 700, 800, 900, and 1000 Mev. This was to include eleven points for each energy in the angular range from 20° to 165° in the c.m. system. Some of these points were measured in more than one configuration, so the total number of measured points exceeded the original 55. Since the data were obtained in different geometries, each measurement is indicated separately in the various tables when more than one configuration was used.

Table 5 shows the experimental information and data for each of the seventy-five points. Each point is designated by its nominal energy - c.m. angle, configuration for easy identification. The table is arranged so the information for each of the five values of k is on a single page. The odd energy points measured at $\theta_{cm} = 90^{\circ}$ are given on a separate page with the subtitle "Odd Energies at 90°." The item of ultimate interest is the net "pion" counting rate C, from which the value of $\sigma(k, \theta_{cm})$ is derived.

Table 6 shows the results obtained from the measurements in a form similar to the one used in table 5. The last column on each page gives the differential cross section with the quoted error, which is a result of compounding the relative statistical counting error with the relative error assigned to the muon correction.

The angular distributions for the five different photon energies are given in figures 8 to 12. In the earlier runs the mean value of k differed slightly from the desired nominal value. Thus,

Table 5

Experimental Information and Data

Point : The particular experimental measurement represented by Nominal Photon Energy - c.m. Angle, Configuration. e.g. 600 - 90 A is the k = 600 Mev, θ_{cm} = 90 degrees point measured in Configuration A.

k : Mean photon energy, Mev.

θ_{cm} : Pion angle in the center-of-momentum system, degrees.

p_o : Mean momentum of spectrometer, Mev/c.

p_o^s : Effective momentum at the center of the hydrogen target = $p_o + \Delta p$, where Δp is the momentum lost in front of the magnet, Mev/c.

E_o : Peak bremsstrahlung energy, Mev.

C_T : Full target counting rate per standard BIP.

C_B : Background counting rate.

C_p : Counting rate due to proton contamination of C_T as result of Čerenkov rejection inefficiency.

C_{pB} : Proton contribution to background.

C_u : Pion counting rate uncorrected for Čerenkov efficiency.

C : Net pion counting rate to be used in data reduction with the statistical standard deviation.

All counting rates have the "electron" counts subtracted from the slow coincidence counts, since these "electron" counts are really absorption effects in the Pb absorber and are part of the absorption correction in equations 10 to 14.

Table 5 - Odd Energies at 90^{o}

Point	k	θ_{cm}	θ_o	p_o	p_o^s	E_o
450-90A	456.1	90^{o}	69.3	316.8	320.6	550
500-90A	506.9	90^{o}	68.0	352.0	355.8	600
550-90A	555.8	90^{o}	66.8	383.5	387.3	650
650-90A	657.8	90^{o}	64.6	446.2	450.1	750
750-90A	754.8	90^{o}	62.6	505.0	508.9	850
550-90B	555.6	90^{o}	66.8	383.5	387.3	650
650-90B	658.0	90^{o}	64.6	446.3	450.2	750
750-90B	756.8	90^{o}	62.6	506.0	509.9	850
600-90B	609.6	90^{o}	65.7	416.5	420.3	700
700-90B	702.7	90^{o}	63.6	474.5	478.4	800
800-90B	803.9	90^{o}	61.6	534.0	537.9	920
900-90B	901.9	90^{o}	59.8	591.0	594.9	1000

Point	C_T	C_B	C_p	C_{pB}	C_u	C
450-90A	1.93	.043				1.89± .14
500-90A	1.84	.041				1.80± .12
550-90A	2.17	.048				2.12± .08
650-90A	2.57	.057				2.51± .09
750-90A	2.46	.054				2.41± .11
550-90B	0.93	.020				0.91± .04
650-90B	1.28	.028				1.26± .06
750-90B	1.03	.023				1.01± .05
600-90B	1.12	.024				1.10± .05
700-90B	1.39	.029				1.36± .04
800-90B	0.64	.022				0.62± .03
900-90B	0.42	.012				0.41± .02

Table 5 - 600 Mev

Point	k	θ_{cm}	θ_o	p_o	p_o^s	E_o
600-20D	600.0	20°	13.1	568.9	572.2	700
600-30D	600.0	30°	19.7	556.8	560.0	700
600-30A	600.4	30°	19.7	557.0	560.9	700
600-45A	601.8	45°	30.1	531.7	535.6	700
600-60A	604.0	60°	41.1	497.2	501.1	700
600-75A	605.5	75°	52.8	459.8	463.6	700
600-90A	608.3	90°	65.7	415.8	419.6	700
600-105A	609.3	105°	80.0	371.4	375.2	700
600-120A	612.1	120°	96.1	330.7	334.5	750
600-135A	612.5	135°	114.2	293.0	296.8	750
600-150C	600.0	150°	134.4	261.5	264.7	800
600-162C	600.0	161.7°	151.5	246.5	249.7	800

Point	C_T	C_B	C_p	C_{pB}	C_u	C
600-20D	1.54	.12			1.418	1.443±.085
600-30D	1.42	.14			1.287	1.310±.077
600-30A	6.15	.59				5.57 ±.20
600-45A	5.69	.21				5.48 ±.18
600-60A	4.58	.13				4.45 ±.15
600-75A	3.80	.072				3.72 ±.17
600-90A	2.22	.053				2.17 ±.10
600-105A	1.39	.033				1.36 ±.07
600-120A	.955	.023				.932±.044
600-135A	.610	.015				.595±.032
600-150C	.414	.034				.380±.022
600-162C	.380	.076				.304±.025

Table 5 - 700 Mev

Point	k	θ_{cm}	θ_o	p_o	p_o^s	E_o
700-20D	700.0	20	12.6	668.5	672.0	800
700-30D	700.0	30	19.0	653.7	657.2	800
700-45D	700.0	45	28.9	620.9	624.3	800
700-60D	700.3	60	39.5	577.9	581.4	800
700-60C	700.0	60	39.5	577.9	581.2	800
700-60A	700.0	60	39.5	577.3	581.2	800
700-75C	700.0	75	51.0	527.8	531.0	800
700-75A	704.6	75	51.0	530.0	533.9	800
700-90A	702.1	90	63.6	474.2	478.0	800
700-105A	712.2	105	77.7	423.3	427.1	800
700-120A	712.5	120	93.7	370.6	374.4	850
700-135A	715.7	135	111.9	325.8	329.6	850
700-150C	700.0	150	132.7	286.9	290.1	900
700-163C	700.0	162.5	151.5	267.2	270.4	900

Point	C_T	C_B	C_p	C_{pB}	C_u	C
700-20D	1.615	.178			1.437	1.462±.074
700-30D	1.362	.138			1.224	1.246±.068
700-45D	1.322	.142			1.180	1.198±.062
700-60D	1.210	.116			1.094	1.113±.046
700-60C	4.03	.30				3.73 ±.090
700-60A	4.92	.13				4.79 ±.13
700-75C	3.27	.24				3.03 ±.12
700-75A	4.21	.10				4.11 ±.20
700-90A	3.02	.06				2.96 ±.10
700-105A	1.87	.03				1.84 ±.09
700-120A	1.091	.015				1.076±.05
700-135A	.702	.008				0.695±.034
700-150C	.415	.044				0.371±.026
700-163C	.346	.064				0.282±.023

Table 5 - 800 Mev

Point	k	θ_{cm}	θ_o	p_o	p_o^s	E_o
800-20D	800	20	12.0	768.3	771.8	900
800-30D	800	30	18.3	749.5	753.1	900
800-45D	800	45	27.9	709.5	713.0	900
800-60D	800	60	38.1	658.7	662.2	900
800-75D	800	75	49.3	597.7	601.2	900
800-75C	800	75	49.3	597.7	601.0	900
800-75A	798.4	75	49.3	596.0	599.9	920
800-90C	800	90	61.6	533.2	536.4	900
800-90A	806.0	90	61.6	535.0	538.9	920
800-105A	810.1	105	75.5	470.0	473.8	920
800-120A	812.9	120	91.6	409.0	412.8	950
800-135A	814.8	135	109.9	353.8	357.6	950
800-150C	800	150	131.1	309.3	312.5	1000
800-163C	796.1	163.2	151.5	284.2	287.4	1000

Point	C_T	C_B	C_p	C_{pB}	C_u	C
800-20D	1.202	.098	.011	.005	1.098	1.117±.054
800-30D	1.054	.131	.005	.001	.919	.936±.054
800-45D	.902	.125	.002	.001	.776	.790±.041
800-60D	.709	.128			.581	.591±.040
800-75D	.508	.050			.458	.466±.019
800-75C	1.777	.136				1.64 ±.81
800-75A	2.527	.076				2.451±.112
800-90C	1.383	.114				1.269±.061
800-90A	1.562	.048				1.514±.059
800-105A	1.183	.049				1.159±.051
800-120A	.820	.015				.805±.039
800-135A	.541	.009				.532±.029
800-150C	.334	.029				.305±.019
800-163C	.289	.049				.240±.019

Table 5 - 900 Mev

Point	k	θ_{cm}	θ_o	p_o	p_o^s	E_o
900-20D	900	20	11.6	866.3	870.0	990
900-30D	900	30	17.6	844.7	848.4	990
900-45D	900	45	26.9	798.7	802.3	990
900-60D	900	60	36.8	738.5	742.1	1000
900-75D	900	75	47.7	667.2	670.8	1000
900-90A	900.9	90	59.8	590.5	594.4	1000
900-105A	908.0	105	73.6	516.0	519.9	1000
900-120A	915.7	120	89.4	445.0	448.8	1000
900-135A	923.6	135	108.0	383.0	386.8	1080
900-135C	900	135	108.0	378.6	381.8	1080
900-150C	900	150	129.6	328.4	332.2	1080
900-164C	900	163.8	151.5	299.2	303.0	1080

Point	C_T	C_B	C_p	C_{pB}	C_u	C
900-20D	1.152	.123	.017	.007	1.019	1.037±.055
900-30D	1.057	.122	.011	.004	.928	.944±.059
900-45D	.930	.088	.007	.003	.838	.853±.049
900-60D	.570	.072	.003	.001	.496	.505±.029
900-75D	.316	.052			.264	.269±.018
900-90A	.918	.027				.891±.043
900-105A	.786	.020				.766±.039
900-120A	.661	.014				.647±.031
900-135A	.554	.011				.543±.026
900-135C	.441	.020				.421±.025
900-150C	.285	.013				.272±.017
900-164C	.263	.028				.235±.016

Table 5 - 1000 Mev

Point	k	θ_{cm}	θ_o	p_o	p_o^s	E_o
1000-20D	1000	20	11.3	965.3	969.0	1080
1000-30D	1000	30	17.0	940.3	944.0	1080
1000-45D	1000	45	26.1	886.3	890.0	1080
1000-60D	1000	60	35.7	816.9	820.5	1080
1000-75D	1000	75	46.3	737.7	741.3	1080
1000-86D	1000	86.1	55.0	672.0	675.6	1080
1000-105A	1000	105	71.7	559.7	563.6	1080
1000-120A	1000	120	87.6	479.2	481.1	1080
1000-135A	1000	135	106.1	408.2	412.0	1080
1000-150C	1000	150	127.9	352.8	356.0	1080
1000-164C	1000	164.2	151.5	318.5	321.7	1080

Point	C_T	C_B	C_p	C_{pB}	C_u	C
1000-20D	1.006	.160	.027	.010	.829	.844±.047
1000-30D	1.143	.139	.021	.006	.989	1.007±.045
1000-45D	1.184	.087	.011	.005	1.091	1.110±.045
1000-60D	.752	.066	.004	.001	.683	.696±.039
1000-75D	.328	.032	.002	.001	.296	.301±.018
1000-86D	.190	.022			.168	.171±.011
1000-105A	.620	.032				.588±.027
1000-120A	.550	.018				.532±.023
1000-135A	.424	.013				.411±.020
1000-150C	.230	.019				.211±.016
1000-164C	.156	.022				.134±.011

Table 6

Results

Point : As in Table 5.

R_π : Fraction of pions which remain in passing from center of target to defining counter at the rear focus.

R_m : Fraction of net counting rate due to muon contamination calculated as described in the Appendix.

R : Net decay correction = $R_\pi + R_m$ with estimated error in R_m indicated by ϵ_R.

K : Number which must be divided into the number of counts per BIP to convert counting rate into a differential cross section, counts per BIP per microbarn/steradian.

$\sigma(k, \theta_{cm})$: Differential cross section in microbarns per steradian. Error is the standard deviation, including ϵ_R and the statistical counting error at each point.

Table 6 - Results

Point	R_π	R_m	$R \pm \varepsilon_R$	K	$\sigma(k, \theta_{cm})$
450-90A	.7854	.0994	.8849 ± .0149	.3467	5.44 ± 0.41
500-90A	.8047	.0914	.8961 ± .0137	.3540	5.09 ± 0.36
550-90A	.8191	.0814	.9005 ± .0122	.3541	5.99 ± 0.24
650-90A	.8425	.0669	.9094 ± .0100	.3543	7.10 ± 0.27
750-90A	.8594	.0558	.9152 ± .0084	.3528	6.82 ± 0.32
550-90B	.8191	.0814	.9005 ± .0122	.1569	5.77 ± 0.27
650-90B	.8425	.0669	.9094 ± .0100	.1569	8.00 ± 0.38
750-90B	.8594	.0558	.9152 ± .0084	.1564	6.44 ± 0.31
600-90B	.8319	.0728	.9047 ± .0109	.1582	6.94 ± 0.33
700-90B	.8510	.0622	.9132 ± .0093	.1566	8.69 ± 0.29
800-90B	.8668	.0552	.9220 ± .0083	.1538	4.00 ± 0.16
900-90B	.8785	.0465	.9250 ± .0070	.1552	2.61 ± 0.13
600-20D	.8087	.0964	.9051 ± .0145	.1188	12.15 ± 0.74
600-30D	.8050	.0978	.9028 ± .0147	.1157	11.32 ± 0.69
600-30A	.8716	.0630	.9346 ± .0095	.5133	10.84 ± 0.41
600-45A	.8660	.0646	.9306 ± .0097	.4849	11.29 ± 0.39
600-60A	.8574	.0668	.9242 ± .0100	.4459	9.98 ± 0.36
600-75A	.8467	.0682	.9149 ± .0102	.4034	9.23 ± 0.44
600-90A	.8319	.0728	.9047 ± .0109	.3540	6.11 ± 0.28
600-105A	.8138	.0777	.8915 ± .0117	.3051	4.45 ± 0.24
600-120A	.7935	.0935	.8870 ± .0140	.2491	3.75 ± 0.18
600-135A	.7702	.1014	.8716 ± .0152	.2089	2.85 ± 0.16
600-150C	.7464	.1091	.8555 ± .0164	.1343	2.83 ± 0.17
600-162C	.7332	.1103	.8435 ± .0165	.1217	2.50 ± 0.20

Table 6 - Results

Point	R_π	R_m	$R \pm \varepsilon_R$	K	$\sigma(k, \theta_{cm})$
700-20D	.8347	.0809	.9156 ± .0121	.1209	12.10 ± 0.65
700-30D	.8313	.0806	.9119 ± .0121	.1175	10.60 ± 0.60
700-45D	.8232	.0816	.9048 ± .0122	.1103	10.86 ± 0.58
700-60D	.8112	.0950	.9062 ± .0143	.1021	10.89 ± 0.49
700-60C	.8761	.0570	.9331 ± .0086	.3604	10.36 ± 0.26
700-60A	.8759	.0625	.9384 ± .0094	.4531	10.58 ± 0.29
700-75C	.8650	.0542	.9192 ± .0081	.3187	9.51 ± 0.39
700-75A	.8656	.0567	.9223 ± .0085	.4034	10.19 ± 0.50
700-90A	.8510	.0622	.9132 ± .0093	.3534	8.39 ± 0.29
700-105A	.8347	.0644	.8991 ± .0097	.3029	6.08 ± 0.29
700-120A	.8135	.0795	.8930 ± .0119	.2462	4.37 ± 0.21
700-135A	.7907	.0870	.8777 ± .0131	.2054	3.38 ± 0.17
700-150C	.7660	.0929	.8589 ± .0139	.1337	2.77 ± 0.20
700-163C	.7510	.0968	.8478 ± .0145	.1172	2.41 ± 0.20
800-20D	.8545	.0683	.9228 ± .0103	.1228	9.09 ± 0.45
800-30D	.8512	.0701	.9213 ± .0105	.1192	7.81 ± 0.46
800-45D	.8434	.0714	.9148 ± .0107	.1118	7.07 ± 0.38
800-60D	.8325	.0750	.9075 ± .0113	.1030	5.74 ± 0.40
800-75D	.8170	.0786	.8956 ± .0118	.0910	5.12 ± 0.22
800-75C	.8799	.0464	.9263 ± .0070	.3200	5.13 ± 0.25
800-75A	.8796	.0522	.9318 ± .0078	.3990	6.14 ± 0.28*
800-90C	.8663	.0501	.9164 ± .0075	.2792	4.55 ± 0.22
800-90A	.8668	.0552	.9220 ± .0083	.3473	4.36 ± 0.17
800-105A	.8497	.0588	.9085 ± .0088	.2965	3.91 ± 0.17
800-120A	.8294	.0682	.8976 ± .0102	.2435	3.31 ± 0.16
800-135A	.8056	.0753	.8809 ± .0113	.2005	2.66 ± 0.15
800-150C	.7805	.0848	.8653 ± .0127	.1277	2.39 ± 0.15
800-163C	.7640	.0856	.8496 ± .0128	.1122	2.14 ± 0.16

*Shifting Magnet current throughout this run.

Table 6 - Results

Point	R_π	R_m	$R \pm \varepsilon_R$	K	$\sigma(k, \theta_{cm})$
900-20D	.8699	.0577	.9276 ± .0087	.1247	8.31 ± 0.45
900-30D	.8668	.0583	.9251 ± .0087	.1212	7.79 ± 0.49
900-45D	.8604	.0603	.9207 ± .0090	.1137	7.50 ± 0.44
900-60D	.8492	.0657	.9149 ± .0099	.1032	4.89 ± 0.28
900-75D	.8344	.0696	.9040 ± .0104	.0916	2.93 ± 0.20
900-90A	.8785	.0465	.9250 ± .0070	.3506	2.54 ± 0.12
900-105A	.8622	.0508	.9130 ± .0076	.2972	2.58 ± 0.13
900-120A	.8421	.0554	.8975 ± .0083	.2466	2.62 ± 0.13
900-135A	.8190	.0694	.8884 ± .0104	.1757	3.09 ± 0.15
900-135C	.8170	.0717	.8887 ± .0108	.1488	2.83 ± 0.17
900-150C	.7922	.0741	.8663 ± .0111	.1248	2.18 ± 0.14
900-164C	.7744	.0780	.8524 ± .0117	.1088	2.16 ± 0.15
1000-20D	.8824	.0486	.9310 ± .0073	.1266	6.67 ± 0.38
1000-30D	.8795	.0490	.9285 ± .0074	.1288	8.45 ± 0.39
1000-45D	.8727	.0536	.9263 ± .0080	.1191	10.05 ± 0.42
1000-60D	.8626	.0546	.9172 ± .0082	.1079	6.96 ± 0.41
1000-75D	.8490	.0572	.9062 ± .0086	.0936	3.47 ± 0.21
1000-86D	.8355	.0612	.8967 ± .0092	.0831	2.21 ± 0.14
1000-105A	.8722	.0422	.9144 ± .0063	.2787	2.28 ± 0.11
1000-120A	.8525	.0481	.9006 ± .0072	.2000	2.87 ± 0.12
1000-135A	.8291	.0549	.8840 ± .0082	.1405	3.16 ± 0.15
1000-150C	.8051	.0541	.8592 ± .0081	.0862	2.64 ± 0.20
1000-164C	.7865	.0587	.8452 ± .0088	.0661	2.19 ± 0.19

in Configurations A and B the mean photon energy indicated under k in table 5 differs from the nominal value in the point designation. The difference in the differential cross section, which could result from these photon differences, was much less than the error and was neglected in the angular distributions. The worst case was the one cited in section III, where the k = 923.6 Mev value was 2.6% above the desired value of 900 Mev.

The notable features of the angular distributions are the front to back asymmetry present at all five values of k and the sudden appearance of the two strong humps in the k = 1000 Mev distribution with the minimum near 90° and the maxima close to 45° and 135°. This feature is entirely absent from the 800 Mev data and is indicated only slightly in the 900 Mev data. The angular distributions have been fitted by the Least Squares Method to two types of equations involving expansion in polynomials of $\text{Cos}\ \theta_{cm}$. The first of these is the standard polynomial expansion used for the analysis of the lower energy measurements of both charged and neutral pions. The expression has the following form:

$$\sigma(k,\theta) = \sum_{n=0}^{n=N} A_n \text{Cos}^n\theta \qquad (17)$$

where N is the highest power of Cos θ for the particular attempt at fitting the data, and θ is the center-of-momentum angle. The curves of this type are represented by solid lines in the figures. The highest power of Cos θ required to give a reasonable fit is N = 4 for k = 600, 700, and 800. The N = 4 fit for 900 Mev is not good, thus, the k = 900 and k = 1000 Mev data require N = 6.

Figures 8-12. Angular Distributions for Single Positive Pions Photoproduced from Hydrogen.

The letters A, B, C, and D refer to the configuration in which the data were obtained.

The x's are values interpolated from the Cornell measurements (8).

The solid curves represent least squares fits to the data reported here given by

$$\sigma_{cm}(k,\theta) = \sum_{n=0}^{N} A_n \mathrm{Cos}^n\theta$$

with N = 4 for k = 600, 700, and 800 Mev in figures 8, 9, and 10. N = 6 for k = 900 and 1000 Mev in figures 11 and 12.

The dashed curves are least squares fits of the form

$$\sigma_{cm}(k,\theta) = \frac{1}{(1-\beta\mathrm{Cos}\theta)^2} \sum_{n=0}^{N} B_n \mathrm{Cos}^n\theta$$

as prescribed by Moravcsik (23). β is the pion velocity relative to the velocity of light and taken in the c.m. system. For this expression N = 6 was required for the illustrated curves. For k = 800 Mev N = 4 was very nearly the same as the N = 6 curve, but the latter was given for consistency.

Little confidence is to be placed in the behavior of these dashed curves forward of $\theta = 20^\circ$, where no data were taken.

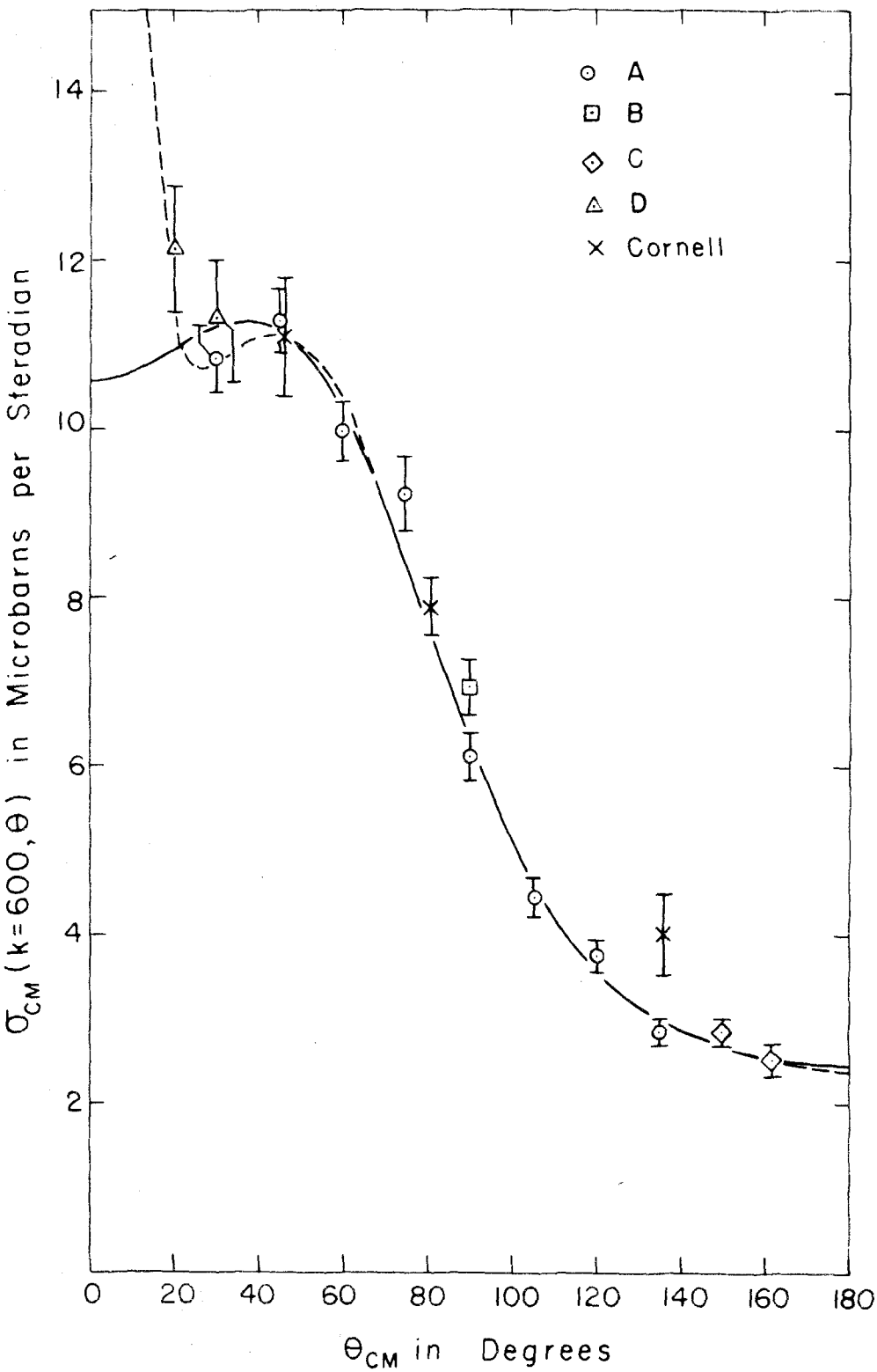
A
B
C
D
Cornell
14
12
10
8
6
4
2
0
20
40
60
80
100
120
140
160
180
σ_{CM} (k=600, θ) in Microbarns per Steradian
θ_{CM} in Degrees

Figure 8

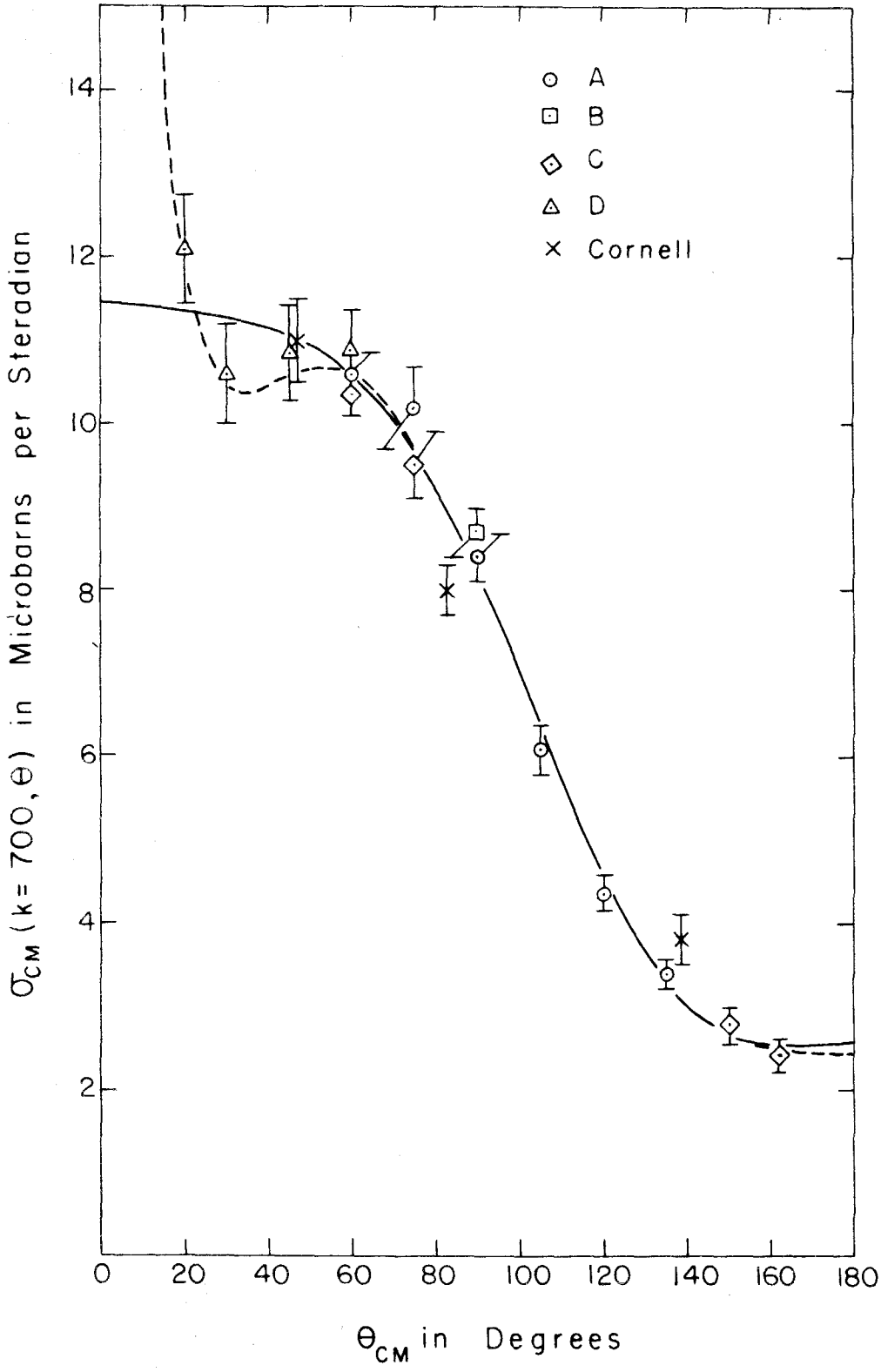
A
B
C
D
Cornell
14
12
10
8
6
4
2
0
20
40
60
80
100
120
140
160
180
σ_{CM} (k= 700, θ) in Microbarns per Steradian
θ_{CM} in Degrees

Figure 9

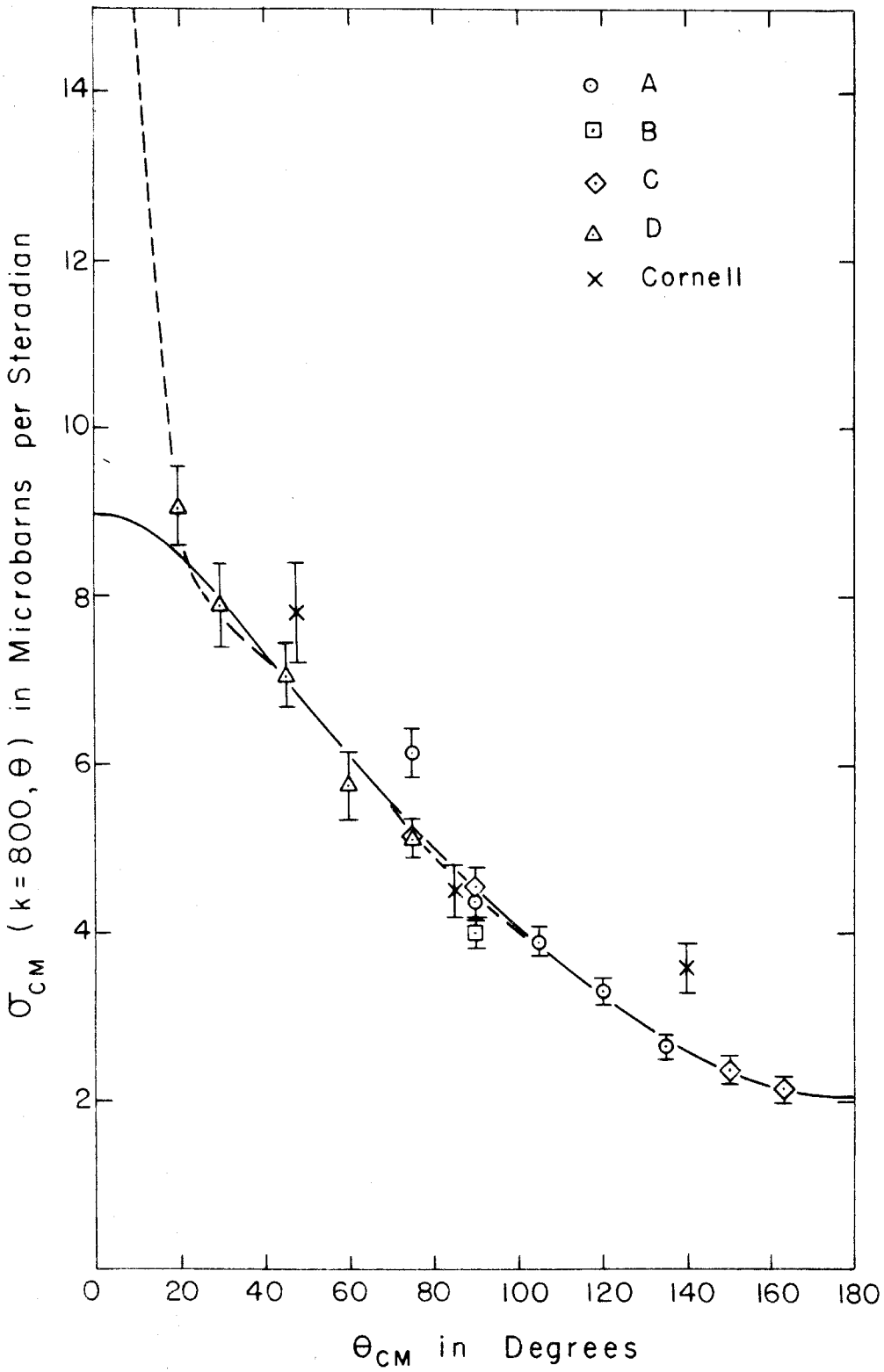
A
B
C
D
Cornell
14
12
10
8
6
4
2
0
20
40
60
80
100
120
140
160
180
σ_{CM} (k = 800, θ) in Microbarns per Steradian
θ_{CM} in Degrees

Figure 10

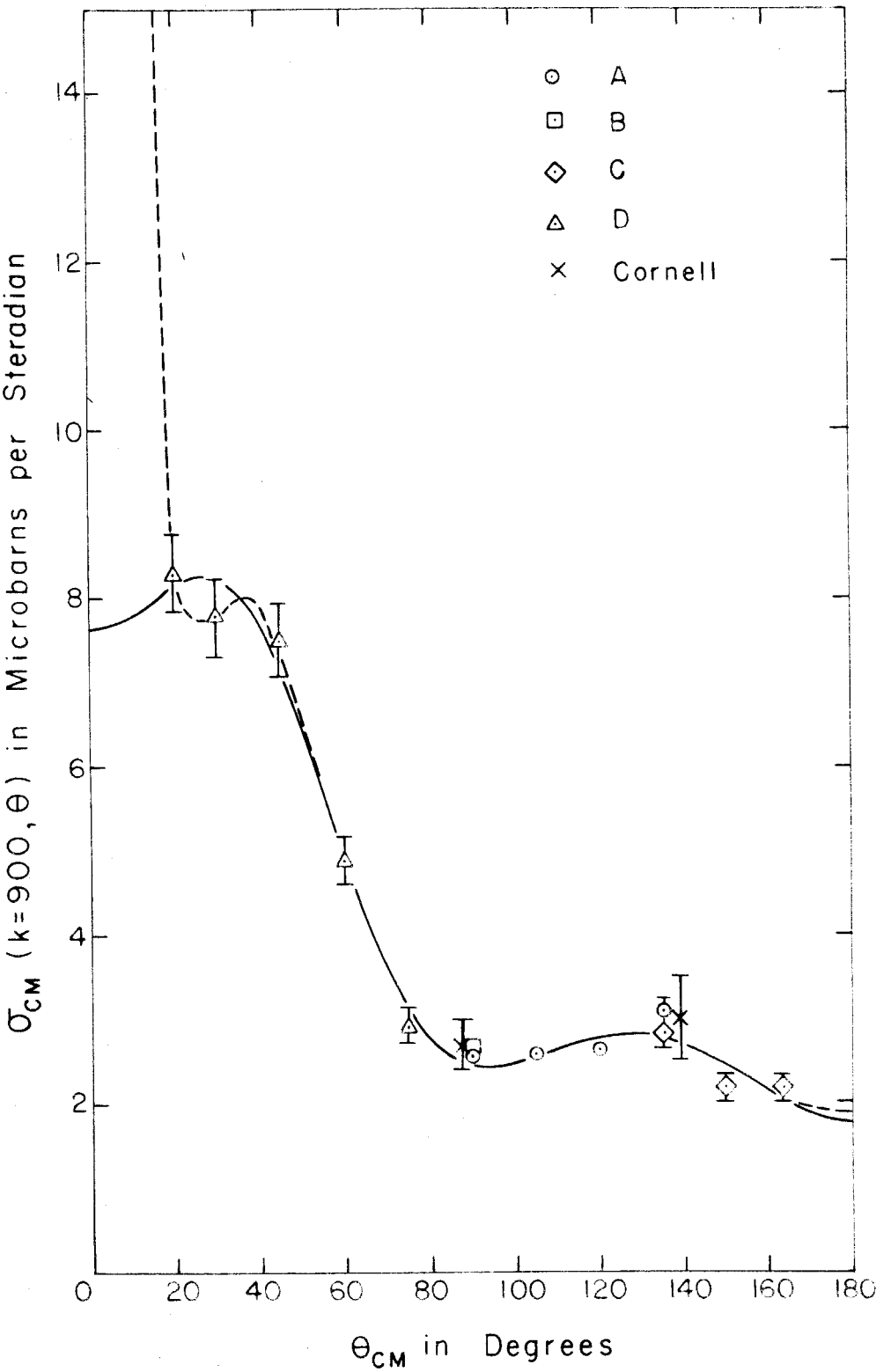
A
B
C
D
Cornell
14
12
10
8
6
4
2
0
20
40
60
80
100
120
140
160
180
σ_{CM} (k=900, θ) in Microbarns per Steradian
θ_{CM} in Degrees

Figure II

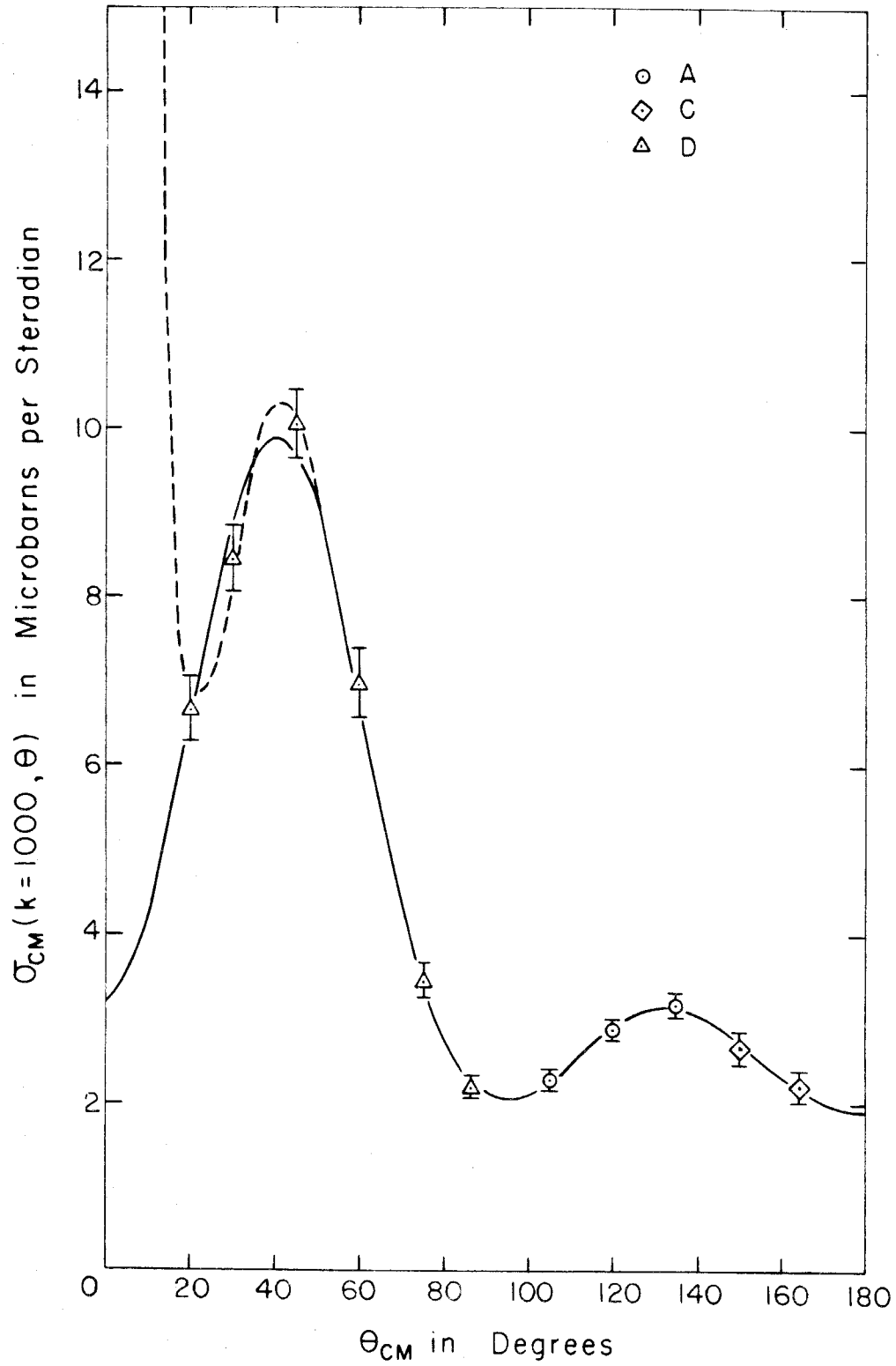
A
C
D
14
12
10
8
6
4
2
0
20
40
60
80
100
120
140
160
180
$\sigma_{CM}(k=1000,\theta)$ in Microbarns per Steradian
θ_{CM} in Degrees

Figure 12

Although the data are fitted well by a polynomial in Cos θ, it has been emphasized by Moravcsik (23) that this type of fit is not theoretically acceptable for charged meson photoproduction. This is due to the term arising from the interaction of the photon with the meson current of the form:

$$\frac{\vec{\varepsilon} \cdot \vec{q}\, \vec{\sigma} \cdot (\vec{k} - \vec{q})}{q_o k - \vec{q} \cdot \vec{k}} \tag{18}$$

where $\vec{k}$ and $\vec{\varepsilon}$ are the photon momentum and polarization, respectively, and $\vec{q}$ and q_o are the momentum and energy, respectively, of the meson. $\vec{\sigma}$ is the nucleon spin. The result of this term is the inclusion of all angular momentum states in the matrix element, which may be expressed in the form

$$M = b \frac{\vec{\sigma} \cdot (\vec{k} - \vec{q})\ \vec{\varepsilon} \cdot \vec{q}}{q_o k(1-\beta \mathrm{Cos}\theta)} + \cdots, \text{ where} \tag{19}$$

$\beta = q/q_o$ is the meson velocity in the c.m. system and θ is the angle between the incoming photon and the outgoing meson. The cross section is proportional to the square of the matrix element and, thus, includes a term with $(1-\beta \mathrm{Cos}\theta)^2$ in the denominator. When expanded in the form

$$(1-\beta \mathrm{Cos}\theta)^{-2} = 1 + 2\beta \mathrm{Cos}\theta + 3\beta^2 \mathrm{Cos}^2\theta + \cdots \tag{20}$$

it is evident that, if β is not small, the cross section will include a high order of dependence on Cosθ. In addition there will be interference with the other terms in the matrix element with a dependence $(1-\beta \mathrm{Cos}\theta)^{-1}$. In order to reduce the complexity Moravcsik suggests an expression for the differential cross section as follows:

$$\frac{d\sigma}{d\Omega} = (1-\beta\mathrm{Cos}\theta)^{-2} \sum_{n=0}^{n=N} B_n \mathrm{Cos}^n\theta \quad . \tag{21}$$

The necessity for fitting charged photoproduction data with expressions of the Moravcsik type has been confirmed by recent experiments at Illinois (24), Berkeley (25), and Stanford (26). These measurements included detection of pions at forward angles where the dependence on $(1-\beta\mathrm{Cos}\theta)$ is most evident, but the theory of Chew and Low used to analyse the data also required inclusion of the so-called "retardation" term described above, in order to obtain a reasonable agreement with the wide angle data in the region of the first resonance.

The least squares fits to the data of this experiment are given by the dashed lines in figures 8-12. For the 600, 700, and 800 Mev points these fits were made with the requirement that the coefficients give the calculated value of the residue at the pole, $\mathrm{Cos}\theta = 1/\beta$, which is obtained on analytic continuation of the expression for $\sigma(k, \theta)$ into the nonphysical region of the complex plane. The pole has a residue due to the numerator of the "retardation" term and the value is given in microbarns/steradian by

$$\mathrm{Residue}(k) = 146\, f^2 \frac{q(2q_o k - k^2 - q^2)(1-\beta^2)}{k^3(1+q_o/(M^2+q^2)^{1/2})(1+k/(M^2+k^2)^{1/2})} \tag{22}$$

where $f^2 = .081$ is the pion-nucleon coupling constant. The terms in the denominator include the recoil effects in the so-called "phase space factor". The units are those obtained by setting $\hbar = c = m_\pi = 1$, where $\hbar$ is Planck's constant, c is the velocity of light, and m_π is the meson mass. M is the nucleon mass measured in units of m_π,

as are q_o, q, and k. β is the meson velocity and all quantities are in the c.m. system. The fitting curves seemed to behave in a more reasonable manner with the residue requirement and an associated error of 10% in the residue for the three lower energies, but the 900 and 1000 Mev fits were poor in that the fitting expressions gave differential cross sections that went to negative values between 20° and 0° when the residue requirement was used, even with an associated error of 100%. The apparent reason for this behavior is found in the loss of significance suffered by the numerical treatment of the sixth order fit of the Moravcsik type given by the Datatron computer. The computer forms the matrix associated with the normal least squares equations. The matrix elements are made up of a sum over all data points of the values $Z/(\text{error})^2(1-\beta\text{Cos}\theta)^4$ for each point with Z ranging from 1 to $\text{Cos}^{12}\theta$ for a N = 6 expansion. The $(1-\beta\text{Cos}\theta)$ term ranges from a value of .03 at 0° to 1.97 at 180° for the 1000 Mev case. Thus, the sums include reciprocal terms from the order 8×10^{-7} to 16. The Datatron keeps only 8 significant figures and the sums are subjected to further addition, subtraction, and mathematical manipulation when the matrix is inverted and the coefficients calculated from the inverse matrix components. The conclusion is that the Datatron is performing a marginal fitting to the Moravcsik expansion of the sixth order when β is close to 1, and the resulting small errors in the $\sum_{n=0}^{n=6} B_n \text{Cos}^n\theta$ are reflected as large errors in $\sigma(k,\theta)$ for the forward angle regions where $(1-\beta\text{Cos}\theta)$ is small. Thus, requirement of the residue fit does not improve the result for the higher order polynomials needed by the 900 and 1000 Mev angular distributions.

The use of the residue to provide a more meaningful physical representation to the data followed a suggestion by M. Gell-Mann. This method to improve the behavior of the fitting curves for the differential cross section in the forward angle region, for which no data were available, appeared successful for the fourth order fits and sixth order fits at the energies where β was not so close to 1 that the computer was forced to operate in a marginal manner. The extrapolation of the curves to forward angle regions where no data are available is not recommended, since the errors reach 20 to 30% of the cross section at 0° and are 10 to 25% at 10° even for the residue limited fits at the lower energies.

The dashed curves indicated in figures 8-12 are all given by $N = 6$ in the Moravcsik expression, since the fits to the data were not as good with $N = 4$, except for $k = 800$ Mev, where the $N = 4$ curve fitted the data as well as the one shown. Since a higher order polynomial was required at lower and higher energies, it seemed appropriate to use the same form at 800 Mev to facilitate comparison of coefficients given in table 7.

The values of the differential cross sections measured at Cornell (8) have been included for comparison. These are not final values, but represent early results obtained at the same time this experiment was in progress. The values shown from Cornell were interpolated from their data which were presented in the form of excitation curves at fixed laboratory angles. Since their measurements were not made at the specific values of k used in this experiment, it was necessary to select the value for k by interpolation. The values obtained in this manner give fair agreement

with the data presented here, although the backward angles seem to give larger values in the Cornell measurements than those obtained in this experiment.

In the early part of this experiment, when the peak near 700 Mev became evident, it was decided to make a measurement of the cross section at 90° in the c.m. system as a function of k. This was done in the range k = 450 Mev to 900 Mev with the standard resolution ($\frac{\Delta p}{p_o} = .0965$) in steps of 50 Mev. The resulting skewed peak was such that a measurement with higher resolution seemed desirable to fix the value of k corresponding to the maximum value, and to check the width of the peak. The results of these measurements are given in figure 13, where the lower energy measurements have been averaged to obtain the values for k less than 450 Mev (9, 10). The classic resonance near 300 Mev in the isotopic spin state I = 3/2 and the angular momentum state J = 3/2 has about the same relative width as the higher energy peak at k = 700 Mev based on this 90° data. The narrow counter measurements do not indicate much change from the poorer resolution data taken with the standard counter, although the values are higher where it would be anticipated that the narrowed range of photon energies might result in a higher average value for σ. This excitation function proved to be a useful indication of the behavior exhibited by the total cross section σ_T, which results from integrating the differential cross section. The data were fitted reasonably well by the pure polynomial expressions with N = 4 for k = 600, 700, and 800 Mev and with N = 6 for k = 900 and 1000 Mev. The expression obtained from integrating over all angles is

Figure 13. 90° Excitation Function.

The spectrometer configurations are indicated by the letters A, B, and C. The interpolated point was obtained from the k = 1000 Mev angular distribution given in figure 12. The Telescope (10) and Magnet (9) data interpolated from earlier low energy experiments are shown without the associated errors of the order 10 to 20%. The solid curve is fitted by eye to the experimental results.

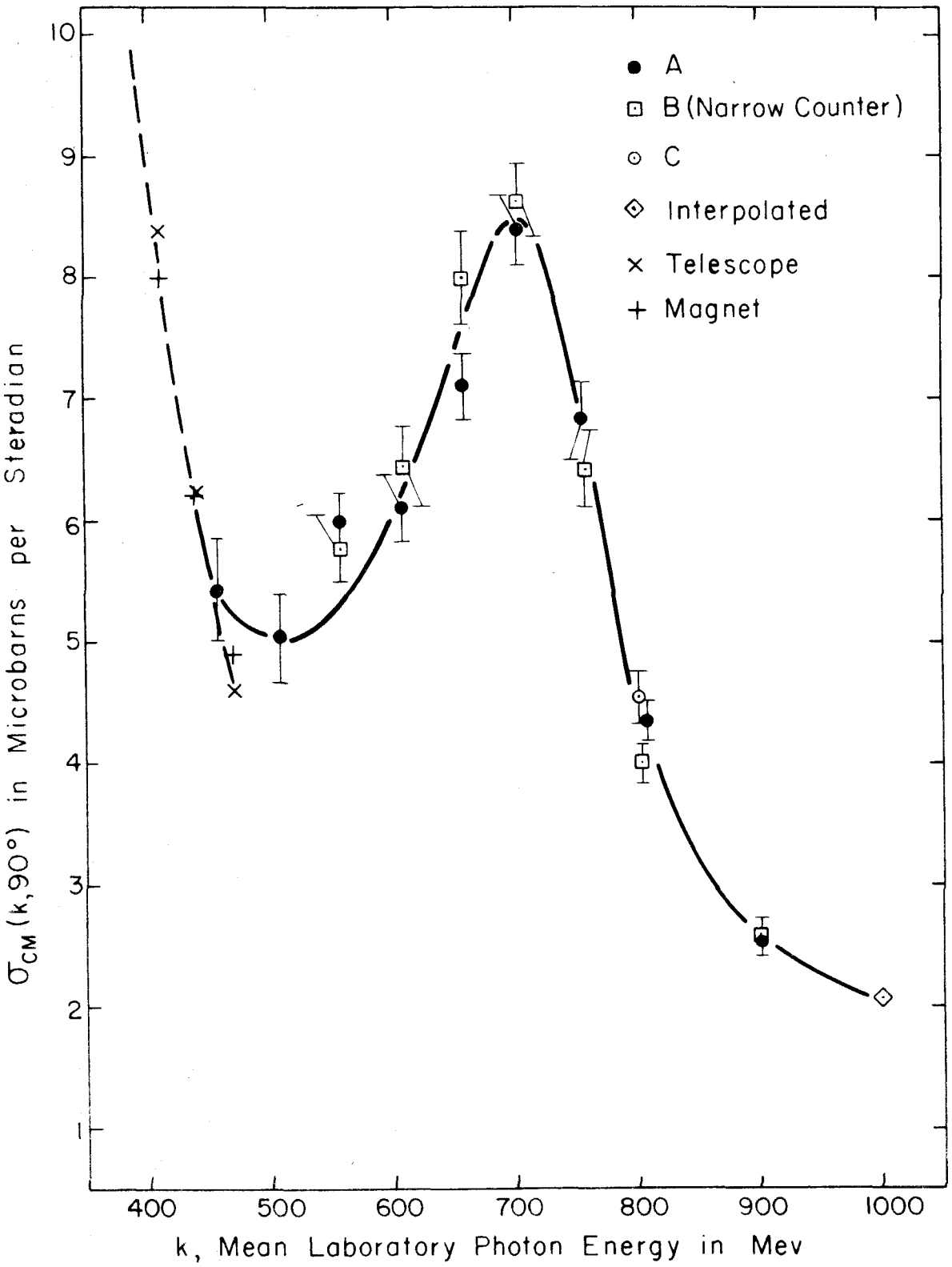
A
B (Narrow Counter)
C
Interpolated
Telescope
Magnet
$\sigma_{CM}(k,90°)$ in Microbarns per Steradian
k, Mean Laboratory Photon Energy in Mev
1
2
3
4
5
6
7
8
9
10
400
500
600
700
800
900
1000

$$\sigma_T = 4\pi(A_0 + A_2/3 + A_4/5 + A_6/7) \qquad (23)$$

for the polynomial up to the 6th power.

The coefficients of the fitted expressions given in equations 17 and 21 are presented in table 7 with the errors associated with the Least Squares Method indicated for each coefficient. The total cross sections are indicated in table 7, and the values of σ_T are plotted in figure 14 with the average values of the earlier measurements below 500 Mev. The early values were raised by a factor of 1.05 in keeping with the convention established by Bernardini (27), who increased these data by 7%, however, to allow for an uncertainty in the beam monitor calibration. The smaller adjustment is believed to be better, based on later calibrations of the ion chamber originally in doubt.

We have joined the earlier data in figure 14 to the results of this measurement by a curve inferred to some extent from the 90° excitation function. This is presumed to follow from the behavior of the angular distributions in the 400 to 800 Mev region where the total cross section behaves very much as the 90° value for the differential cross section as a function of k.

The prominent features of the total cross section as a function of photon energy are the classic resonance in the $I = 3/2$, $J = 3/2$ state at 300 Mev found in the earlier low energy measurements, the peak in the cross section at $k = 700$ Mev with a maximum about half that of the lower energy peak, the minimum which appears about 900 Mev, and the slight rise at $k = 1000$ Mev. A discussion of the angular distributions and variations in the total cross section will be given in the next section.

Table 7

Coefficients for Angular Distributions

A_n : Coefficient given by least squares fit to the experimental data of the form

$$\sigma(k, \theta_{cm}) = \sum_{n=0}^{N} A_n \cos^n \theta_{cm} \text{, where}$$

the A's are in microbarns/steradian.

B_n : Coefficient given by a least squares fit to the experimental data of the Moravcsik type given by

$$\sigma(k, \theta_{cm}) = \frac{1}{(1-\beta \cos\theta_{cm})^2} \sum_{n=0}^{N} B_n \cos^n \theta_{cm}, \text{ where}$$

the B's are in microbarns/steradian.

In both cases N is given by the largest subscript for which a value is shown. The errors are associated with a least squares estimation for the data and errors indicated in Table 6.

σ_T : The total cross section at the indicated photon energy in microbarns ($10^{-30} cm^2$) calculated from the coefficients as follows:

$\sigma_T = 4\pi (A_o + \frac{1}{3} A_2 + \frac{1}{5} A_4 + \frac{1}{7} A_6)$ where terms are included for even coefficients up to N in each case.

Table 7

k (Mev)	A_0	A_1	A_2	A_3	A_4	A_5	A_6	σ_T (10^{-30} cm^2)
600	6.32±.19	7.50±.45	2.83±1.04	-3.44± .68	-2.62±1.19			84.73±1.21
700	8.16±.19	6.54±.34	-2.94±1.04	-2.95± .60	1.77±1.12			94.62±1.19
800	4.54±.10	2.64±.32	.37± .78	.82± .49	.63± .91			60.11± .89
900	2.46±.10	4.71±.53	5.58±1.49	7.94±2.43	.87±4.63	-5.49±2.30	-4.22±3.69	48.88± .92
1000	2.01±.12	1.65±.50	13.87±1.81	13.12±2.21	-7.02±5.27	-14.14±2.10	-6.36±4.00	54.30± .94

k	B_0	B_1	B_2	B_3	B_4	B_5	B_6
600	6.31±.20	-4.08±.78	-5.51±1.45	-3.34±3.13	6.45±3.68	2.93±2.83	-2.61±2.95
700	8.14±.19	-8.39±.65	-8.46±1.02	6.80±2.56	5.30±1.90	-3.01±2.36	- .32±1.69
800	4.52±.10	-5.86±.45	- .45± .69	1.56±1.89	- .28±1.27	.44±1.81	.12±1.25
900	2.40±.09	-4.11±.48	7.30± .86	-4.17±2.00	-8.12±2.39	4.68±1.83	2.10±1.97
1000	2.06±.10	-2.36±.46	10.91± .87	-11.45±2.13	-11.65±2.34	10.27±2.03	2.42±2.03

Figure 14. Total π^+ Cross Section for $\gamma + P \longrightarrow \pi^+ + N$.

The dashed curve is an average of the lower energy experiments (9, 10) increased by a factor 1.05, as explained in the text. The values for this experiment are those quoted in table 7.

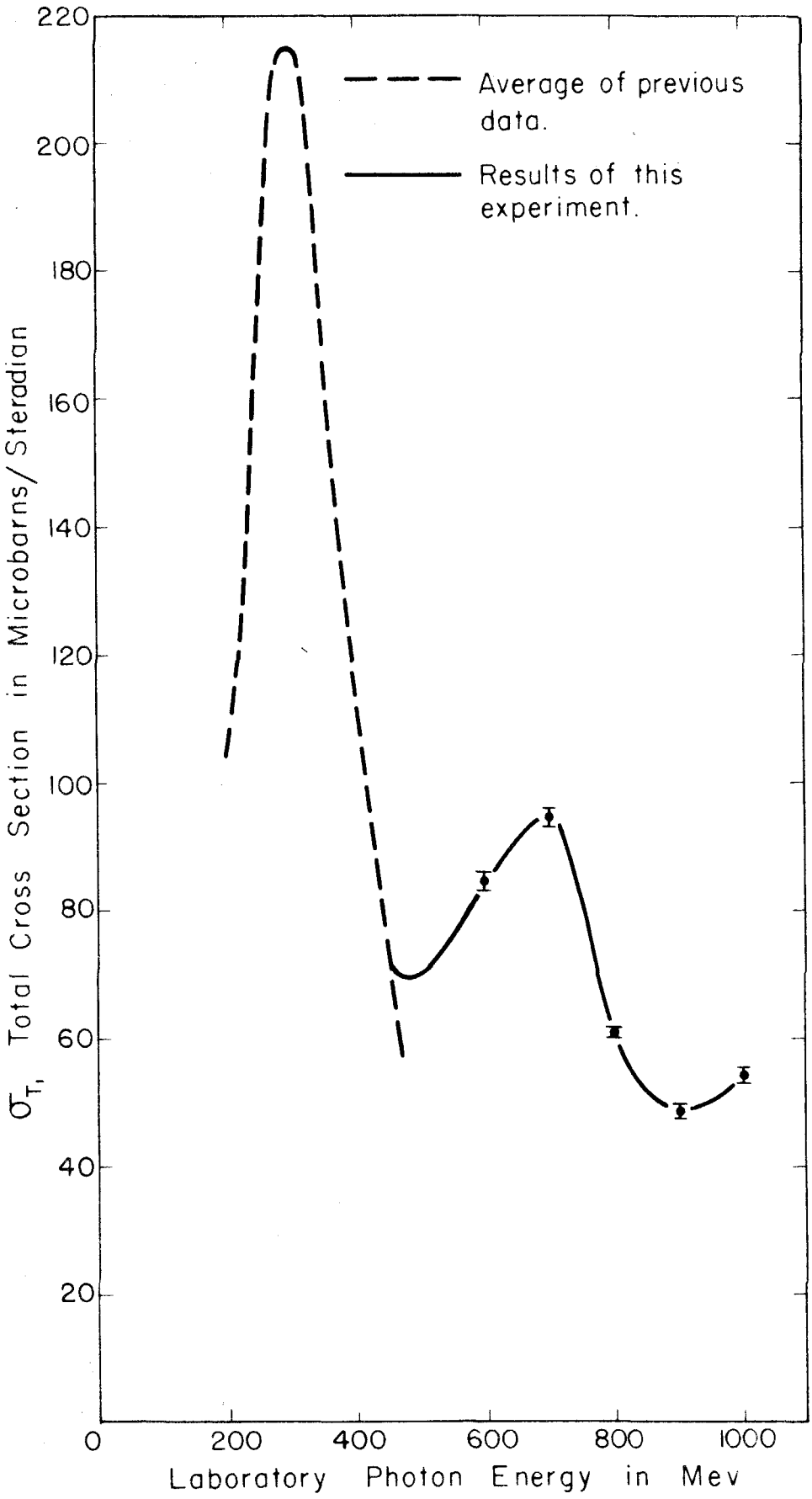
Average of previous data.
Results of this experiment.
σ_T, Total Cross Section in Microbarns/Steradian
220
200
180
160
140
120
100
80
60
40
20
0
200
400
600
800
1000
Laboratory Photon Energy in Mev

VI. INTERPRETATION

In the energy range covered by this experiment the interpretation of the behavior exhibited by the angular distributions and total cross sections is complicated by the number of states which make important contributions. In the lower energy region the important states were the $S_{1/2}$, the $P_{3/2}$, and the meson current contributions for the π^+ photoproduction from hydrogen. The π^o photoproduction showed no appreciable S-state effect and no meson current effect, of course, so the $P_{3/2}$ state represented the only major contribution. When the hypothesis of charge independence is evoked and the isotopic spin formalism applied to the pion-nucleon system, the description of the cross sections in photoproduction achieves some simplification in terms of the total isotopic spin states $I = 3/2$ and $I = 1/2$. Analysis of the photoproduction cross sections leads to the following expressions for π^+ and π^o total cross sections:

$$\sigma(\gamma + P \longrightarrow \pi^+ + N) = \frac{1}{3}\sigma_{3/2} + \frac{2}{3}\sigma_{1/2} + \text{Interference Terms} \tag{24}$$

$$\sigma(\gamma + P \longrightarrow \pi^o + P) = \frac{2}{3}\sigma_{3/2} + \frac{1}{3}\sigma_{1/2} + \text{I.T.},$$

where the subscripts refer to the total isotopic spin. We see that the relative importance of the two isotopic spin states are different for the photoproduction of positive and neutral pions from protons. Similar difference is noted in the scattering cross sections where the relations

$$\sigma(\pi^+, P) = \sigma_{3/2}$$

and

$$\sigma(\pi^-, P) = \frac{1}{3}\sigma_{3/2} + \frac{2}{3}\sigma_{1/2} \quad (25)$$

give the relative importance of the I = 3/2 and 1/2 states.

The π^o and π^+ photoproduction total cross sections are shown in figure 15 and the total (π^+, P) and (π^-, P) cross sections are given in figure 16 for reference. For the first resonance in the I = 3/2, J = 3/2 state with a p-wave meson a comparison of the π^o and π^+ cross sections with $\sigma_{\frac{1}{2}} = 0$, hence $\sigma_{3/2}$ for the $P_{3/2}$ state only, gives the ratio $\pi^o/\pi^+ = 2$ by equation 24. To check this experimentally the $S_{1/2}$ and meson current contributions must be subtracted from the observed π^+ cross section. When this is accomplished, the remainder of the π^+ total cross section at k $\doteq$ 300 Mev is very near half the value of the π^o cross section. This supports the assignment I = 3/2. Further support comes from the scattering experiments, for which the (π^+, P) total cross section is very nearly three times the (π^-, P) total cross section at T = 195 Mev, for T = the laboratory pion kinetic energy. The angular distributions of the scattered pions and the π^o's from photoproduction indicate the resonance to be in a J = 3/2 state, as does the value of the maximum cross section given by

$$\sigma_J = 2\pi \lambda\!\!\!^{-2} (2J+1) \quad (26)$$

with $\lambda\!\!\!^{-}$ the pion wave length over 2π in the c. m. system, and the expression gives the resonance value for an elastically scattered

Figure 15. Photoproduction Total Cross Sections for π^o and π^+ from Hydrogen.

The π^o cross section follows the data of MacDonald (38), Vette (7), and Worlock (33).

The lower energy π^+ curve is an average of the available data below k = 500 Mev and follows the results of this experiment above that energy. These results are indicated by the x's.

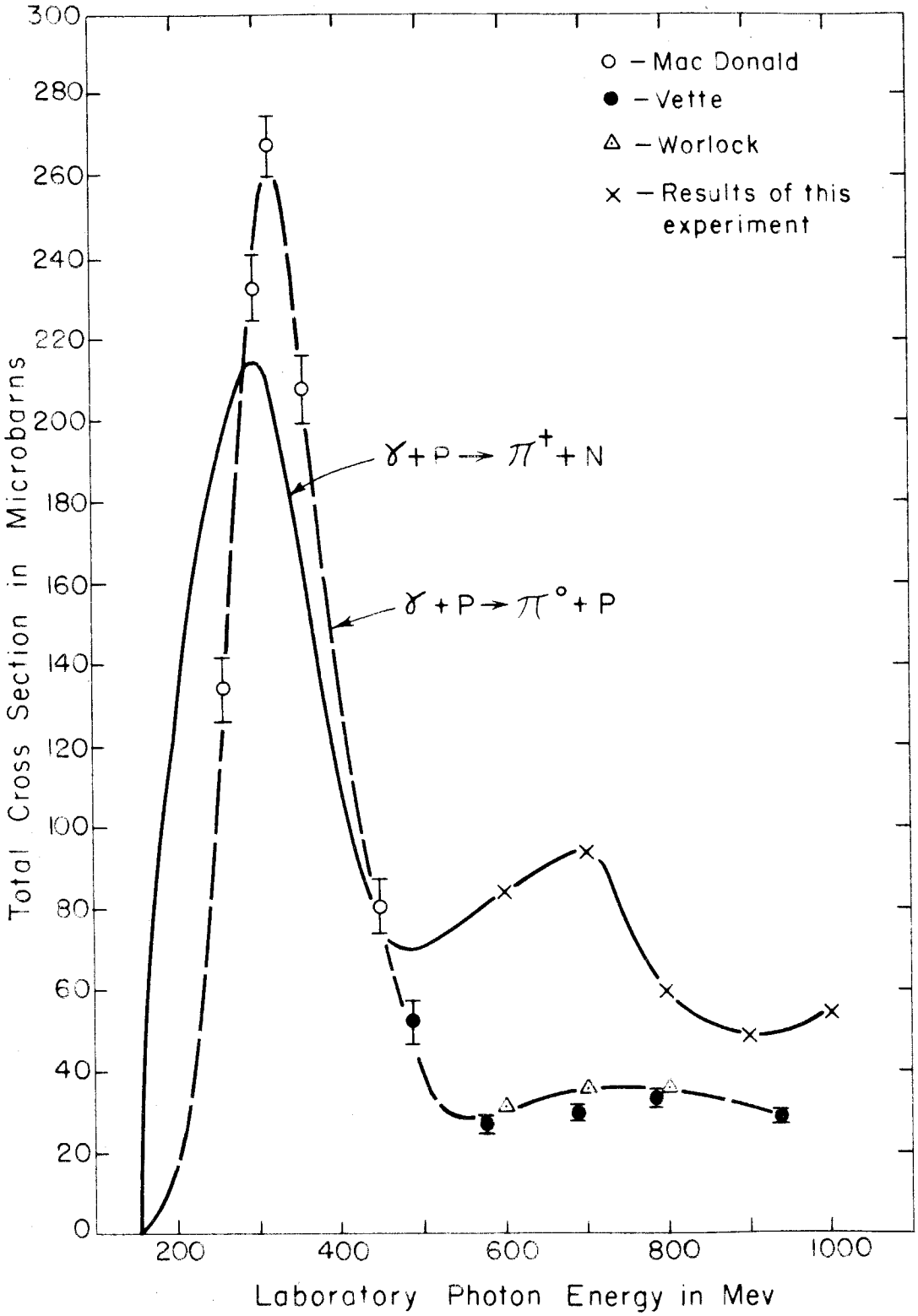
300
280
260
240
220
200
180
160
140
120
100
80
60
40
20
0
200
400
600
800
1000
Total Cross Section in Microbarns
Laboratory Photon Energy in Mev
○ – Mac Donald
● – Vette
△ – Worlock
× – Results of this experiment
γ + P → π⁺ + N
γ + P → π° + P

Figure 16. Total Pion-Proton Cross Sections from π^+ and π^- Scattering Experiments.

The data below 500 Mev are averages of available results and the curves above 500 Mev were taken from the recent results of Burrowes et al (11).

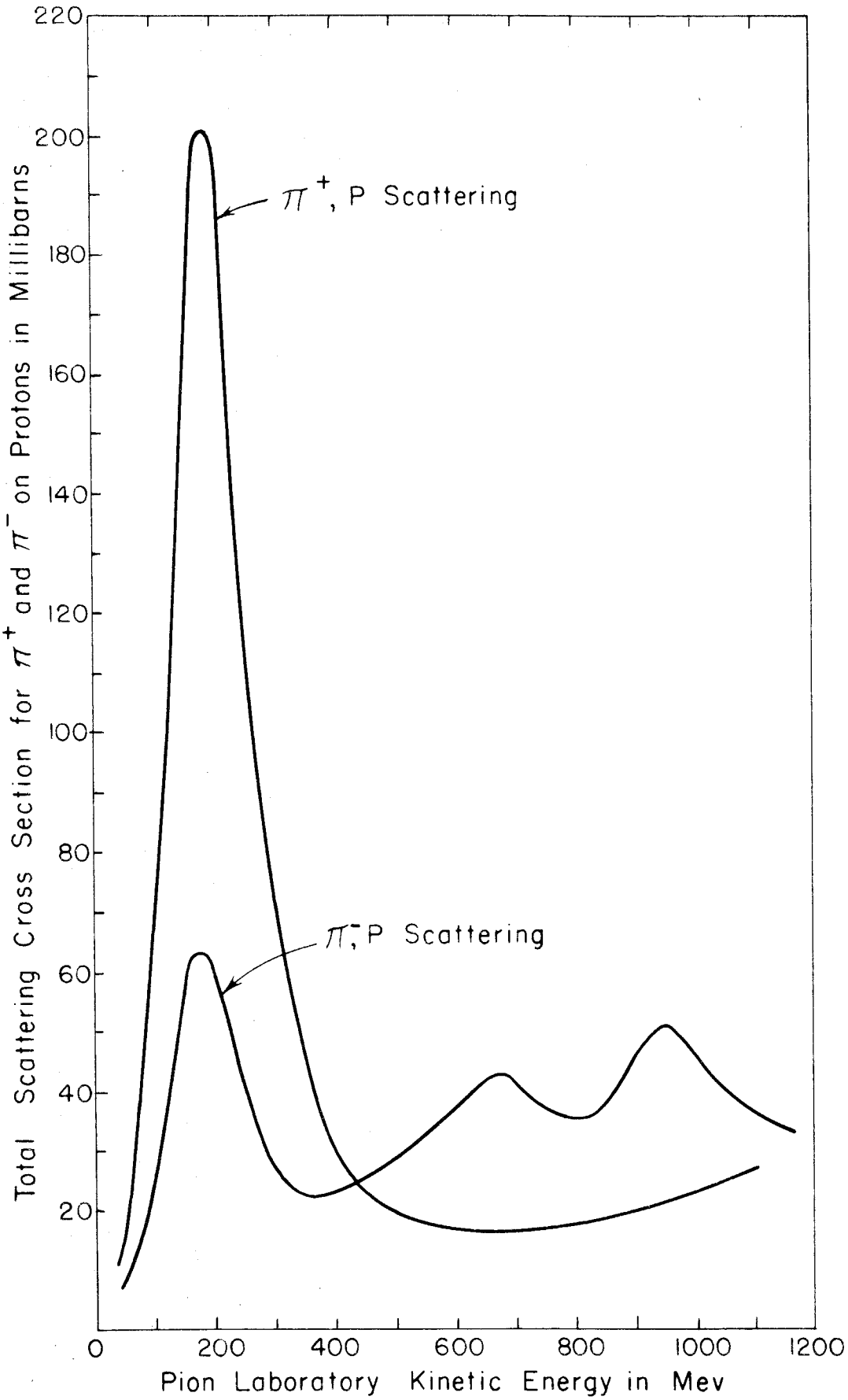
220
200
180
160
140
120
100
80
60
40
20
0
200
400
600
800
1000
1200
Total Scattering Cross Section for π^+ and π^- on Protons in Millibarns
Pion Laboratory Kinetic Energy in Mev
π^+, P Scattering
π^-, P Scattering

particle in an angular momentum state J. The behavior of the related pion-nucleon experimental results in the low energy region is well known and excellent summaries of the data and analysis may be found in the literature (5, 28, 29, 30).

When the early experiments were performed in the low energy region there was no good theory available to explain the results and a phenomenological approach (31) using the scattering phase shifts from experiment and an "enhanced" $I = 3/2$, $J = 3/2$ state was employed by Watson et al with great success. Shortly thereafter, the use of dispersion theory in the hands of Chew, Low, Goldberger, and Nambu (4) gave the best theory to date. The theory of Chew made use of low energy approximations and was not expected to be very successful at energies much above the first resonance. In spite of this the understanding achieved by the application of this theory to various models cannot be overemphasized. In a recent application of this theory to a model of the pion-nucleon system Wetherell (32) has demonstrated the point first noted by Chew that the interference between the retardation term due to the meson current and the $P_{3/2}$ resonant state, as calculated by the Chew effective range formula and dispersion theory amplitudes, was in excellent agreement with the difference between the total π^+ photoproduction cross section minus the contributions of the $S_{1/2}$ term, the retardation term, and their interference and the π^o photoproduction total cross section divided by two. This calculation demonstrated that the apparent difference in the location of the first resonance for π^+ relative to the π^o in photoproduction was due to the terms associated with the meson

current term emphasized by Moravcsik. We see that the effect of the retardation term must be included in a description of the π^+ photoproduction phenomena and the pure polynomial fit, which has been used for most of the low energy data, is not suitable for the π^+ data even in the first resonance region.

The high energy region includes photoproduction with k above 500 Mev and scattering with pion kinetic energy, T, above 400 Mev. The first experimental data in the high energy region came from Brookhaven, where the total cross sections for π^+ and π^- on protons (6) indicated a broad hump in the (π^-, P) total cross section about 600 Mev wide at a mean value near T = 900 Mev. Since this feature was absent in the (π^+, P) results, it was evident that the effect came from the I = 1/2 state (see equation 25). The first data from photoproduction in the energy region above 500 Mev came from the π^o experiments (7, 33, 40). The data of Vette and Worlock are indicated on the total π^o cross section curve of figure 14. From the π^o data we see a broad hump, whose center is not well defined, but taken to be k = 750 Mev, with little suggestion of a resonance. Comparison with the π^+ from this experiment, which is also shown in figure 14, discloses a different shape for the π^+ peak and a lower mean energy. The π^+ peak is skewed toward the low energy side, falling off rapidly on the high energy side of k = 700 Mev. The relative importance of the enhancement effect, being of the order of twice as big in the π^+ case as it is in the π^o case, indicates that the I = 1/2 state is responsible for this second resonance in the photoproduction

from hydrogen. In the angular distributions of π^o Vette found that above 600 Mev photon energy a second order polynomial in Cosθ no longer gave a good fit to the π^o data implying the presence of higher angular momenta. Since there is no meson current interaction of the photon with the meson charge, which is zero for the π^o of course, the confusion in the angular distribution arising from the retardation term and its interference with all the angular momentum states is not present and a correlation between the order of the polynomial fit and the highest meson angular momentum making an important contribution to the pion-nucleon final state is expected to have some significance. From the π^+ angular distribution alone no single J state can be separated as the resonant state at 700 Mev. The simplest picture of the contributing states must include the $S_{1/2}$, $P_{3/2}$, the retardation term and its interference with all other states, and the state responsible for the enhanced cross section. Even with this simple picture it is evident that the angular distribution becomes quite complicated. Also, it is possible that the higher energy, or third resonance state, has some effect even at 700 Mev, where no detectable influence of this higher angular momentum state is seen in the angular distribution itself.

While the isotopic spin assignment for the resonant state at 700 Mev was evident, the angular momentum state has been the subject of much discussion. The first assignment was made by R. R. Wilson (34), who used the $P_{3/2}$ designation and asserted that the broad scattering peak found by Cool (6) in the π^-, Proton

total cross section was really two unresolved peaks, one with J = 3/2 and the higher energy one with J = 5/2, to account for the size of the cross section. This permitted the correlation of the peak in the π^+ photoproduction at 750 Mev according to the Cornell data (8) with the scattering data then available. The second resonance then corresponded to the first of the two peaks predicted by Wilson. This prediction led to further measurements of the scattering of π^+ and π^- mesons from hydrogen at Berkeley (11). This group found two peaks at laboratory pion kinetic energies of 669$\pm$40 Mev and 945$\pm$ 40 Mev. The total cross sections for charged mesons on hydrogen are given in figure 15, where the curves are given by the new data of Burrowes et al from 500 Mev on.

In making a comparison of pion scattering and photoproduction it is necessary to add 150.1 Mev to the pion laboratory kinetic energy incident on a proton to obtain the photon energy incident on a proton, which gives the same kinetic energy in the center-of-momentum system. This means that a photon energy of 700 Mev is to be compared to a pion kinetic energy of 550 Mev when it is desired to correlate photoproduction with scattering experiments. It should be remembered that the photoproduction gives single pions in the reactions studied, but the pion total cross section may have more than the single incident pion present in the final state and a perfect correlation is not possible due to the inelastic processes, which become important above 400 Mev. (Although the threshold for meson production in a pion-nucleon interaction is 170 Mev laboratory pion kinetic energy.) Burrowes et al find

that the peak at 669 is consistent with a resonance in a J = 3/2 angular momentum state when allowance is made for a nonresonant background and the inelastic processes involved.

Shortly after Wilson used the $P_{3/2}$ state assignment, Peierls (35) indicated that a $D_{3/2}$ state would be in better agreement with the angular distributions, which failed to indicate a reversal of the asymmetry on passing through the resonance region. His arguments supported a state with odd parity and J = 3/2, or a $D_{3/2}$ state, as opposed to the $P_{3/2}$ assignment of Wilson, which had an even parity. In an effort to provide a means of deciding which of these assignments might be correct Sakurai (36) showed that Peierls' predicted behavior would result in a high degree of polarization of the recoil proton in π^o production. Observation of large polarization in direction $\vec{q} \times \vec{k}$ would tend to confirm the $D_{3/2}$ assignment. An experiment was undertaken by Stein (37) at Cornell using a Carbon scatterer for the recoil protons, and a high degree of polarization of the proton relative to the $(\vec{q} \times \vec{k})$ plane was observed. The polarization at 675 Mev photon energy for the recoil proton in π^o photoproduction was 60% at 90° in the c.m. system according to Stein. No model other than the one proposed by Peierls would be expected to give a large positive polarization, so the conclusion would be that the $D_{3/2}$ angular momentum state of the pion in the I = 1/2 isotopic spin state is supported by Stein's measurements.

Using the $D_{3/2}$ assignment for the second resonance Wetherell (32) has extended his calculation to higher energies. The calculation used the resonance observed by Burrowes et al (11) at

T = 669 ± 40 Mev to fix the location and included the meson current term, the $P_{3/2}$ contribution from the first resonance, the $S_{1/2}$ contribution to π^+, and the assumed resonant behavior of the $D_{3/2}$ phase shift to show that the differences in the π^+ photoproduction compared to the (π^-, P) scattering and the π^o photoproduction are a natural consequence of the interference effects of the retardation term and the states assumed. Wetherell concludes that a $D_{3/2}$ resonant state, which he assumed for his calculation, is consistent with the observed experimental data. The peculiar shape of the π^+ peak at k = 700 Mev, the differences in the location of the peaks for the π^+ photoproduction and the π^o, and the correlation with the scattering experiment following in a natural way from his calculation.

On the basis of the evidence available thus far, the conclusion that the peak observed in the π^+ photoproduction at 700 Mev is due to a resonance with an assignment of J = 3/2, I = 1/2, and a D-wave meson seems to be well supported. This would occur through an electric dipole transition, which produces a $D_{3/2}$ state.

The existence of a third resonance, inferred from the results of this experiment, is supported by the π^o photoproduction measurements and the (π^-, P) scattering data. The sudden appearance of the unique angular distribution for k = 1000 Mev and its strong resemblance to the J = 5/2 angular distribution resulting from an electric quadrupole or a magnetic quadrupole absorption, respectively leading to a $F_{5/2}$ or $D_{5/2}$ state, is remarkable. The first indication of this behavior occurs in the 900 Mev angular

distribution, where the slight bump near 140^{o} becomes apparent. Then, in the 1000 Mev data the characteristic twin peaked distribution with a minumum near 90^{o} becomes obvious. For comparison the $1+6\cos^{2}\theta-5\cos^{4}\theta$ for a pure $F_{5/2}$ or a pure $D_{5/2}$ state is shown in figure 16 by the solid curve. If we add a term in Cos θ, for example $(3/2)\cos\theta$, the dashed curve results. This gives a front to back asymmetry and the gross features resemble those of the experimental distribution for k = 1000 Mev. Certainly, this does not tell the whole story, but is offered as a demonstration of the importance of this component to the observed data. A complete description will include several states, the $S_{1/2}$, the $P_{3/2}$, the second resonant state taken to be $D_{3/2}$, the meson current term, and the J = 5/2 state could all be important near k = 1000 Mev. It is even possible that other states are important, but these are the obvious choices considering all the evidence.

To support the existence of a third resonance a similar change in the π^{o} angular distributions between k = 785 and k = 940 Mev is shown by Vette (7). His results for these energies are reproduced in figure 18 for reference and they demonstrate the same qualitative behavior as the π^{+} cross sections in the transition from 800 to 1000 Mev. The peak at 90^{o} in the π^{o} differential cross section for k = 785 Mev with the fall off in value on both sides is characteristic of the lower energy angular distributions, also. Then, very suddenly, a minimum appears near 90^{o}, with higher values on both sides. Thus, the k = 940 Mev π^{o} angular distribution also indicates the sudden influence of a higher angular momentum state. Of course, the increase in the total cross section for the

Figure 17. Angular Distribution for $F_{5/2}$ or $D_{5/2}$ State for the Pion initiated by Electric Quadrupole or Magnetic Quadrupole, respectively.

The pure J = 5/2 state from quadrupole absorption by a Proton is represented by the angular distribution $1+6\text{Cos}^2\theta - 5\text{Cos}^4\theta$.

The dashed curve is an illustration of the effect of a $\text{Cos}\theta$ term added to the 5/2 distribution to produce some of the gross features of the k = 1000 Mev angular distribution shown in figure 12.

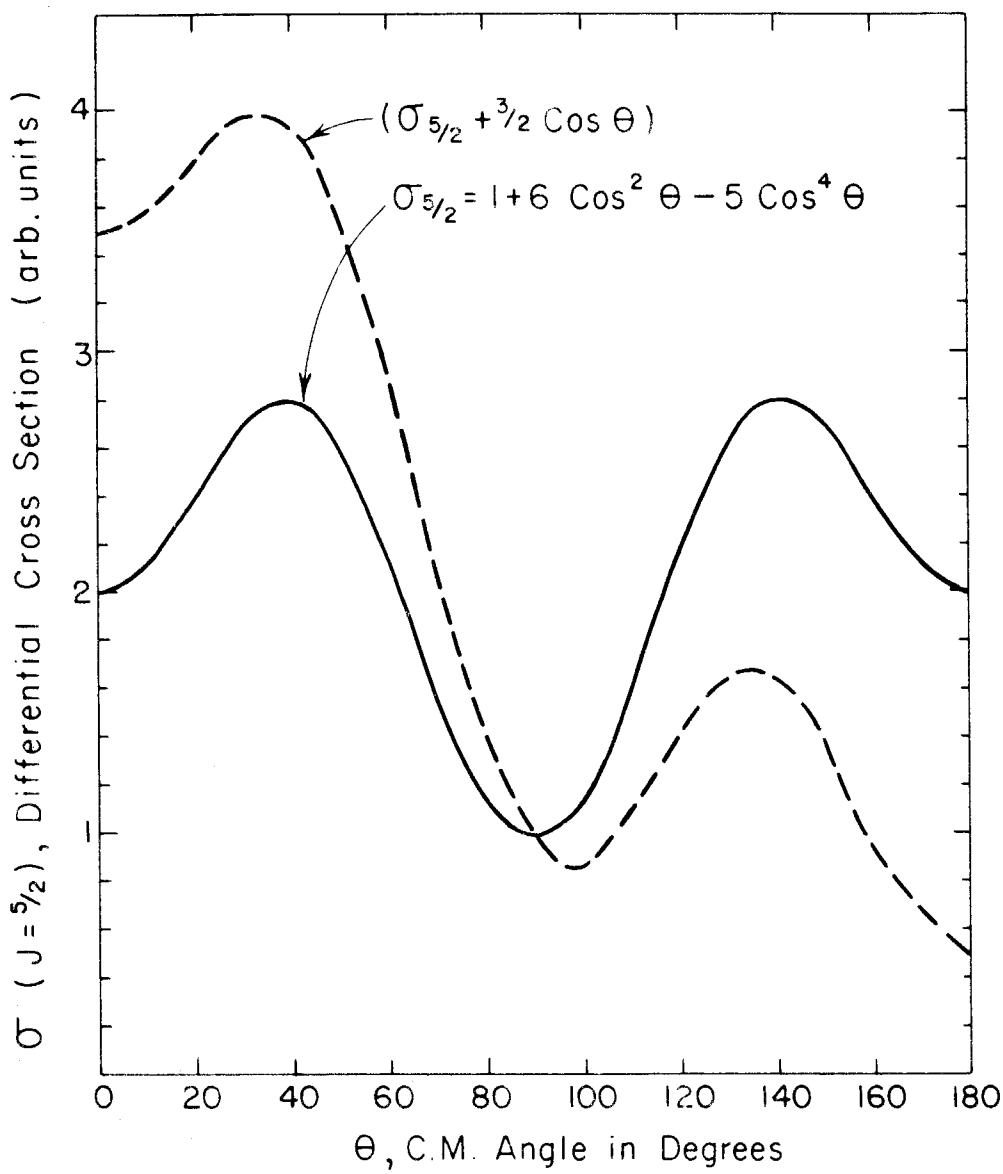
$(\sigma_{5/2} + {}^{3}/_{2} \cos\theta)$
$\sigma_{5/2} = 1 + 6\cos^2\theta - 5\cos^4\theta$
$\sigma\ (J = {}^{5}/_{2})$, Differential Cross Section (arb. units)
4
3
2
1
0
20
40
60
80
100
120
140
160
180
θ, C.M. Angle in Degrees

π^+ photoproduction is not impressive from 900 to 1000 Mev and the conclusions based in part on this effect might not be well founded. Coupled, however, with the π^o photoproduction data, and the higher energy peak observed in the π^-, P scattering experiments the conclusion of a resonance at an energy of 1050 to 1100 Mev seems justified.

Recent measurements of the elastic, inelastic, and charge exchange cross sections for π^- on protons has been reported from Brookhaven by Crittenden, Scandrett, Shephard, Walker, and Ballam (39). They find the peaks near 600 Mev and 950 Mev, in agreement with Burrowes et al, and in addition they find that an enhanced $D_{3/2}$ phase shift is required to give the angular distribution of elastically scattered pions from hydrogen nuclei in a propane bubble chamber at 600 Mev. This is a preliminary attempt by W. D. Walker to fit the data, but offers more support to the second resonance occurring in a $D_{3/2}$ state. Crittenden et al find that f-wave mesons must play a part in the interaction at 950 Mev, since the inelastic cross section is so large that complete absorption of the s, p, and d-wave pions would be required to give the observed effects, if only these states were important. The consistency of an assignment of $J = 5/2$ for the angular momentum state in the higher energy scattering resonance is indicated by the total elastic cross section being less than 35 millibarns in the $I = 1/2$ state. The maximum value of $4\pi(J+1/2)\lambda\!\!\!^{-2}$ would give this value for $J = 5/2$ at an energy of 950 Mev for entirely elastic scattering. The observed elastic cross section in the $I = 1/2$ state is 28 ± 3 millibarns and the inelastic cross section

Figure 18. π^o Angular Distributions for k = 785 and 940 Mev from Vette (7).

The solid curves are least squares fits to a polynomial in Cos θ of the second order and the dashed curves are fourth order fits.

The important feature is the change from the peak at 90^o for k = 785 and lower, to the minimum at 90^o for k = 940 Mev.

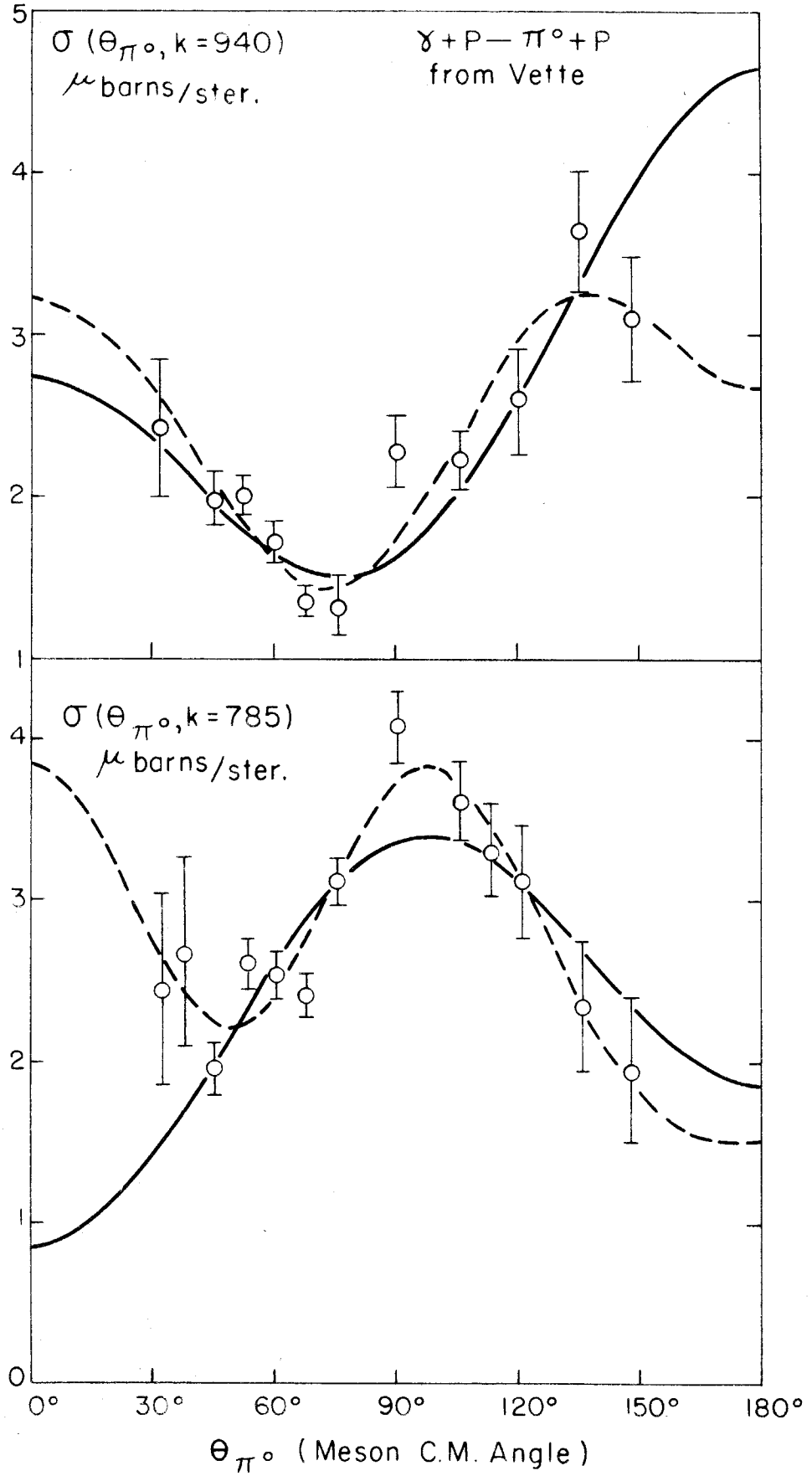
σ (θπ°, k = 940)
μ barns/ster.
γ + P — π° + P
from Vette
σ (θπ°, k = 785)
μ barns/ster.
0°
30°
60°
90°
120°
150°
180°
θπ° (Meson C.M. Angle)

is 37.5 ± 4 mb. It would appear that a nonresonant background plus a resonant $J = 5/2$ state is consistent with these values, providing some of the f-wave mesons are also absorbed.

For the third resonance in π^+ photoproduction we have the sudden appearance of the change in the angular distribution at $k = 1000$ Mev, the increase in the total cross section when the lower energy resonant states are expected to be of less importance, the similar behavior in the π^o data, and the observed third peak in the scattering experiments with a $J = 5/2$ state and f-wave meson consistent with the observed behavior in the $I = 1/2$ elastic, inelastic, and total cross sections.

VII. SUGGESTIONS

The results obtained in this experiment prompt several suggestions for future work, which might aid in understanding the features of high energy photoproduction of pions. The need for further investigation is pointed up by the problems associated with interpreting the high energy behavior of the angular distributions and the total cross sections derived from them.

First, the measurement of π^+ photoproduction cross sections at angles forward of 20° in the c.m. system is essential before a reasonable fit of the Moravcsik type can be made to the data. The importance of this angular range is evident, when the value of β is very near one and $(1-\beta\text{Cos}\theta)$ is near zero. In fitting the data with this expression the significance of the data at angles larger than 90° is such that little confidence is held for extrapolation of the curves into the region where data are not available at forward angles. The need for inclusion of the retardation term is not evident from the measurements that do not include the very forward angles; however, need for this term has been illustrated at lower energies and its influence on the higher energy measurements should be even greater.

The total cross section for 500 Mev photons is needed to complete the π^+ picture, so a measurement of the $k \approx 500$ Mev angular distribution would help to determine the behavior in the region between the data reported here and the lower energy measurements. This information would render the inferences from the 90° differential cross section unnecessary for the determination of the behavior of the total cross section in the 450 to 600

Mev region.

The most interesting question to be answered by future experiment is in the higher energy region not yet attainable. Where is the third resonance located? Plans to increase the peak energy of the Caltech and Cornell synchrotrons have been made, and it should be possible to answer this question in the not too distant future.

To obtain a better understanding of the entire pion-nucleon picture better measurements of the π^o photoproduction cross section in the 800-1100 Mev range would be very helpful. Perhaps the detection of the recoil proton in coincidence with one of the π^o decay gamma rays would be the best way to obtain this information without the large background from pair processes, which detection of the proton alone does not eliminate.

At the end of these measurements it was evident that the electron showering absorber was not essential. Since the absorption correction applied to the half inch of lead was not well determined, elimination of this uncertainty would have made the data better. With the veto counters and the counter in front of the magnet the lead could probably have been eliminated.

VIII. CONCLUSIONS

These measurements of the photoproduction of single positive pions from hydrogen have indicated the presence of two resonances in the 500 to 1100 Mev photon energy region. We may now add to the "classic" $I = 3/2$, $J = 3/2$ resonance at 300 Mev the second resonance, probably in a $J = 3/2$ and $I = 1/2$ state with a D-wave meson, giving a peak in the π^+ total cross section at 700 Mev and the third resonance in an $I = 1/2$ state consistent with a $J = 5/2$ angular momentum assignment, which could come from a D-wave or F-wave meson, giving a peak in the total cross section anticipated to be in the 1050 to 1100 Mev photon energy range.

APPENDIX

Correction for Muon Contamination

The positive pions observed in this experiment were subject to decay by the process $\pi^+ \longrightarrow \mu^+ + \nu$ with a mean lifetime in the pion rest system of $t_o = (2.56 \pm .05) \times 10^{-8}$ second. The muons have a rest energy of $105.70 \pm .06$ Mev and decay with a mean lifetime at rest of $(2.22 \pm .02) \times 10^{-6}$ second. The π^+ has a rest energy of $139.63 \pm .06$ Mev and energetic pions which decay in flight produce muons in an energy range such that signals from a pion or a decay muon in the counter system employed for this experiment have no detectable difference. This means that the counting rate corrected for background is not due to pions alone, but consists of pions and muons from the decay of pions, some of which would have been counted had no decay occurred and some from pions whose momentum or angle of emission fell outside the acceptance window of the spectrometer and would not have been counted. In order to arrive at the number of pions emitted into the solid angle defined by the detection system, the observed counting rate C must be corrected for the pion decay and the muon contamination resulting from this decay. If there were no decay, the "true" counting rate would be

$$C_o = Q(p_o, \theta_o) \left(\frac{\Delta p}{p_o}\right) p_o \, \Delta\Omega A \qquad \text{(A1)}$$

where $Q(p_o, \theta_o)$ is the number of π^+'s emitted at angle θ_o per steradian with a momentum p_o per unit momentum, $\frac{\Delta p}{p_o}$ is the

spectrometer momentum dispersion constant, p_o is the mean momentum of the spectrometer, $\Delta\Omega$ is the solid angle of the spectrometer, and A is the absorption correction given by the number of pions which are not absorbed relative to the number emitted into the spectrometer. In terms of C_o the observed counting rate is

$$C = C_o R = C_o (e^{-S/f} + \frac{C_m}{C_o}) = C_o(R_\pi + R_m) \quad , \tag{A2}$$

in which R is the correction factor for decay effects and is given by the sum of the decay factor, R_π, and the muon correction factor R_m; S is the mean path length travelled by particles from the target to the rear focus of the spectrometer given by the focus-to-focus distance along the mean path through the magnet; and f is the mean decay length for pions in the laboratory system and is related to the mean momentum by the expression $f = 2.157\ p_o$ for p_o in Mev/c and f in inches, indicating that S is also in inches. C_m is the counting rate due to muons. The object of this appendix is to indicate the method used to calculate R_m so that the true pion emission rate C_o may be determined from the observed counting rate C, since R_π is determined by the configuration of the spectrometer and the mean momentum setting. The expression for f given above is obtained from the decay time t in the laboratory, and t_o in the rest system, as follows:

$$f = vt = \frac{pt_o}{m} \tag{A3}$$

for v ≡ velocity, p ≡ momentum, and m ≡ mass in a system of units where c ≡ 1 is the velocity of light. Thus, given p_o the mean value for f follows immediately for a known t_o and m.

Figure A1 shows the coordinate system, which we shall use in our description of the muon correction calculation in front of the magnet. The decay of the muons will be neglected, as their mean life is a factor of 100 longer than that for pions. Since the particles entering the magnet are subject to the discrimination on momentum provided by the magnetic field and counter system, it is convenient to break the calculation down to two parts, which include the contribution to C_m from in front of the magnet and behind the magnet, respectively.

A. In Front of the Magnet

For the muon calculation we have taken the source of pions to be a point source located at the center of the liquid hydrogen target. The contribution to C_m from the region in front of the magnet (up to the middle in the final analysis) is C_{mb} and the contribution from the region after the magnet will be called C_{ma}. Thus, $C_m \equiv C_{mb} + C_{ma}$ will give the total muon contribution. The muon counts before the magnet are

$$C_{mb} \equiv \int \cdots \int Q(p_\pi \theta_\pi) dp_\pi d(\mathrm{Cos}\theta) d\phi \; e^{-r/f} \frac{dr}{f} D(p_\pi, a) \, d\Omega_m, \quad (A4)$$

with $Q(p_\pi, \theta_\pi)\, dp_\pi$ the number of pions per steradian at θ_π with momentum p_π in dp_π, $e^{-r/f} \frac{dr}{f}$ is the fraction of pions which decay in dr at r, $d(\mathrm{Cos}\theta)\, d\phi$ is the pion differential solid angle, $D(p_\pi, a)$ is the probability per steradian of a pion with momentum

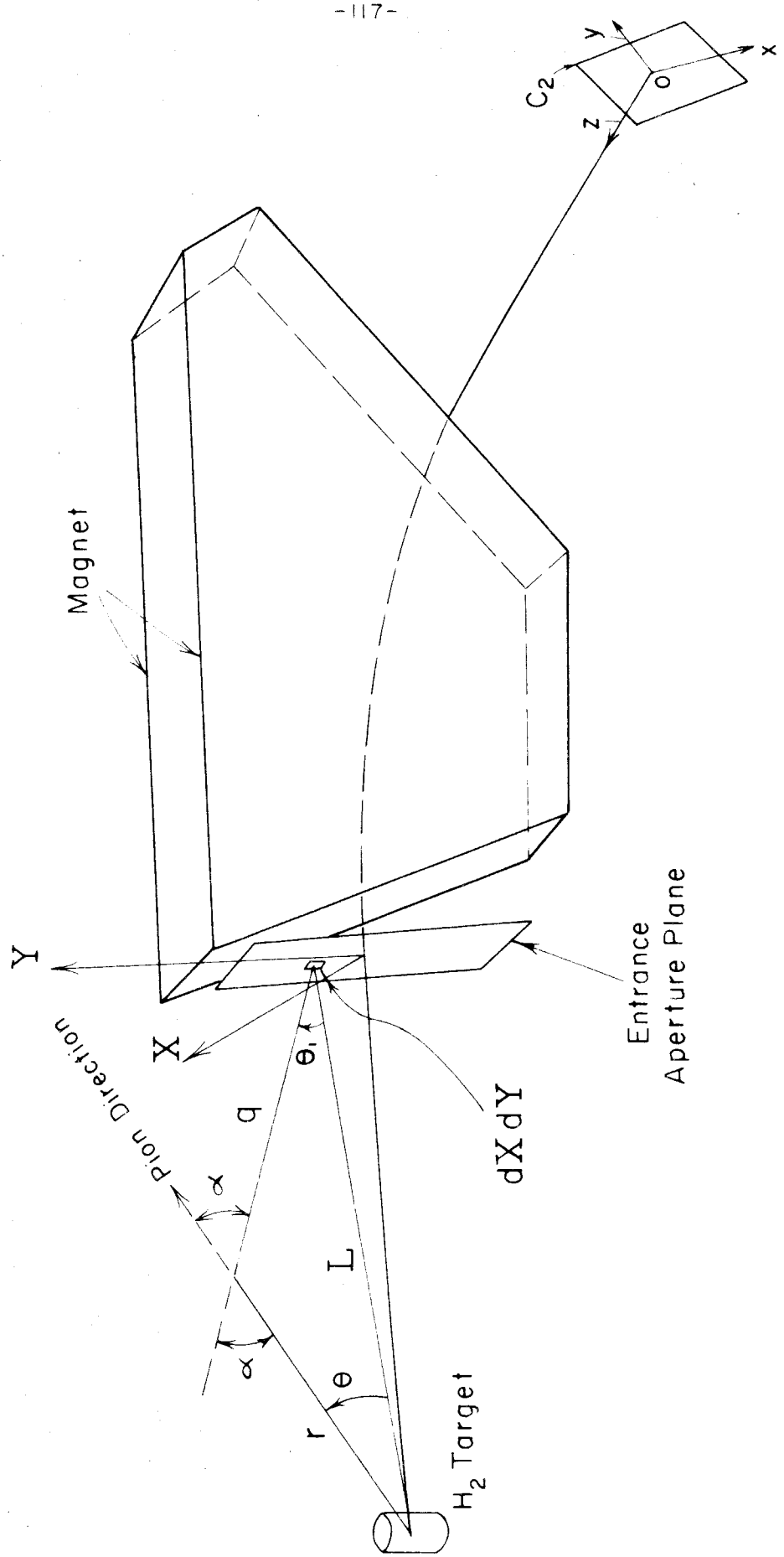

Figure A1. Coordinate System for the Muon Correction

p_π emitting a muon at angle α to the direction of pion motion, and $d\Omega_m$ is the differential muon solid angle. For an elementary area in the aperture dXdY the muon solid angle is $(dXdY/q^2)\text{Cos}\,\theta_1$, which is very nearly $dXdY/q^2$ since θ_1 is small as a result of the very small angles of decay in the energy region under consideration. The maximum value of α is 8° for the lowest pion momentum of this experiment and much smaller in general. The decay probability may be transformed for isotropic decay in the c.m. system (') by

$$\begin{aligned} D(p_\pi, \alpha)d\Omega_m &= D(p_\pi, \alpha')\, d\Omega_m' \\ &= \frac{1}{4\pi}\left(\frac{\partial\Omega'}{\partial\Omega}\right)_{p_\pi} d\Omega_m \\ &\cong \frac{dXdY}{4\pi q^2}\left(\frac{\partial\Omega'}{\partial\Omega}\right)_{p_\pi} . \end{aligned} \tag{A5}$$

Since the decay angles are small we shall neglect the slight dependence on θ and ϕ of $Q(p_\pi, \theta_\pi)$ to arrive at

$$C_{mb} = \int\cdots\int Q\, dp_\pi \frac{e^{-r/f}}{4\pi f}\left(\frac{\partial\Omega'}{\partial\Omega}\right)_{p_\pi} dr\, d(\text{Cos}\theta)d\phi\, \frac{dXdY}{q^2} . \tag{A6}$$

We now change variables from θ to p, the muon momentum by

$$d(\text{Cos}\theta) = \left(\frac{\partial\text{Cos}\theta}{\partial\text{Cos}\alpha}\right)\cdot\left(\frac{\partial\text{Cos}\alpha}{\partial p}\right) dp , \tag{A7}$$

with p_π, r, ϕ, X, and Y held constant. We find from the dynamics of the decay and the geometry that

$$\begin{aligned} \left(\frac{\partial\Omega'}{\partial\Omega}\right)_{p_\pi}\left(\frac{\partial\text{Cos}\theta}{\partial\text{Cos}\alpha}\right)_r\left(\frac{\partial\text{Cos}\alpha}{\partial p}\right)_{p_\pi} &= \frac{\beta M_\pi q^2}{p_\pi p' L^2}\left(\frac{\text{Cos}\alpha}{\text{Cos}\theta - \frac{r}{L}\text{Sin}^2\alpha}\right) \\ &\cong \frac{\beta M_\pi q^2}{p_\pi p' L^2} , \text{ for } \alpha \text{ and } \theta \text{ small,} \end{aligned} \tag{A8}$$

where β is the relative muon velocity, p^* is the c.m. muon momentum = 29.81 Mev/c, M_π = 139.6 Mev/c^2 is the pion mass, and the other quantities were defined earlier. Substitution in our expression for C_{mb} gives

$$C_{mb} \cong \frac{M_\pi}{4\pi p^*} \int \cdots \int Q(p_\pi, \theta_\pi) dp_\pi e^{-r/f} \frac{dr}{f} \int_\phi \beta \frac{p}{p_\pi} \left(\frac{\Delta p}{p}\right) d\phi \frac{dXdY}{L^2} \quad (A9)$$

where we replaced $\int dp$ by Δp the muon acceptance interval and note that $p\left(\frac{\Delta p}{p}\right)$ for the average muon is approximately $p_o\left(\frac{\Delta p}{p_o}\right)$ of the spectrometer. We extract the averages from the ϕ integral to get the relation

$$\int \beta \frac{p}{p_\pi} \left(\frac{\Delta p}{p}\right) d\phi \cong \beta_o \frac{p_o}{p_\pi} \left(\frac{\Delta p}{p}\right)_o \int d\phi \quad , \quad (A10)$$

with β_o the muon velocity/c for momentum p_o. We now replace $\int d\phi$ by the average over X and Y, which is $(\Delta\phi)_{av}$ for $\Delta\phi \equiv \int d\phi$ for a constant p_π, $p = p_o$, and r. This is $\Delta\phi(\theta_1)$, where θ_1 is the angle indicated at the aperture element in figure A1. We also replace $\int dXdY/L^2$ by $\Delta\Omega$, the average solid angle subtended at the target by the spectrometer aperture, to get

$$C_{mb} \cong \frac{M_\pi}{4\pi p^*} \beta_o \left(\frac{\Delta p}{p}\right)_o \Delta\Omega \int\int dp_\pi \frac{dr}{f} e^{-r/f} Q(p_\pi) \frac{p_o}{p_\pi} (\Delta\phi)_{av} . \quad (A11)$$

We wish to obtain R_{mb} the fraction of the "true" pion counting rate, so we divide by C_o to obtain

$$R_{mb} = \frac{C_{mb}}{C_o} \cong \frac{M_\pi}{4\pi p^*} \beta_o \frac{1}{A} \int_{p_{\pi min}}^{p_{\pi max}} \frac{Q(p_\pi)}{Q(p_o)} \left[\int_0^L e^{-r/f} (\Delta\phi)_{av} \frac{dr}{f} \right] \frac{dp_\pi}{p_\pi} \quad , \quad (A12)$$

where $p_{\pi min}$ is the p_π for which p_{max} of muon = p_o and $p_{\pi max}$ is the p_π for which p_{min} of muon = p_o, or the p_π emitted at θ_π from a photon of peak bremsstrahlung energy $k = E_o$, whichever is lower.

From the decay dynamics, for a muon of momentum p_o,

$$p_{\pi max}^{min} = 1/2\ p_o \left[1 + \left(\frac{M_\pi}{M_m}\right)^2\right] \mp 1/2\ E_{mo} \left[\left(\frac{M_\pi}{M_m}\right)^2 - 1\right] \qquad (A13)$$

with $E_{mo} = (p_o^2 + M_m^2)^{1/2}$ the muon energy for momentum p_o.

In this experiment the data were taken with the peak of the bremsstrahlung just above the spectrometer window, or within it in the k = 1000 Mev runs, and $p_{\pi max}$ was fixed by $k = E_o$ for the mean angle of the spectrometer. Within the range of p_π the ratio $Q(p_\pi)/Q(p_o) \simeq 1$ for these measurements, also due to the limitation set by the value of E_o.

In order to evaluate the integrals for R_{mb} we must obtain the average value of $\Delta\phi$. In figure A2 the geometrical limitations to particles in the "horizontal" plane through the central path of the spectrometer are shown. The muon from decay in front of the magnet must pass through the aperture limitation defined by lead slits or the aperture counter depending on the configuration employed and clear the horizontal limitation of the pole face counter or the lead slit on the pole face then pass through the counter system represented by C2. Since the magnet exit aperture is roughly rectangular, we shall take the variation with Y to be negligible for the averaging on $\Delta\phi$ and average in the X direction at the aperture entrance for Y = 0. For a given X, U1 and U2 are the limiting angles for missing the rear aperture limitation and hitting the rear counters. There are three critical values of X, which separate the regions where the limiting angles are set

by the rear counter or the rear aperture, and the regions where U1 is positive or negative. For a given value of X we can evaluate the angle $\Delta\phi$ corresponding to an angle U1 + U2 for which muons can count. The total angular range U1 + U2 is approximately equal to 2U for X less than X1, where U is the angle from the center of the aperture (X = 0) to the limiting ray through the end of the counter. Here U1 $\doteq$ U-X/L and U2 $\doteq$ U + X/L give the spectrometer limits. For X greater than X1, U1 $\doteq$ (a-X)/D - X/L and U2 $\doteq$ U + X/L. For U2 defined to be positive the condition for a count is

$U1 \geq \theta_1 \sin\phi \geq -U2$. This gives the range for $\Delta\phi$

$$\Delta\phi = 2(\text{Arc Sin } U1/\theta_1 + \text{Arc Sin } U2/\theta_1) \ , \tag{A14}$$

where θ_1 is related to the decay angle α of pion with p_π into a muon with p_o at r by the relation $\sin\theta_1 = (r/L)\sin\alpha$. Remembering that our average for $\Delta\phi$ is subject to the fixed values r and p_π with the average muon momentum $p = p_o$, we wish to find $\Delta\phi$ as a function of θ_1. Since the angles are small, $\sin\theta_1 \doteq \theta_1$ and we use the approximation $\theta_1 \doteq r\alpha/L$ for $\sin\alpha \doteq \alpha$. Also, in arriving at R_{mb} we took the solid angle defined by $\int dX dY/L^2$ to be $\Delta\Omega$ of the spectrometer, which is an excellent approximation for an upper limit calculation, which is used to evaluate R_{mb} for each of the 75 points, but we must allow for this change when evaluation of $(\Delta\phi)_{av}$ is required. The substitution of X2 for X3 in the limits of the $\Delta\Omega$ integral gives

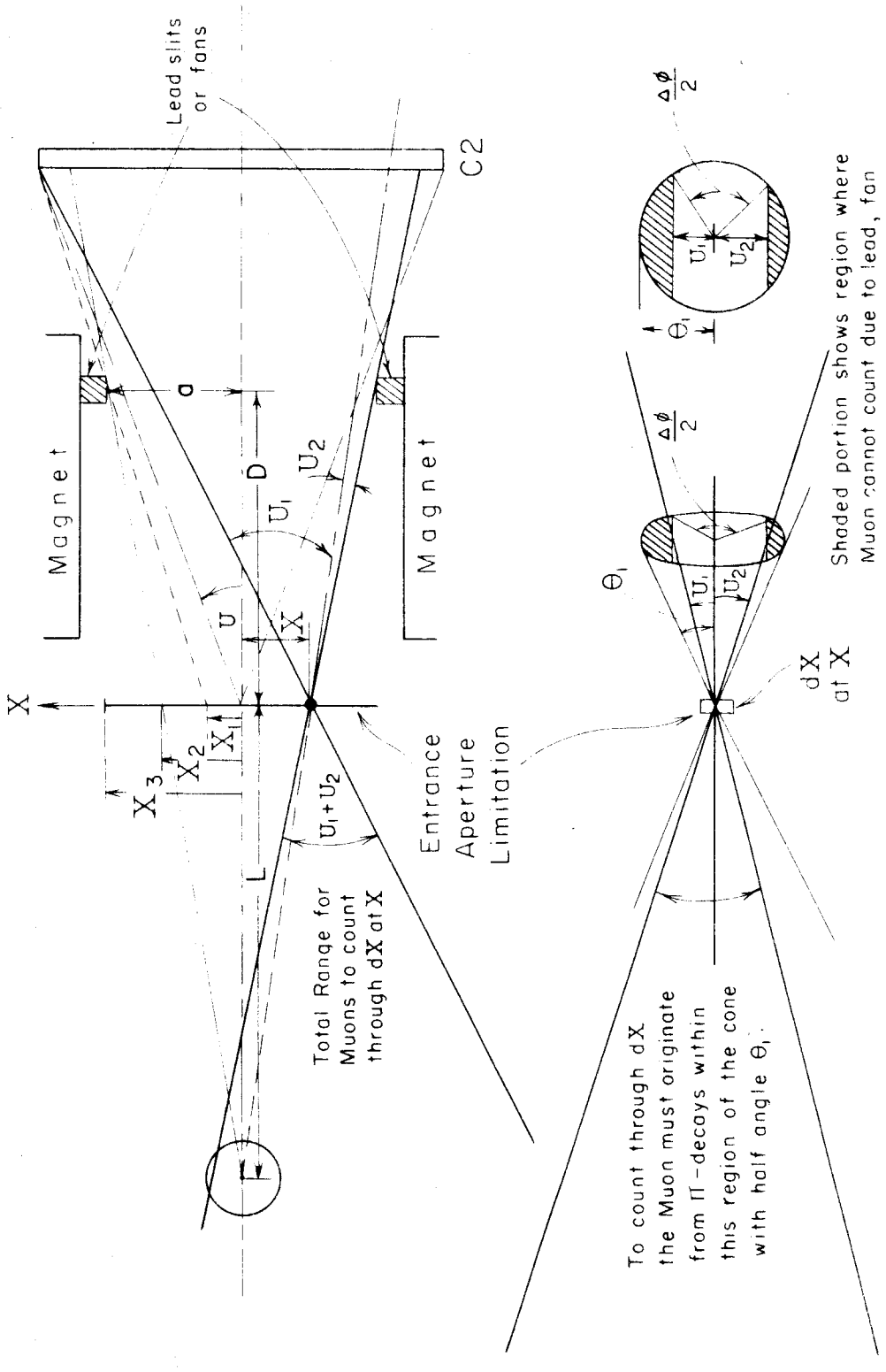

Figure A2. Angular Limitation for Muons from Decays Before the Magnet.

$$\Delta\Omega \cong 2 \int_0^{X2} dX \int_{-Y_a}^{+Y_a} dY/L^2 \cong 4(X2\ Y_a)/L^2 \quad , \tag{A15}$$

where Y_a is the vertical aperture limit on Y. This magnet solid angle is less than the aperture solid angle by the factor X2/X3 and this is adjusted by the following formula in the averaging for $\Delta\phi$ over X:

$$(\Delta\phi)_{av} = \frac{\int_0^{X3} \Delta\phi\, dX}{\int_0^{X3} dX\ X2/X3} = \frac{1}{X2} \int_0^{X3} \Delta\phi\, dX \quad . \tag{A16}$$

Substitution from above for $\Delta\phi$ gives

$$(\Delta\phi)_{av} = \frac{2}{X2} \int_0^{X3} \mathrm{ArcSin}(U1/\theta_1)\, dX + \frac{2}{X2} \int_0^{X3} \mathrm{ArcSin}(U2/\theta_1)\, dX. \tag{A17}$$

From this point on we shall presume that whenever the argument of an inverse Sine equals or exceeds one that the constant value $\pi/2$ will be substituted. Substitution for U1, U2, and θ_1 gives:

$$(\Delta\phi)_{av} \cong \frac{2}{X2} \int_0^{X1} \mathrm{Sin}^{-1}\left(\frac{UL-X}{ra}\right) dX + \frac{2}{X2} \int_{X1}^{X3} \mathrm{Sin}^{-1}(U1/\theta_1)\, dX + \frac{2}{X2} \int_0^{X3} \mathrm{Sin}^{-1}\left(\frac{UL+X}{ra}\right) dX \quad . \tag{A18}$$

We shall use the fact that X1 and X3 are roughly equidistant from X2, where U1 passes through zero as it becomes negative for X larger than X2. We then make the approximation:

$$\int_{X1}^{X3} \mathrm{Sin}^{-1}(U1/\theta_1)dX \cong \mathrm{Sin}^{-1}\left(\frac{UL-X1}{ra}\right)(2X2-X1-X3) \quad , \tag{A19}$$

which we substitute for the second integral in the expression for $(\Delta\phi)_{av}$. We also combine the first and last integrals to get:

$$(\Delta\phi)_{av} \doteq \frac{2}{X2}\int_{-X1}^{X3} \mathrm{Sin}^{-1}\left(\frac{UL+X}{ra}\right)dX + \frac{2}{X2}(2X2-X1-X3)\mathrm{Sin}^{-1}\left(\frac{UL-X1}{ra}\right). \quad (A20)$$

We are now ready to write down the integrated form for $(\Delta\phi)_{av}$ for the three conditions set by the particular value of ra determined by p_π, r and p_o in each case. These regions are I: $0 \leq ra \leq UL-X1$, II: $UL-X1 \leq ra \leq UL+X3$, III: $UL+X3 \leq ra$. Remembering to replace $\mathrm{Sin}^{-1}Z$ by $\pi/2$ when $Z \geq 1$, we obtain for the respective regions the following integrated expressions:

I: $(\Delta\phi)_{av} = 2\pi$

II: $$(\Delta\phi)_{av} \doteq \frac{\pi}{X2}(UL+X3) - \frac{2ra}{X2}\left[\left(\frac{UL-X1}{ra}\right)\mathrm{Sin}^{-1}\left(\frac{UL-X1}{ra}\right) + \sqrt{1-\left(\frac{UL-X1}{ra}\right)^2}\right] + \frac{2}{X2}(2X2-X1-X3)\mathrm{Sin}^{-1}\left(\frac{UL-X1}{ra}\right)$$

III: $$(\Delta\phi)_{av} \doteq \frac{2ra}{X2}\left[\left(\frac{UL+X3}{ra}\right)\mathrm{Sin}^{-1}\left(\frac{UL+X3}{ra}\right) + \sqrt{1-\left(\frac{UL+X3}{ra}\right)^2} - \left(\frac{UL-X1}{ra}\right)\mathrm{Sin}^{-1}\left(\frac{UL-X1}{ra}\right) - \sqrt{1-\left(\frac{UL-X1}{ra}\right)^2}\right] + \frac{2}{X2}(2X2-X1-X3)\,\mathrm{Sin}^{-1}\left(\frac{UL-X1}{ra}\right) . \quad (A21)$$

We now have an expression for $(\Delta\phi)_{av}$, which we can use under the integral sign to evaluate R_{mb}. However, we can replace some of the terms and render the evaluation more straight forward without losing much accuracy. For the ranges of interest the following expressions are useful:

$$1 \leq w \leq 4 : \quad \mathrm{Sin}^{-1}\left(\frac{1}{w}\right) + \sqrt{w^2 - 1} \doteq 0.572 + 0.868w \quad (A22)$$

and

$$\mathrm{Sin}^{-1}\left(\frac{1}{w}\right) \doteq 2.143\, e^{-w/1.5} , \quad (A23)$$

where w is $(\frac{ra}{UL+X_i})$ for $X_i = X3$ or $-X1$. The error is very small for these expressions, the linear approximation is good to a few per cent in general and at worst better than 1 part in 15, this worst value occurring at $w = 1$, where we replace the $\mathrm{Sin}^{-1}(\frac{1}{w})$ by $\pi/2$ for $w \leq 1$. Using these approximate formulae, integration of the variables over r is straightforward. We find for this integral

$$F(a) = \int_0^L e^{-r/f} (\Delta\phi)_{av} \frac{dr}{f} \quad , \tag{A24}$$

the following expressions for our three cases:

I: $a \leq U-X1/L$, $F(a) = 2\pi (1-e^{-L/f})$

II: $U-X1/L \leq a \leq U+X3/L$,

$$F(a) \cong 2\pi(1-e^{-(\frac{UL-X1}{af})}) + \frac{\pi}{X2}(UL+X3)\,(e^{-\frac{UL-X1}{af}} - e^{-\frac{L}{f}})$$

$$+ \frac{2}{X2}\,0.868a\left[(f+L)e^{-\frac{L}{f}} - (f+\frac{UL-X1}{a})e^{-\frac{UL-X1}{af}}\right] \tag{A25}$$

$$+ \frac{1.144}{X2}(UL-X1)\left[e^{-\frac{L}{f}} - e^{-\frac{UL-X1}{af}}\right]$$

$$+ \frac{6.42(2X2-X1-X3)(UL-X1)}{X2\,[af+1.5\,(UL-X1)]}\left[e^{-\frac{1.5(UL-X1)+af}{1.5(UL-X1)}(\frac{UL-X1}{af})}\right.$$

$$\left. - e^{-\frac{1.5(UL-X1)+af}{1.5(UL-X1)}(\frac{L}{f})}\right]$$

III: $U + X3/L \leq a$,

$$F(a) \cong 2\pi\left(1-e^{-\frac{UL-X1}{af}}\right) + \frac{\pi}{X2}(UL+X3)\left[e^{-\frac{UL-X1}{af}} - e^{-\frac{UL+X3}{af}}\right]$$
$$+ \frac{1.736a}{X2}\left[\left(f+\frac{UL+X3}{a}\right)e^{-\frac{UL+X3}{af}} - \left(f+\frac{UL-X1}{a}\right)e^{-\frac{UL-X1}{af}}\right]$$
$$+ \frac{1.144}{X2}(UL+X3)\left(e^{-\frac{UL+X3}{af}} - e^{-\frac{L}{f}}\right) \qquad \text{(A25 Cont'd)}$$
$$- \frac{1.144}{X2}(UL-X1)\left(e^{-\frac{UL-X1}{af}} - e^{-\frac{L}{f}}\right)$$
$$+ \frac{6.42}{X2}\left(\frac{(2X2-X1-X3)(UL-X1)}{af+1.5(UL-X1)}\right)\left[e^{-\frac{1.5(UL-X1)+af}{1.5(UL-X1)}\left(\frac{UL-X1}{af}\right)}\right.$$
$$\left. - e^{-\frac{1.5(UL-X1)+af}{1.5(UL-X1)}\left(\frac{L}{f}\right)}\right] .$$

We are now ready to perform a numerical integration of the expression for R_{mb} given approximately by

$$R_{mb} \cong \frac{M_\pi}{4\pi p'} \beta_o \frac{1}{A} \int_{p_{\pi min}}^{p_{\pi max}} F(a) \frac{dp_\pi}{p_\pi} \qquad \text{(A26)}$$

with the quantities as previously defined. The method involves the following steps:

1. Obtain p_o from the spectrometer setting.
2. Find $p_{\pi min}$ and $p_{\pi max}$.
3. Pick number of points desired for p_π and form the successive values, $p_{\pi n} = p_{\pi min} + (n+1/2)\Delta p_\pi$, with $\Delta p_\pi = (p_{\pi max} - p_{\pi min})/N$ and n = 0 to N.
4. For each $p_{\pi n}$ calculate a_n from the decay dynamics by

$$a_n = \text{Arc Cos}\left(\frac{2E_{mo}E_{\pi n} - (M_\pi^2 + M_m^2)}{2p_o p_{\pi n}}\right) . \qquad \text{(A27)}$$

5. Evaluate $F(\alpha_n)$.

6. Use Simpson's Rule, or a simple sum if N is large enough to provide a good estimate, and evaluate the integral over p_π.

7. Multiply by the constants in front of the integral to obtain R_{mb}.

Since there were many points for which this correction was needed and it was possible to obtain a reasonable estimate without performing the numerical integration at every point, the correction was obtained by performing an upper limit calculation of R_{mb} (to be explained below) and comparing the variation of the numerical integration R_{mb} with the upper limit calculations for a few selected points in each configuration of the spectrometer. As a function of the spectrometer momentum p_o, the variation of R (integrated)/R (upper limit) was a smooth function and it is felt that the estimate given by multiplying the upper limit values of R_{mb} by this function is within the accuracy of the calculation of the integral with the approximations employed.

The upper limit was obtained by setting $(\Delta\phi)_{av} = 2\pi$ and using the approximation $Q(p_\pi)/Q(p_o) \cong 1$ in equation A12 to give

$$R_{mb} \leq \frac{M_\pi}{2p^2}\,\beta_o\,\frac{1}{A}\,(1-e^{-L/f})\,\mathrm{Log}_e\,\left(\frac{p_{\pi max}}{p_{\pi min}}\right) \quad . \tag{A28}$$

The dependence on E_o is present in $p_{\pi max}$. The contribution to the muon contamination before the magnet aperture was obtained for the various configurations using the properties shown in table AI.

Table A1. Spectrometer Configuration Properties used in the Muon Correction.

The terms given for R_{mb} are:

X1 is the point intercepted by a ray touching the horizontal aperture limitation and the edge of C2.
X2 is the point in the aperture intercepted by a ray from the center of the target and grazing the horizontal aperture limitation.
X3 is the edge of the entrance aperture.
U is half the angle subtended by C2 at the center of the entrance aperture (radians).
L is the distance from the center of the target to the entrance aperture.
D is the distance from the aperture to the horizontal defining limitation at the rear of the magnet.
a is the half width of the horizontal limiting gap.
$L_{1/2}$ is the distance from the center of the target halfway through the magnetic field.

All distances are in inches. Refer to figures A1 and A2 for further information.

The terms given for R_{ma} are:

x_1 is the point from the center of C2 where the pion counting density g(x) starts to decrease from g_o.
x_2 is the point where g(x) would reach zero in the linear decrease from g_o at x_1.
x_ℓ is the value of x where the pions are cut off by the geometry of the target and spectrometer so that $g \equiv 0$ for x greater than x_ℓ.
x_c is given by the edge of the defining counter.
g_o is the pion density in the central region of the rear counter normalized by

$$\int_{-x_1}^{+x_1} g_o dx + 2 \int_{x_1}^{x_\ell} g_o \frac{(x_2-x)}{(x_2-x_1)} dx = 1.$$

S/2 is the distance from the center of C2 to the point halfway from the center of the target to the rear focus along the mean path.

Table A1

Spectrometer Configuration Properties used in the Muon Correction

Before the Magnet, R_{mb}

Conf.	X1	X2	X3	U	L	D	a	$L_{1/2}$
A, B	.432	1.002	2.175	.0401	56.0	35.14	1.675	82.5
C	0	.900	1.617	.0364	61.0	40.00	1.460	82.5
D	.830	.928	1.617	.0171	107.5	36.75	1.460	130.0

After the Magnet, R_{ma}

Conf.	x_1	x_2	x_c	x_ℓ	g_o	S/2
A, B	2.800	5.260	5.50	5.260	.1241	82.5
C	2.515	4.345	5.50	5.310	.1458	82.5
D	3.909	6.309	5.50	5.109	.1040	130.5

The fraction R_{mb} gave the correction for the muons before the magnet, but the ultimate correction to be determined had to include the region in the magnetic field. Since previous calculations had shown that the variation of the relative muon contribution with distance along the central path of the spectrometer was a smooth function at the magnet entrance, the upper limit calculation was extended halfway through the magnetic field by changing L to $L_{\frac{1}{2}}$, half the focus-to-focus distance along the central ray. For the small angles of decay, or high momenta pions, this is a better estimate than the low momenta points, where the maximum angle becomes 8^{o} for $p_{o} = 250$ Mev/c and the estimate is slightly high, since some of the decay muons striking the pole faces and limitations are not made up by pions decaying outside the magnet gap. Also, the use of the approximation of the muon momentum dispersion by the spectrometer dispersion becomes a poor average as the decay point moves nearer the rear counter system and the fraction of the distance through the magnetic field becomes smaller. The pion which decays has been subjected to part of the magnet momentum analysis, and the discrimination provided by this combination of effects is difficult to include in the analysis. The value obtained for the front of the magnet muon correction up to the $L_{\frac{1}{2}}$ distance will be called R_{I} and appears in table A2 for each of the points of this experiment. Also, the fraction of the upper limit calculation represented by the actual numerical integration is given by $R_{mb}/R_{mb}(u.l.)$.

Table A2

Results of the Muon Calculations

Point is the measurement as designated in table 5.

R_I is the calculated muon correction for the region in front of the point half way between the target center and the rear focus of the magnet.

R_{II} is the calculated muon correction for the region from the half way point to the rear defining counter, C2.

$R_{mb}/R_{mb}(u.l.)$ is the fraction of the upper limit calculation for before the magnet represented by the actual numerical integration for R_{mb}.

$R_m = R_I + R_{II}$ is the muon correction and is given in table 6 with the 15% error assigned to R_m indicated as the error in the decay correction, $R = R_\pi + R_m$, under the heading ε_R

p* is the pion momentum at the mean spectrometer angle θ_o produced by a photon with $k = E_o$.

Table A2

Point	$R_{mb}/R_{mb}(u.l.)$	R_I	R_{II}	p*
450-90A	.893	.0440	.0554	367.5
500-90A	.905	.0401	.0513	408.0
550-90A	.915	.0343	.0471	438.0
650-90A	.932	.0248	.0421	497.3
750-90A	.946	.0188	.0370	554.0
550-90B	.915	.0343	.0471	438.0
650-90B	.932	.0248	.0421	497.3
750-90B	.946	.0188	.0370	554.0
600-90B	.924	.0284	.0444	468.0
700-90B	.940	.0227	.0395	526.0
800-90B	.952	.0195	.0357	592.0
900-90B	.960	.0143	.0322	640.0
600-20D	.826	.0408	.0556	671.0
600-30D	.817	.0412	.0566	655.4
600-30A	.956	.0291	.0339	655.4
600-45A	.951	.0286	.0360	620.0
600-60A	.945	.0287	.0381	574.0
600-75A	.936	.0279	.0403	522.5
600-90A	.924	.0284	.0444	468.0
600-105A	.911	.0292	.0485	414.0
600-120A	.898	.0401	.0534	379.0
600-135A	.884	.0424	.0590	333.0
600-150C	.840	.0548	.0543	307.4
600-162C	.835	.0541	.0562	286.5

Table A2

Point	$R_{mb}/R_{mb}(u.l.)$	R_I	R_{II}	p*
700-20D	.889	.0326	.0483	770.0
700-30D	.882	.0323	.0483	750.5
700-45D	.861	.0318	.0498	708.6
700-60D	.836	.0401	.0549	654.5
700-60C	.927	.0266	.0304	654.5
700-60A	.959	.0299	.0329	654.5
700-75C	.919	.0213	.0329	592.0
700-75A	.951	.0213	.0354	592.0
700-90A	.940	.0227	.0395	526.0
700-105A	.926	.0212	.0432	461.0
700-120A	.911	.0305	.0490	415.0
700-135A	.896	.0322	.0548	361.0
700-150C	.850	.0415	.0514	326.5
700-163C	.842	.0434	.0534	303.0
800-20D	.922	.0256	.0427	869.0
800-30D	.919	.0258	.0443	846.0
800-45D	.906	.0255	.0459	796.0
800-60D	.884	.0254	.0496	734.0
800-75D	.848	.0252	.0534	660.5
800-75C	.929	.0167	.0297	660.5
800-75A	.961	.0202	.0320	671.0
800-90C	.920	.0170	.0331	583.0
800-90A	.952	.0195	.0357	592.0
800-105A	.938	.0193	.0395	513.0
800-120A	.922	.0236	.0446	449.0
800-135A	.905	.0248	.0505	385.0
800-150C	.858	.0346	.0502	344.5
800-163C	.849	.0340	.0516	314.0

Table A2

Point	$R_{mb}/R_{mb}(u.l.)$	R_I	R_{II}	p*
900-20D	.937	.0191	.0386	958.0
900-30D	.935	.0189	.0394	931.0
900-45D	.929	.0189	.0414	876.0
900-60D	.916	.0208	.0449	812.0
900-75D	.888	.0211	.0485	729.0
900-90A	.960	.0143	.0322	640.0
900-105A	.948	.0140	.0368	551.6
900-120A	.932	.0141	.0413	470.0
900-135A	.915	.0223	.0471	415.0
900-135C	.881	.0242	.0475	415.0
900-150C	.865	.0267	.0474	358.0
900-164C	.854	.0282	.0498	324.7
1000-20D	.942	.0136	.0350	1045.0
1000-30D	.941	.0138	.0352	1017.0
1000-45D	.940	.0159	.0377	965.0
1000-60D	.932	.0142	.0404	875.0
1000-75D	.916	.0133	.0439	782.0
1000-86D	.891	.0136	.0476	710.0
1000-105A	.956	.0096	.0326	588.0
1000-120A	.941	.0094	.0387	498.0
1000-135A	.922	.0101	.0448	420.3
1000-150C	.873	.0098	.0443	361.4
1000-164C	.861	.0108	.0479	324.7

B. Decays Beyond the Magnet

After passing through the magnet the pions have been subjected to the momentum analysis of the magnetic field and the lower momenta particles have been bent through a larger angle than higher momenta particles, which had the same initial direction at the target. In the focal plane of the spectrometer this selection results in the higher momenta pions striking the momentum defining counter at a point above that for a particle with the mean momentum and the opposite for lower momenta. In our analysis of the correction for muons after the magnet we shall use the coordinate system shown in figure A3 with the origin at the center of the defining counter and the x, y plane in the focal plane of the spectrometer. The z coordinate gives the distance from the focal plane, or counter, toward the exit aperture of the magnet. The counter occupies the area $-x_c \leq x \leq +x_c$ and $-y_c \leq y \leq y_c$ where the subscript c is associated with the limits of the sensitive region. The objective is to determine the fraction of the observed counts due to muons from decays occurring after the pions pass through the magnetic field, so we wish to determine what fraction of pions originally headed for a point in the counter, (x, y) within dxdy, decay after the magnet and provide muon counts, as well as how many counts arise from pions decaying after the magnet, but which would not have given a count otherwise. We then integrate over the counter to obtain the total muon contribution.

A certain degree of simplification is achieved by the assumption that the pions coming from the magnet have a

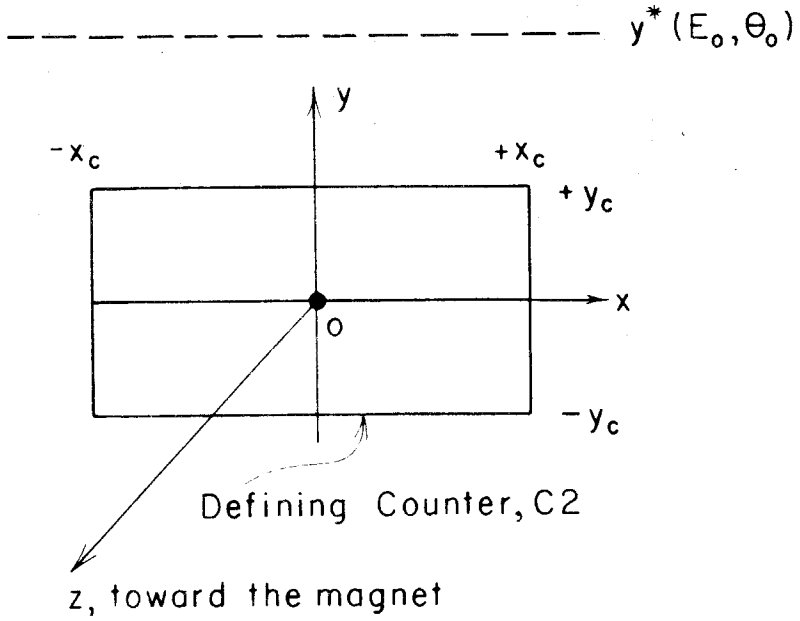

Figure A3. Counter Plane Showing Limits for Muon Effects After the Magnet.

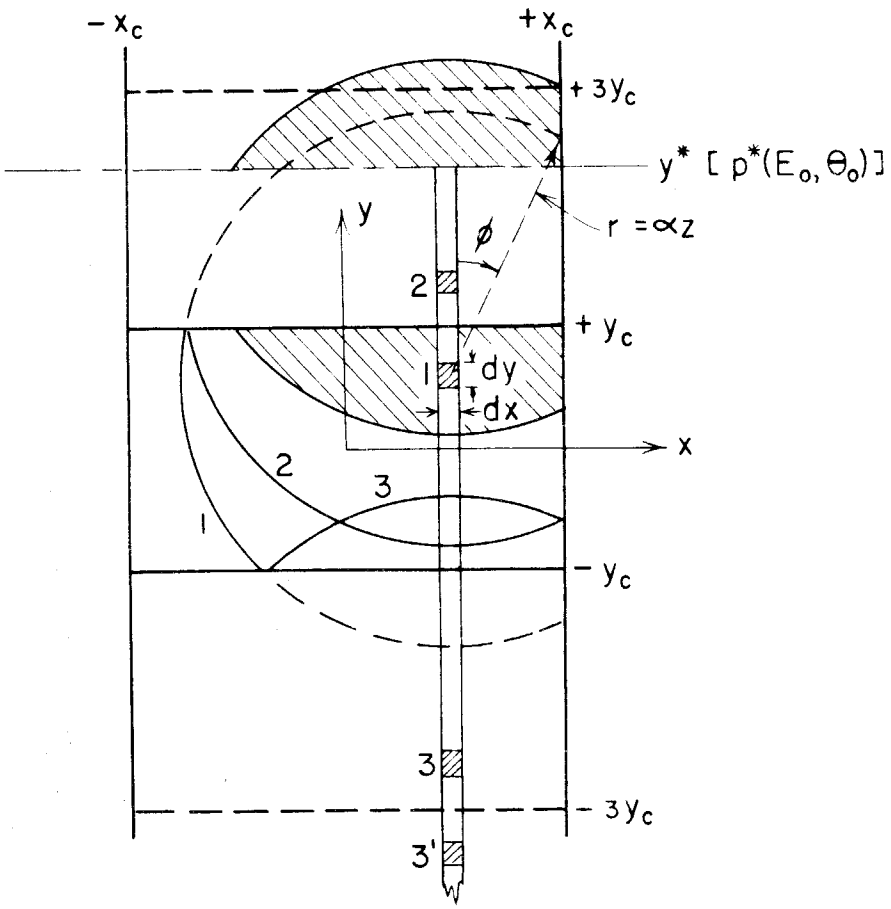

momentum p_o, which is true on the average, and thus, the pions decaying at z have a cone in which the decay muons are distributed with a half angle which is a constant for all pions. This is not true in practice, since some pions having a higher momentum than p_o have a maximum angle which is smaller than that for the mean value, and the lower momenta pions have a larger maximum angle. We shall neglect the small difference, and presume that all pions decaying in a plane at a distance z from the counter within dz have the same half angle cones into which the muons fall.

Taking the element of the counter area, x, y within dxdy, indicated in figure A3, we analyse the contribution in muon counts from pions which would have hit this area of the counter, if there were no decays beyond the magnet. Muons of momentum p from decays in dz at z of pions headed for dxdy fall on a circle of radius r centered at x, y. Some of these particular muons strike the counter on arc 1, while others fall outside the sensitive region on the dashed continuations of arc 1. Within our approximations, neglecting the fact that the pions are not headed directly perpendicular to the plane of the counter, the total arc within the strip between $-x_c$ and $+x_c$ contributes to the muon count if the peak of the bremsstrahlung is sufficiently high so that the strip dx wide is populated with pions far enough from the counter area to make up by the contribution from images of the elementary area reflected in the counter edges the losses due to the dashed arcs. In the case under consideration the muons of momentum p from image 2 give arc 2 and those from image 3 give arc 3. When the peak of the bremsstrahlung is low enough the line indicated by

y^* cuts off the contribution from image elements, since no pions are available to hit the counter plane at y greater than y^*. y^* is given approximately by $\frac{2y_c}{(\Delta p/p_o)} \left(\frac{p^*-p_o}{p^*}\right)$. We see that if allowance is made for the loss over the top represented by y^* that the pions, which would have hit in dxdy, contribute to the muon count in such a way that the counts from pions not destined to strike the counter, but giving decay muons which do so, are included if we accept all the muons falling in the strip from $-x_c$ to x_c.

To obtain R_{ma}, the contribution of muons after the magnet divided by the pion counting rate if there were no decays, we shall find the contribution for each element of the counter and add them up. Let $g(x_\pi, y_\pi)dxdy$ be the number of pions which would hit dxdy if there were no decay. Then the pion counting rate for no decay would be simply

$$C_o = A \int_{-x_c}^{+x_c} \int_{-y_c}^{+y_c} g(x, y)\, dxdy \quad , \tag{A29}$$

where A is the correction for absorption of pions. The number of pions which decay at z within dz and would have hit in dxdy is

$$N(z)dz = g(x, y)dxdy\, e^{-S/f} e^{+z/f}\, dz/f \quad , \tag{A30}$$

where S is the distance from target to defining counter, f is the mean decay length defined earlier, and z is the distance from the counter. The muon counting rate after the magnet becomes

$$C_{ma} = \int\int\int\int g(x, y)dxdy e^{-S/f} e^{+z/f}\, dz/f\, D(p_\pi, a)d\Omega_m \, , \tag{A31}$$

where $D(p_\pi, a)d\Omega_m$ is the probability of a pion of momentum p_π

giving a muon at angle α within the solid angle $d\Omega_m$, and the integrals are performed over the counter area. In terms of the variables p and ϕ for the muon momentum and the azimuthal angle about the pion direction before decay we have from the dynamics:

$$D(p_\pi, \alpha)\, d\Omega_m = \frac{M_\pi \beta_m}{4\pi\, p_\pi p'}\, dp d\phi \quad , \tag{A32}$$

with the symbols defined in our previous analysis. The muon counting rate for decays after the magnet is then

$$C_{ma} = \iiiint g(x, y) dx dy e^{-S/f} e^{+z/f}\, dz/f \frac{M_\pi \beta_m}{4\pi p_\pi p'}\, dp d\phi \quad . \tag{A33}$$

Within our approximation, the density of pions headed for the elemental area dxdy is independent of y and we may find the value of the function g(x) from the geometry of the spectrometer. The value of g(x) is a constant g_o from $x = 0$ to $x = x_1$ and then decreases linearly to $g = 0$ at x_2. Depending on the geometry the value of x_2 may be greater or less than x_c, but the behavior of g(x) is even about $x = 0$ and the integration will make use of this fact. We wish the fraction of muons after the magnet to the "true" pion rate. This fraction is given by

$$R_{ma} \doteq \frac{M_\pi\ e^{-S/f}}{4\pi p' A f} \iint \frac{\beta_m}{p_0}\, e^{+z/f} (\Delta\phi)_{av}\, dz dp \quad , \tag{A34}$$

in which we have replaced the integral over ϕ by the average of $\Delta\phi$ over the counter weighted by the density function g(x). Thus,

$$(\Delta\phi)_{av} = \frac{\int g(x)\ \Delta\phi\ dx}{\int g(x)\ dx} \tag{A35}$$

with

$$\Delta\phi = \int d\phi = 2\left[\mathrm{Sin}^{-1}\left(\frac{x_c - x}{r}\right) + \mathrm{Sin}^{-1}\left(\frac{x_c + x}{r}\right)\right] \qquad \text{(A36)}$$

the total arc length falling within the strip from $-x_c$ to x_c, and where $\mathrm{Sin}^{-1}Z$ is replaced by $\pi/2$ for $Z = 1$ or greater. The value of $r = \alpha z$ is fixed by the muon momentum p for a pion with momentum p_o and the value of z. The integral on z goes from zero to $S/2$ and the integral on p goes from p_{min} for a muon from a pion with p_o to p_{max} given for the same pion momentum. The upper and lower muon momenta are given by

$$p_{\substack{max \\ min}} = \frac{p_o}{2}\left(1 + \frac{M_m^2}{M_\pi^2}\right) \pm \frac{1}{2}\left(p_o^2 + M_\pi^2\right)^{1/2}\left(1 - \frac{M_m^2}{M_\pi^2}\right) \qquad \text{(A37)}$$

$$p_{\substack{max \\ min}} = 0.7865 p_o \pm 0.2185\, E_{\pi o} \qquad \text{(A38)}$$

with $E_{\pi o}$ the mean pion energy accepted by the spectrometer and M_m the muon rest energy.

A numerical integration over the variables was accomplished by a Datatron computer routine, which performed the calculation of $(\Delta\phi)_{av}$ over the counter area with appropriate allowance for the effects associated with the setting of the bremsstrahlung endpoint energy, integrated over p_o and integrated over z to the middle of the magnet. The use of this routine was dictated by the random relation of $k = E_o$ and the associated maximum pion momentum p^* at the mean spectrometer angle θ_o to the mean momentum p_o. Thus, the corrections calculated by the program and given in table A2 under R_{II} will be lacking in a smoothly varying character as

a function of p_o. The muon correction is given by $R_m = R_I + R_{II}$ from this analysis and the error of 15% assigned to this correction represents the estimated standard deviation for the calculated R_m resulting from the various approximations employed.

A monte carlo calculation of this correction using a digital computer should be capable of much greater accuracy than the described method, but the variation in geometry and the dependence on the peak energy of the beam of the various points made the required computer time and the cost prohibitively high. Since the correction is only about ten per cent and the resulting error only 1.5% the correction calculation by this less exact method seems justified.

REFERENCES

1. H. Yukawa, Proc. Phys.-Math. Soc. Japan 17, 48 (1935).
2. Lattes, Occhialini, and Powell, Nature 160, 453 (1947).
3. K. A. Brueckner and K. M. Watson, Phys. Rev. 86, 923 (1952) and Phys. Rev. 90, 699 (1953).
   K. M. Watson, Phys. Rev. 95, 228 (1954).
   Watson, Keck, Tollestrup, and Walker, Phys. Rev. 101, 1159 (1956).
4. Chew, Low, Goldberger, and Nambu, Phys. Rev. 106, 1337, 1345 (1957).
5. H. A. Bethe and F. de Hoffmann, "Mesons and Fields", Vol. II, Row, Peterson and Co., Evanston, Ill. (1955).
6. Cool, Piccioni, and Clark, Phys. Rev. 103, 1082 (1956).
7. J. I. Vette, Phys. Rev. 111, 622 (1958).
8. Heinberg, McClelland, Turkot, Wilson, Woodward, and Zipoy, Phys. Rev. 110, 1209 (1958).
9. Walker, Teasdale, Peterson, and Vette, Phys. Rev. 99, 210 (1955).
10. Tollestrup, Keck, and Worlock, Phys. Rev. 99, 220 (1955).
11. Burrowes, Caldwell, Frisch, Hill, Ritson, Schluter, and Wahlig, Phys. Rev. Lett. 2, 117 (1959).
12. P. L. Donoho, "A Magnetic Spectrometer for Analysis of Particles of Momentum up to 1200 Mev/c", (Nov., 1957), Unpublished.
13. F. P. Dixon, Supplement to reference 12 (1959), Unpublished.
14. R. Gomez, Private Communication.

15. R. R. Wilson, Nuc. Instr. 1, 101 (1957).

16. R. L. Walker, P. L. Donoho, and E. B. Emery, Private Communication.

17. Described on page 16 and shown in figure 4 of reference 33.

18. Woolley, Scott, and Brickwedde, Journal of Research of the National Bureau of Standards 41, 453 (1948).

19. H. M. Brody, Ph. D. Thesis, California Institute of Technology (1959).

20. R. L. Garwin, Rev. Sci. Instr. 24, 618 (1953).

21. W. A. Wenzel, UCRL 8000 (1957).

22. Martin, Anderson, and Yodh, Phys. Rev. 85, 486 (1952).
R. L. Martin, Phys. Rev. 87, 1052 (1952).
Chedester, Isaacs, Sachs, and Steinberger, Phys. Rev. 82, 958 (1951).
Kessler and Lederman, Phys. Rev. 94, 689 (1954).
Abashian, Cool, and Cronin, Phys. Rev. 104, 855 (1956).

23. M. J. Moravcsik, Phys. Rev. 104, 1451 (1956) and Phys. Rev. 107, 600 (1957).

24. Malmberg and Robinson, Phys. Rev. 109, 158 (1958).

25. Uretsky, Kenney, Knapp, and Perez-Mendez, Phys. Rev. Lett. 1, 12 (1958).

26. Lazarus, Panofsky, and Tangherlini, Phys. Rev. 113, 1330 (1959).

27. Beneventano, Bernardini, Carlson-Lee, Stoppini, and Tau, Nuovo Cimento 4, 323 (1956).

28. M. Gell-Mann and K. M. Watson, Ann. Rev. Nuc. Sci. 4, 219 (1954).

29. E. Fermi, Supp. del Nuovo Cimento 2, 17 (1955).

30. G. Bernardini, Supp. del Nuovo Cimento 2, 104 (1955).

31. Watson, Keck, Tollestrup, and Walker, Phys. Rev. 101, 1159 (1956).

32. A Wetherell, "Interference Effects of the Retardation Term in Photopion Production", to be published.

33. R. L. Worlock, Ph.D. Thesis, California Institute of Technology (1958), to be published.

34. R. R. Wilson, Phys. Rev. 110, 1212 (1958).

35. R. F. Peierls, Phys. Rev. Lett. 1, 174 (1958).

36. J. J. Sakurai, Phys. Rev. Lett. 1, 258 (1958).

37. P. C. Stein, Bull. Am. Phys. Soc. Series II, 4, No. 1, 24 (1959).

38. MacDonald, Peterson, and Corson, Phys. Rev. 107, 577 (1957).

39. Crittenden, Scandrett, Shephard, Walker, and Ballam, Phys. Rev. Lett. 2, 121 (1959).

40. Dewire, Jackson, and Littauer, Phys. Rev. 110, 1208 (1958).

P. C. Stein and K. C. Rogers, Phys. Rev. 110, 1209 (1958).